



## MASTER THESIS

# The Study on Metal 3D Printing and Laser Powder Bed Fusion (L-PBF) Additive Manufacturing Process

Mr. Patiparn Ninpetch



A THESIS SUBMITTED IN PARTIAL FULFILLMENT OF THE REQUIREMENTS  
FOR THE DEGREE OF MASTER OF ENGINEERING IN MATERIALS AND PRODUCTION ENGINEERING  
THE SIRINDHORN INTERNATIONAL THAI-GERMAN GRADUATE SCHOOL OF ENGINEERING  
KING MONGKUT'S UNIVERSITY OF TECHNOLOGY NORTH BANGKOK  
ACADEMIC YEAR 2018

COPYRIGHT OF KING MONGKUT'S UNIVERSITY OF TECHNOLOGY NORTH BANGKOK

---

## Author

Name	Mr. Patiparn Ninpetch
Title	The Study on Metal 3D Printing and Laser Powder Bed Fusion (L-PBF) Additive Manufacturing Process
Major Field	Materials and Production Engineering
Advisor	Asst. Prof. Dr.-Ing. Pruet Kowitwarangkul
Co-Advisor	Dr. Sithipong Mahathanabodee
Academic Year	2018

---

## Acknowledgement

Firstly, I would like to thank my thesis advisor and co-advisor Asst. Prof. Dr-Ing Pruet Kowitwarangkul and Dr. Sithipong Mahathanabodee for their guidance, insightful comments and encouragement.

Besides my advisors, I would like to thank Dr. Ruangdaj Tongsri Head of Particulate Materials Processing Technology Research Team at National Metal and Materials Technology Center (MTEC), NSTDA for his kind suggestion and guidance.

I would like to thank the researchers and assistance researcher at ImplanTable Medical Device Technology Research Team lab, Assistive Technology and Medical Devices Research Center, National Science and Technology Development Agency (NSTDA) for facilities support and their guidance.

I would like to thank the support of laser source 50 ns device from “Center Innovation of Design and Engineering for Manufacturing (Col-DEM), KMUTNB, Thailand.

I would like to thank the support of laser source device YLR 300AC from ImplanTable Medical Device Technology Research Team, Assistive Technology and Medical Devices Research Center, National Science and Technology Development Agency (NSTDA)

I would like to thank the fund support from Thailand Graduate Institute of Science and Technology (TGIST), National Science and Technology Development Agency (NSTDA) contract No. SCA-CO-2560-4552-TH, the Thailand Research Fund (TRF) and the Commission on Higher Education (CHE) under the TRF contract No. MRG6180164 and software license support from Flow Science, Inc, Flow Science Japan and Design Through Acceleration Co., Ltd.

Last but not the least, I would like to thank my family, friends and TGGs staff for supporting me throughout writing this thesis.

Patiparn Ninpetch

## Abstract

The aim of this thesis was to study the metal 3D printing technology and the laser powder fusion additive manufacturing process. The work in this thesis was divided into two parts: the numerical study with experimental validation and the experimental study and material characterization. In the first part, the numerical study was applied in order to study the effect of process parameters on physical phenomena in L-PBF process of stainless steels with different grades including AISI 304, AISI 420 and AISI 316L. The results showed that at the lower scanning speed, the temperature field has a region of heat distribution larger than that of the higher one. The results from the simulation are in agreement with the experimental results. In the second part of the thesis, the effect of laser process parameters on single track formation, layer formation, the microstructure and the microhardness of AISI 316L stainless steel fabricated by L-PBF process were investigated by the experimental study. The results indicated that the width of melted track is increased when lower scanning speed are applied. The discontinuous with fragment and instability of melted track occur at the scanning speed of 5 mm/s. When the scanning speed is increased to 10 mm/s, more continuous melted track was formed. The discontinuous melted tracks with balling effect were appeared at H 0.1 mm due to oxidation reaction and the insufficient laser heat energy to fully melt the metal powder. When increasing the hatch spacing to 0.3 mm, the discontinuous melted track with balling effect can be observed with the reduced balling size. Futhermore, the microstructure of AISI 316L stainless steel fabricated by L-PBF process consists of cellular columnar structure and dendrite structure oriented according to temperature gradient direction. The L-PBF process can produce the final parts with higher microhardness than the conventional manufacturer due to rapid cooling rate and small grain size.

Keywords: Additive manufacturing, Metal 3D printing, Laser powder bed fusion (L-PBF) process, Computer simulation, Stainless steels

---

# Table of content

Author .....	i
Acknowledgement .....	ii
Abstract .....	iii
Table of content .....	iv
List of Figure.....	vi
List of Table.....	x
Nomenclature.....	xi
Chapter 1 Introduction .....	1
1.1. Background .....	1
1.2. Objective of the study .....	2
1.3. Scopes of the study .....	2
1.4. Expected Benefits of the study.....	3
Chapter 2 Theory and Literature review .....	4
2.1. Classification of Additive Manufacturing (AM) process .....	4
2.2. Laser Powder Bed Fusion (L-PBF) process.....	5
2.3. Stainless steel types (AISI 304, 316L and 420) .....	16
2.4. Microstructural evolution of AISI 316L stainless steel .....	18
2.5. Laser powder bed fusion of AISI 316L stainless steel.....	21
2.6. Numerical modelling in L-BPF Process .....	24
2.7. Other metal additive manufacturing .....	28
Chapter 3 Methodology .....	31
3.1. The numerical study with experimental validation.....	31
3.1.1 A numerical study on the thermal transient 2D Model with moving laser heat source of AISI 304 stainless steel plate.....	31
3.1.2 Thermal and single track formation simulation in Laser powder bed fusion (L-PBF) process of AISI 420 .....	35

---

3.1.3 Numerical study and experimental validation on single track formation and layer formation of AISI 316L stainless steel fabricated by L-PBF process .....	38
3.2. The experimental study with material characterization .....	43
3.2.1 Materials .....	43
3.2.2 Experimental process.....	43
Chapter 4 Results and Discussion.....	51
4.1. Computer simulation results .....	51
4.1.1 The numerical simulation results of the thermal transient 2D Model with moving laser heat source of AISI 304 stainless steel plate .....	51
4.1.2 The computer simulation results of temperature distribution and single track formation of AISI 420 martensitic stainless steel during Laser powder bed fusion (L-PBF) process .....	53
4.1.3 The results of the numerical study and experimental validation on single track formation and layer formation of AISI 316L stainless steel fabricated by L-PBF process .....	57
4.2. Experimental results.....	62
4.2.1 The effect of scanning speed on melted track width .....	62
4.2.2 Melted pool characteristic with low laser power (Max 50 Watt)....	62
4.2.3 Layer formation with different laser process parameters .....	62
4.2.4 Microstructure of AISI 316L stainless steel fabricated by L-PBF process .....	64
4.2.5 Characterization the microstructure of AISI 316L fabricated by L-PBF process using Scanning electron microscope (SEM) .....	65
4.2.6 The effect of scanning speed and Hatch spacing on cellular structure .....	68
4.2.7 Microhardness of AISI 316L fabricated by L-PBF process .....	69
Chapter 5 Conclusions .....	71
Bibliography .....	73
Biography.....	82
Appendix A.....	84
Appendix B .....	92

---

## List of Figure

Figure 2.1 Types of additive manufacturing process.....	4
Figure 2.2 Schematic of laser powder bed fusion process.....	5
Figure 2.3 An example of laser beam profiles with Gaussian distribution.....	6
Figure 2.4 Relationship of absorption rate of materials and wavelength .....	7
Figure 2.5 Schematic representation of heat transfer in L-PBF process.....	8
Figure 2.6 Types of melt pools shape with difference scanning speed (a) slow, (b) intermediate, (c) fast .....	11
Figure 2.7 Types of Single track formation.....	12
Figure 2.8 Schematic of wetting characteristic (a) wetting system (b) non-wetting system .....	13
Figure 2.9 Schematic of the balling effect mechanism in L-PBF process.....	14
Figure 2.10 The relationship of temperature gradient with growth rate on solidified microstructure .....	14
Figure 2.11 Types of solidification structure in welding process.....	15
Figure 2.12 Heat flow direction in solidification process.....	15
Figure 2.13 Types of microstructure in casting process .....	16
Figure 2.14 The ternary phase diagram of AISI 316L stainless steel.....	19
Figure 2.15 The relationship between the solidification modes with $C_{req}/N_{eq}$ and microstructure .....	20
Figure 2.16 The Shaeffler diagram .....	20
Figure 2.17 The comparison of AISI 316L microstructure at (a) low cooling rate and (b) rapid cooling rate.....	21
Figure 2.18 An example of microstructure with typical defects.....	24
Figure 2.19 An example of temperature distribution during L-PBF process with power 100 W and scanning speed 100 mm/s.....	25
Figure 2.20 The influence of the scan speed (a) and laser power (b) on the width and depth of the molten pool An example of SEM images of surface morphology of L-PBF-processed Ti sample with laser power 150 W and scanning speed 100 mm/s (c).....	25

---

Figure 2.21 The results of molten pool simulation with scanning speed 1.1 m/s, laser power 150 W and packing density 45% .....	26
Figure 2.22 A metal powder melt pool modelling using FLUENT software .....	26
Figure 2.23 Molten fluid flow characteristic of steel powder in SLM process .....	27
Figure 2.24 Comparison of simulation results and experiment results.....	27
Figure 2.25 Schematic of Materials extrusion process .....	29
Figure 2.26 Schematic of binder jetting process.....	29
Figure 2.27 Schematic of Direct energy deposition.....	30
Figure 3.1 Thermal properties of AISI 304; (a) The Thermal conductivity coefficient of AISI 304, (b) The specific heat capacity of AISI 304 .....	32
Figure 3.2 Setup simulation in ANSYS 18.1 program .....	33
Figure 3.3 CAD model (a) The geometry and moving path of laser heat source, (b) mesh elements of the work piece model .....	33
Figure 3.4 The experiment setup (a) Laser source device at Center Innovation of Design and Engineering for Manufacturing (Col-DEM), KMUTNB, (b) Specimen and experimental setup .....	35
Figure 3.5 The simulation setup in the Flow-3D program.....	36
Figure 3.6 The schematic of the powder bed and scanning direction of moving laser beam.....	37
Figure 3.7 Thermal-physical properties of AISI 420 stainless steel including density, thermal conductivity, specific heat .....	37
Figure 3.8 The schematic of simulation domain for single track formation.....	39
Figure 3.9 The schematic of simulation domain for layer formation .....	40
Figure 3.10 Thermal-physical properties of AISI 316L stainless steel including density, thermal conductivity, specific heat .....	41
Figure 3.11 The experimental setup.....	42
Figure 3.12 The experimental process in the second part.....	43
Figure 3.13 The building platform and gas chamber.....	44
Figure 3.14 Creating specimens (a) The laser heat source interacting with metal powder bed in L-PBF process, (b) An example of the specimens.....	45
Figure 3.15 The analysis equipment (a) Stereomicroscope, (b) macro camera.....	45
Figure 3.16 The process of cutting the specimens, (a) cutting machine, (b) The cut specimens.....	46

---

Figure 3.17 The hot mounting process (a) Hot mounting machine, (b) The section of specimens inside hot mount resin .....	46
Figure 3.18 Grinding process.....	47
Figure 3.19 Polishing process .....	47
Figure 3.20 The acids used in etching process .....	48
Figure 3.21 The process of microstructure analysis .....	48
Figure 3.22 Scanning electron microscopy.....	49
Figure 3.23 Testing the hardness properties .....	49
Figure 4.1 Temperature distribution in the numerical specimen model from the scenario 1 at time (a) 30 sec, (b) 70 sec and (c) 101 sec.....	51
Figure 4.2 Temperature History at The Probe Point No.1 of Specimen in (a) Scenario 1 and (b) Scenario 2 .....	52
Figure 4.3 Comparison of Temperature History at The Probe Point No.1 From the 4 Scenarios of Numerical Simulation .....	52
Figure 4.4 The Temperature History Profile at Six Probe Points of (a) Scenario 3 and (b) Scenario 5.....	53
Figure 4.5 The effect of laser power on temperature field during L-PBF process .....	54
Figure 4.6 The effect of scanning speed on temperature field during L-PBF process .....	54
Figure 4.7 The effect of scanning speed on melt pool geometry.....	55
Figure 4.8 Longitudinal section view of molten metal pool and fluid flow in molten metal pool.....	55
Figure 4.9 The effect of laser power on the width of single track formation .....	56
Figure 4.10 The effect of scanning speed on the width of single track formation .....	56
Figure 4.11 The effect of laser power on single track formation depth.....	57
Figure 4.12 The effect of scanning speed on single track formation depth.....	57
Figure 4.13 The simulation results validated with experimental results (a), The effect of process parameter on the width of single track formation.....	57
Figure 4.14 The measurement of width and depth of melted track obtained by computer simulation.....	58
Figure 4.15 An example measurement the melted track obtained by experiment.....	58
Figure 4.16 The melted track width with different scanning speed.....	59
Figure 4.17 The melted track width with different laser power .....	59
Figure 4.18 The melted track depth with different scanning speed.....	60
Figure 4.19 The melted track depth with different laser power.....	60

---

Figure 4.20 Surface morphologies of the first layer formation with two different.....	61
Figure 4.21 the cross section of layer formation with different hatch spacing.....	61
Figure 4.22 The single track formation width with different scanning speed .....	62
Figure 4.23 Melt pool characteristic from (a) experiment, (b) simulation .....	62
Figure 4.24 The layer formation with different hatch spacing, (a) $H = 0.1$ mm, (b) $H = 0.3$ mm, (c) $H = 0.5$ mm .....	63
Figure 4.25 The layer formation with different scanning speed, (a) $v = 5$ mm/s, (b) 10 mm/s and (c) 15 mm/s.....	63
Figure 4.26 AISI 316L Microstructure (a) cross section area of melted powder bed layer formation, (b), (c), (d) Microstructure of AISI 316L fabricated by L-PBF.....	64
Figure 4.27 The cellular and columnar dendrite structure of AISI 316L stainless steel fabricated by L-PBF process with magnificant 5000x .....	65
Figure 4.28 The cellular structure of AISI 316L stainless steel fabricated by L-PBF process with magnificant 10000x .....	65
Figure 4.29 The cellular structure of AISI 316L stainless steel fabricated by L-PBF process with magnificant 20000x .....	66
Figure 4.30 The chemical composition of the cellular structure (full area) obtained by SEM-EDS .....	66
Figure 4.31 The chemical composition of the cellular structure (point) obtained by SEM-EDS .....	67
Figure 4.32 The chemical composition of the cellular structure (Mapping) obtained by SEM-EDS .....	67
Figure 4.33 The chemical composition of the cellular structure (Mapping) obtained by SEM-EDS .....	68
Figure 4.34 The cellular structure with different scanning speed.....	69
Figure 4.35 The cellular structure with different hatch spacing .....	69
Figure 4.36 Microhardness of AISI 316L fabricated by L-PBF process.....	70
Figure 4.37 The microhardness of L-PBF compared with the conventional process..	70

---

## List of Table

Table 2.1 Chemical composition (%wt.) of AISI 304 stainless steel [39].....	17
Table 2.2 Chemical composition (%wt.) of AISI 420 martensitic stainless steel [40] .....	17
Table 2.3 The chemical compositions (%wt.) of AISI 316L stainless steel [41] .....	18
Table 2.4 Mechanical properties of AISI 316L stainless steel [41].....	18
Table 2.5 The comparison of mechanical properties of AISI 316L stainless steel fabricated by L-PBF process and the conventional method [7].....	23
Table 3.1 Process parameters for the numerical simulation of moving laser heat source .....	34
Table 3.2 Five cases of numerical simulations with different parameters of moving laser heat source .....	34
Table 3.3 Materials properties of AISI 420 stainless steel and Process parameters used in this simulation study .....	37
Table 3.4 Case study of the numerical simulation with different process parameters	38
Table 3.5 Materials properties of AISI 316L stainless steel and Process parameters used in this simulation study .....	40
Table 3.6 The case study of numerical simulation with different process parameters	41
Table 3.7 The chemical compositions of stainless steels including AISI 304 and AISI 316L [82] .....	43
Table 3.8 The six cases experiment study of single single track formation with different the scanning speed .....	50

---

# Nomenclature

$A_c$	Absorption coefficient
$C$	Heat capacity [J/K]
$C_p$	Specific heat capacity [J/kg.K]
$d$	Laser spot size [ $\mu\text{m}$ ]
$d_l$	Beam diameter [mm]
$E$	Heat energy [J]
$g$	gravitational acceleration in z direction [ $\text{m/s}^2$ ]
$G$	Temperature gradient [K]
$H$	Hatch spacing [mm]
$I_o$	Power intensity [ $\text{W/mm}^2$ ]
$L_f$	Latent heat of fusion [J/kg]
$L_t$	Layer thickness [ $\mu\text{m}$ ]
$P$	Laser power [W]
$Q$	Internal heat [J]
$R$	Radial distance [mm]
$T$	Temperature [K]
$T_0$	Initial temperature [K]
$T_e$	Environment temperature [K]
$T_m$	melting temperature of material [K]
$T_s$	Solidus temperature [K]
$v$	Scanning speed [mm/s]

# Chapter 1 Introduction

## 1.1. Background

Additive manufacturing (AM) process, also known as 3D printing technology, is becoming the next industrial revolution [1]. It is also a key technology that hold the potential to boost the future growth of the 10 S-curve industries for Thailand 4.0. The 3D printing technology is defined by National Council on Research and Innovation Policy by National Research Council of Thailand (NRCT) and National Science Technology and Innovation Policy Office as one of modern technologies in digital technology in Thailand's 20-year national strategy for revolutionary innovation and improvement in service and production [2]. Recently, the 3D printing technology began to rise a significant in commercial manufacturing technology [3]. It can create products through 3D CAD model without using cutting tools and mold. The process has advantages for producing near net shape parts, complex topology parts, lattice structure parts, manufacturing tool, medical parts, aerospace parts, and automotive parts. [4,5]. Various materials can be used in manufacturing process including metal, polymer, ceramic, composites, food, vax and biomaterials [6].

There are several methods in 3D printing process such as laser powder bed fusion (L-PBF) or selective laser melting (SLM), binder jetting, materials extrusion and direct energy deposition, etc [7]. This current study is primarily concerned with the laser powder bed fusion (L-PBF) process. It is the most widespread AM process which uses laser source scanning as a moving heat source on powder bed to fully melt the metal powder a layer-by- layer fashion. The main laser process parameters are laser power (P), laser spot size (d), scanning speed (v), hatch spacing (H), layer thickness ( $L_t$ ) and working atmosphere [8]. During the process, it involves several complex multiphysics such as the materials absorption, heat transfer, molten fluid dynamic, surface tension, phase transformation, rapid melting, rapid solidification, recoil pressure, evaporation, chemical reaction, distortion, and thermal stress, etc. These physical phenomena have significant influence on the physical properties, mechanical

properties and the microstructure of final parts, e.g. density, dimension, void, porosity, non-fully melted particle, and balling effect phenomena [9].

Nowadays, computer simulation is an essential method to investigate and predict the complex multiphysics in metal 3D printing process. The method is used to replace the trial and error method due to its lower operating cost compared to that of the trial and error method [10]. The example of complex multiphysics in metal 3D printing process can be predicted by computer simulation methods such as temperature distribution, fluid dynamic, and melt pool characteristics [10].

The aim of this thesis is to study the metal 3D printing technology and the laser powder fusion additive manufacturing process. The work in thesis is divided into two parts. The first part of the thesis is the study the effect of laser process parameters on physical phenomena in L-PBF process including temperature distribution, melt pool geometry, single track formation and layer formation of the stainless steels including AISI 304, AISI 420 and AISI 316L by using the computer simulation method. The second part is the experimental study which focuses on the effect of laser process parameters including scanning speed and hatch spacing (the distance between laser scanning track) on the single track formation, layer formation, microstructure and microhardness of AISI 316L stainless steel fabricated by Laser powder bed fusion (L-PBF) process with low laser power (Max. 50 W). The results obtain from this study will be useful for the further research studies in metal 3D printing process in the coming future of the fourth industrial revolution in Thailand.

## **1.2. Objective of the study**

To study the effect of laser process parameters on physical phenomena, the microstructure and mechanical property of the stainless steels in L-PBF process by using the computer simulation method and experimental study.

## **1.3. Scopes of the study**

1. CFD computer simulation software ANSYS 18.1 and Flow-3D (Flow DEM and Flow-weld) are used to study the effect of laser process parameters on physical phenomena in L-PBF process including temperature distribution, melt pool geometry, single track formation and layer formation of the stainless steels.

2. Laser power, scanning speed, laser spot diameter, hatch spacing layer thickness and material properties are the main laser process parameters used in the computer simulation method.

3. Stainless steels with different grades including AISI 304, AISI 420 and AISI 316L are investigated in the computer simulation method.

4. The L-PBF system consists of laser source, which is used as the energy heat source in the experiment, building platform, gas chamber and argon inert gas shielding.

5. The varied laser process parameters used in the study are scanning speed, hatch spacing and layer thickness.

6. The melted track width of AISI 316L stainless steel fabricated by L-PBF process is investigated by Stereomicroscope.

7. The microstructure and alloying element analysis of the AISI 316L stainless steel fabricated by L-PBF process are characterized by optical microscope (OM) and scanning electron microscope (SEM) with EDS technique.

8. Micro Vickers hardness is used to analyse the microhardness of AISI 316L stainless steel in L-PBF process.

9. The results obtained from the computer simulation method are validated with the experimental results.

## **1.4. Expected Benefits of the study**

1. Gaining a fuller and a crucial body of knowledge of the constitutional of metal 3D printing and laser powder bed fusion (L-PBF) additive manufacturing process

2. Obtaining the computer simulation results of process parameters effect on the physical phenomena, single track formation, layer formation in L-PBF process of the stainless steels

3. Obtaining the experimental results of laser process parameters effect on single track formation and layer formation of AISI 316L stainless steel fabricated by L-PBF process

4. Obtaining the results of the microstructure and the microhardness of AISI 316L stainless steel fabricated by L-PBF process

## Chapter 2 Theory and Literature review

### 2.1. Classification of Additive Manufacturing (AM) process

Additive manufacturing (AM) process is defined by American Society for Testing and Materials (ASTM) as a process of joining materials to create products from 3D cad model, usually layer upon layer, as opposed to subtractive manufacturing, e.g. milling, turning and drilling [3]. AM process has been developed for more than 20 years [8] since the advent of stereolithography, a form of 3-D printing technology, in mid 1980s [4]. In 1997, AeroMat can produce the first additive manufactured metal by using high-power laser to melt titanium alloy powder [7]. Recently, AM process began to rise a significant in commercial manufacturing technology [3].

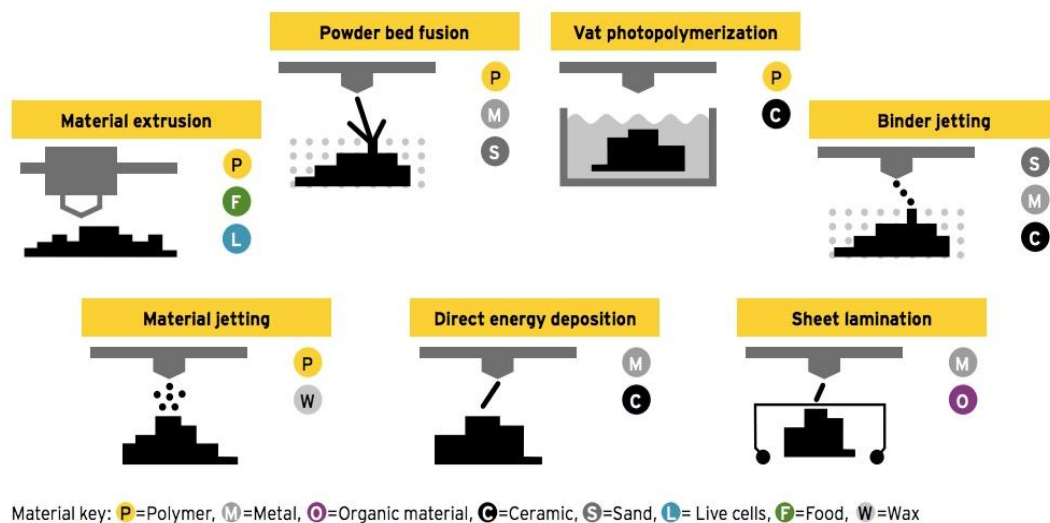


**Figure 2.1 Types of additive manufacturing process [11]**

Figure 2.1 presents the additive manufacturing process which seven methods are classified as follows: (1) Material extrusion (2) Powder bed fusion (3) Vat photopolymerization (4) Materials jetting (5) Binder jetting (6) Direct energy deposition (7) Sheet lamination [7].

All these methods are usually used to build the materials as layer-by-layer fashion from a 3D CAD-model. Powder bed fusion, binder jetting, direct energy deposition and sheet lamination methods were applied in metal industry [12]. When

using the binder jetting, green body from the process need to be sintered in an atmosphere furnace for near full density and strong mechanical properties [12,13,14].

## 2.2. Laser Powder Bed Fusion (L-PBF) process

Laser Powder Bed Fusion (L-PBF) process is a type of additive manufacturing process, which use laser as a heat source for fully melting metal powder to create 3D part layer fashion [6]. Figure 2.2 shows the schematic of laser powder bed fusion process. In this process, the powder bed is created by raking metal powder across the work space [3]. An energy source of laser is used to scan on each layer of metal powder bed to selectively melt the material according to the part cross section obtained from the CAD model. After one layer has been scanned, the piston under the product goes downward and the piston of the powder delivery goes upward by defined layer thickness. The cycle is repeated layer by layer, until the complete part is formed. Finally, the part is visible after the eliminated the excess metal powder from powder cake [6]. Usually the L-PBF process is conducted in an inert atmosphere such as Argon or Nitrogen for shielding of the molten metal.

Generally, most of the L-PBF process use laser energy 50 W to 1 KW capacity to selectively fuse the powder bed layer. The main parameters of this process are laser power, scan speed, hatch spacing, and the layer thickness [8]. The process can manufacture full density metallic parts from metal alloys e.g. titanium alloys, inconel alloys, cobalt chrome, aluminium alloys, stainless steels and tool steels [8].

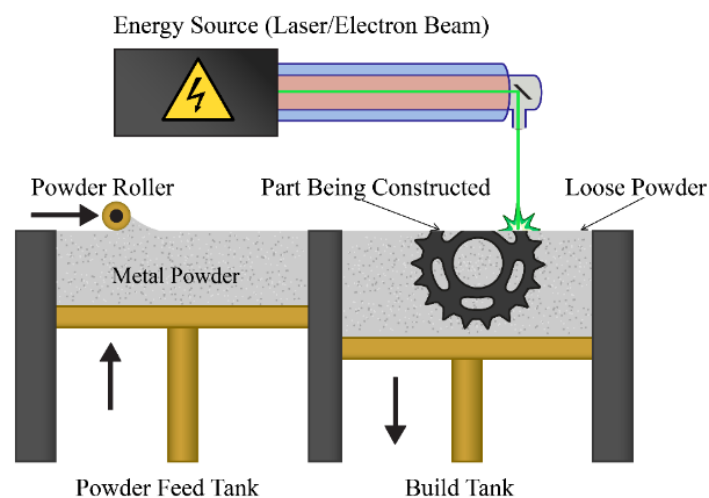


**Figure 2.2 Schematic of laser powder bed fusion process [15]**

### *Laser Source Energy Characteristics*

The laser beam characteristics have a significant effect on the temperature distribution in L-PBF. Several research studies related to the laser beam characteristics shows that the simplest laser beam has been assumed to be a point source. It was found that the laser beam can be characterized using three parameters: laser spot diameter, laser power, and power intensity [16]. The most widely used model is called Gaussian laser beam distribution which utilizes the symmetrical distribution of laser irradiance across the beam [17]. Figure 2.3 [18] illustrates an example of laser beam intensity profile with Gaussian distribution.

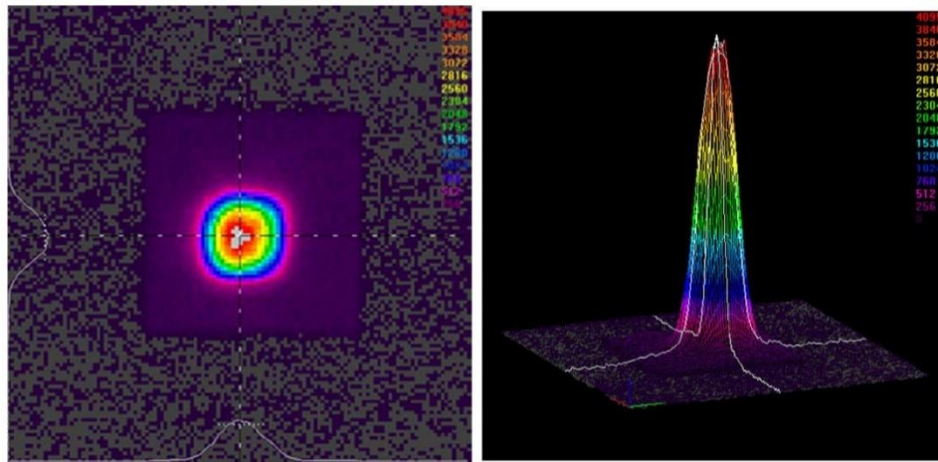


**Figure 2.3 An example of laser beam profiles with Gaussian distribution [18]**

The Equation of the laser beam irradiance at any point is defined as [17]

$$I(r) = I_0 e^{-2d^2/d_1^2} \quad (2.1)$$

$I_0$  is the maximum irradiance (power per unit area) at the center of the beam,  $d_1$  is the beam diameter corresponding to the point where the irradiance diminishes to  $1/e^2$  and  $d$  the diametrical distance of a point from the center. The laser heat flux can be described as follows:

$$q(r) = \frac{2P}{\pi r_0^2} e^{-2r^2/r_0^2} \quad (2.2)$$

$P$  is the laser power,  $r_0$  the spot radius and  $r$  the radial distance.

### *Laser-Material Interaction*

Laser-material interaction is a physical phenomena of materials which can occur when the laser beam interacts with the surface of metal powder in L-PBF process. It depends on laser parameters, laser beam absorption, reflective index, type of materials and the size of powder [19]. Figure 2.4 [20] shows the relationship of absorption rate of materials and wavelength. It can be seen that the wavelength of laser beam has a significant effect on absorption rate of materials. For instance, when using the CO<sub>2</sub> laser with wavelength 10.6  $\mu\text{m}$ , the iron can absorb the laser energy 6% of total laser energy, whereas Nd:YAG laser with the wavelength 1.06  $\mu\text{m}$ , the iron can absorb the laser energy around 30%. When the laser energy is absorbed and converted into heat energy on the surface of the material, the heat energy will distribute to the surrounding area. The materials are fused at above the melting point, thereby leading to the occurrence of the heat-affected zone in the adjacent area. Consequently, the microstructure transformation of the materials will be occurred [20].

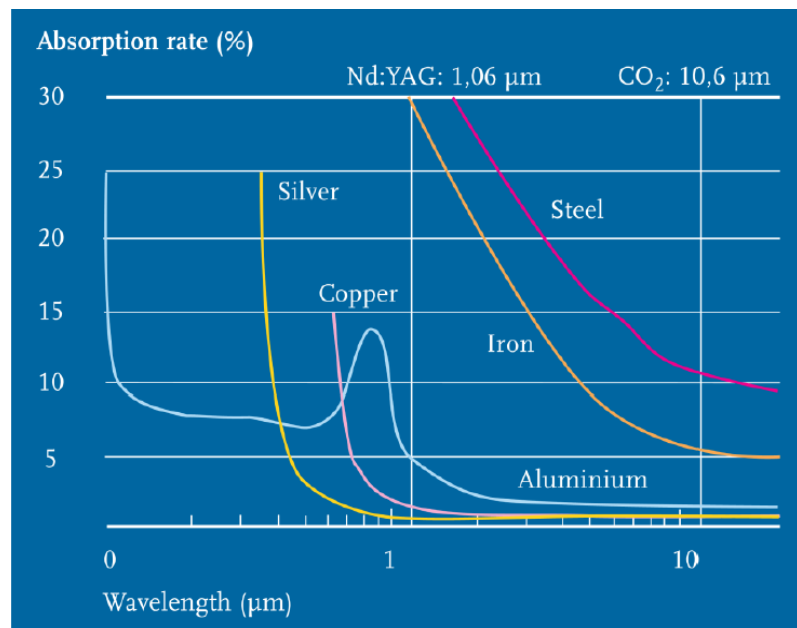


**Figure 2.4 Relationship of absorption rate of materials and wavelength [20]**

### *Heat transfer and fluid dynamic in L-PBF process*

L-PBF process involves with the complex multiphysics such as laser beam absorption, heat transfer, molten melt flow, phase transformation, rapid melting, rapid solidification thermal stress and distortion etc. These factors influence the final build quality and properties [9].

### *Heat Transfer in L-PBF process*

In the L-PBF process, a complicate thermal history takes place in the metallic AM part and involves with directional heat extraction, repeated rapid melting and rapid solidification [21, 22]. Heat transfer models are quite complex due to the laser scanning rates and material transformations occur in a short period of time [16]. Figure 2.5 shows the schematic of heat transfer in L-PBF process. The heat transfer process consists of powder bed radiation, convection, and heat conduction inside the powder bed and between the powder bed and substrate. During the process, the metal powder is transformed into liquid and finally to solid in a short time [17]. These large thermal gradients cause residual stresses and thermal distortion [16].

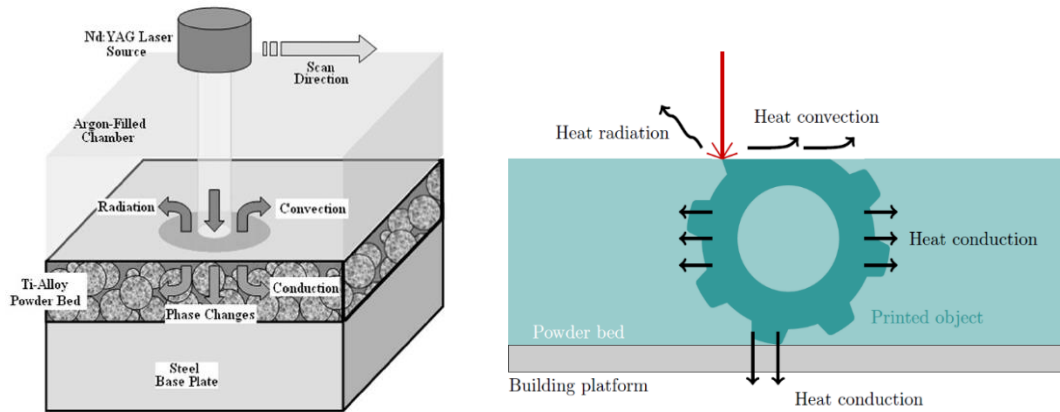


**Figure 2.5 Schematic representation of heat transfer in L-PBF process [17, 23]**

By the first law of thermodynamics, the general energy balance in the closed system can be written as shown in Equation (2.3) [17]

$$Q_L = Q_{CD} + Q_{CV} + Q_R \quad (2.3)$$

$Q_L$ ,  $Q_{CD}$ ,  $Q_{CV}$  and  $Q_R$  are the vector heat quantities for the laser flux, conduction, convection losses and radiation losses, respectively.

Fourier heat conduction is the most common Equation used to simulate a heat transfer process in L-PBF thermal field. The governing Equation for heat conduction is described in Equation (2.4) [24]. Equations (2.5), (2.6) and (2.7) are the initial and boundary conditions respectively.

$$\lambda \left( \frac{\partial^2 T}{\partial x^2} + \frac{\partial^2 T}{\partial y^2} + \frac{\partial^2 T}{\partial z^2} \right) + q = \rho c \frac{\partial T}{\partial t} \quad (2.4)$$

$$T(x, y, z) = T_0 \quad (2.5)$$

Boundary conditions:

Surface convection and radiation:

$$-\lambda \frac{\partial T}{\partial z} = \varepsilon_{\theta} \sigma (T^4 - T_e^4) + h(T - T_e) \quad (2.6)$$

$$\text{No heat loss at the bottom: } -\lambda \frac{\partial T}{\partial z} = 0 \quad (2.7)$$

$T$  is the temperature,  $\lambda$  is the conductivity coefficient,  $\rho$  is the density,  $c$  is the heat capacity coefficient,  $q$  is the internal heat,  $T_0$  is the powder bed initial temperature,  $T_e$  is the environment temperature,  $\varepsilon_{\theta}$  is the thermal radiation coefficient  $\sigma$  is the Stefan-Boltzmann constant, and  $h$  is the convection heat transfer coefficient.

Considering the melting and solidification phenomena, the enthalpy including latent heat evolution arising from phase change effect during the process can be described as [25]

$$H(T) = \rho \int_{T_0}^{T_s} C_p dT + \rho L_f + \int_{T_1}^T C_p dT \quad (2.8)$$

$T_s$  is the solidus temperature,  $\rho$  is the density,  $C_p$  is the specific heat capacity,  $L_f$  is the latent heat of fusion, and  $T_0$  is the room temperature.

### ***Fluid Dynamics and Marangoni Effect in L-PBF process***

Y.S. Lee and W. Zhang [9] developed the 3D transient simulation model of SLM, which is based on numerical solution of mass, energy and momentum conservation Equations as Equations (2.9), (2.10), (2.11). The volume of Fluid (VOF) method is used to track the position and shape of the molten pool surface as shown in Equation (2.12).

$$\text{Mass: } \nabla \cdot \vec{v} = 0 \quad (2.9)$$

$$\text{Energy: } \frac{\partial h}{\partial t} + (\vec{v} \cdot \nabla) h = \frac{1}{\rho} (\nabla \cdot \lambda \nabla T) \quad (2.10)$$

$$\text{Momentum: } \frac{\partial \vec{v}}{\partial t} + (\vec{v} \cdot \nabla) \vec{v} = -\frac{1}{\rho} \nabla P + \mu \nabla^2 \vec{v} + \vec{g} [1 - \beta(T - T_m)] \quad (2.11)$$

$\vec{v}$  is molten metal velocity,  $h$  is enthalpy,  $t$  is time,  $\rho$  is fluid density,  $T$  is temperature,  $\lambda$  is thermal conductivity,  $P$  is hydrodynamic pressure,  $\mu$  is viscosity,  $g$  is gravitational acceleration in  $z$  direction,  $\beta$  is coefficient of thermal expansion, and  $T_m$  is melting temperature of material.

$$\text{VOF: } \frac{\partial F}{\partial t} + \nabla \cdot (\vec{v}F) = 0 \quad (2.12)$$

A cell is void when  $F = 0$ , and completely occupied by the fluid when  $F = 1$ . When the value of  $F$  is between 0 and 1, an interface between the fluid and void exists in the cell

In [26], a model with the liquid motion in the melt pool was driven by capillary and gravity forces, and the flow characteristics have been formulated using Darcy's Law which describes the flow through a porous medium. In a previous research study [27], the model from [26] has been expanded to a three-dimensional model by considering the thermal behavior and fluid dynamics in the molten pool caused by buoyancy forces and Marangoni effect. Marangoni effect is the phenomena which relates to the mass transfer along an interface due to the surface tension gradient. In the melt pool, the strong temperature gradients at the laser hot spot cause surface tension which depends on temperature. An example of Equation which describes that relationship of 316L stainless steel is shown in Equation (2.14) [28].

$$\sigma(T) = \sigma_o - \frac{d\sigma}{dT}(T - T^*) \quad (2.13)$$

$\frac{d\sigma}{dT}$  is surface tension gradient,  $T$  is temperature in Kelvin. This creates Marangoni effects and drives the melt flow from the hot laser spot toward the cold rear, which could increase the melt depth, recirculate the melt flow.

$$\sigma(T) = 3.282 - 8.9e^{-4}T \quad (2.14)$$

### ***Melting and Solidification in L-PBF process***

The rapid melting and rapid solidification of material can generally occur in L-PBF process due to the laser scanning rates and material transformations occur in a very short time. The rapid melting and rapid solidification process began when the laser energy source interacts with the metal powder causing the melt pool, after that the rapid solidification of material can be occurred. The rapid melting and rapid

solidification in L-PBF process have a significant effect on the quality and mechanical properties of final products.

***Melt pool geometry and laser melted track.***

The melt pool shape is determined by laser process parameters and the thermal conditions in and near the melt pool [19]. It has an influence on the fusion zone grain structure. The shape of melt pool can change from ellipse shape to tear drop shape when scanning speed is increased as shown in Figure 2.6 [29].

The laser melted track is formed while the laser source is scanned along the laser path. The laser melted track in L-PBF process are classified into three types (1) discontinuous track with balling effect, (2) discontinuous track with fragment and (3) continuous track as shown in Figure 2.7 [19]. The geometric characteristics of laser melted tracks strongly depend on the laser process parameters such as laser power, scanning speed, layer thickness, working atmosphere and surface tension force of materials. Surface tension can be influenced by laser process parameters. [29].

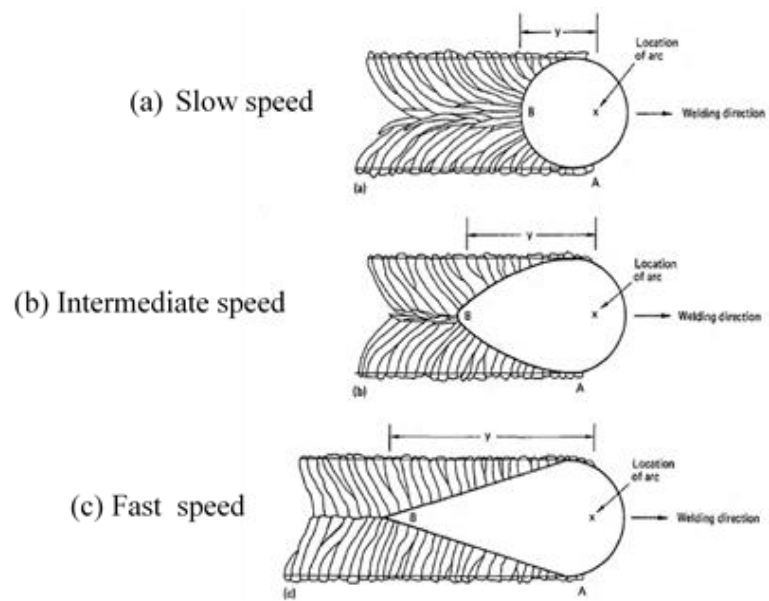


**Figure 2.6 Types of melt pools shape with difference scanning speed (a) slow, (b) intermediate, (c) fast [29]**

The discontinuous track with balling effect can expose when the lower laser power and high scanning speed are applied. This phenomena occur due to the insufficient of laser energy heat source to fully melt the metal powder bed in L-PBF process (a). The discontinuous track with fragment can be formed with the lower laser power and lower scanning speed. The laser melted track cannot completely melt and also caused high residual stress and cracks [30] (b). The continuous melted track can be formed when the properly laser process parameters are applied (e.g, higher laser power and slower scanning speed) [30] (c).

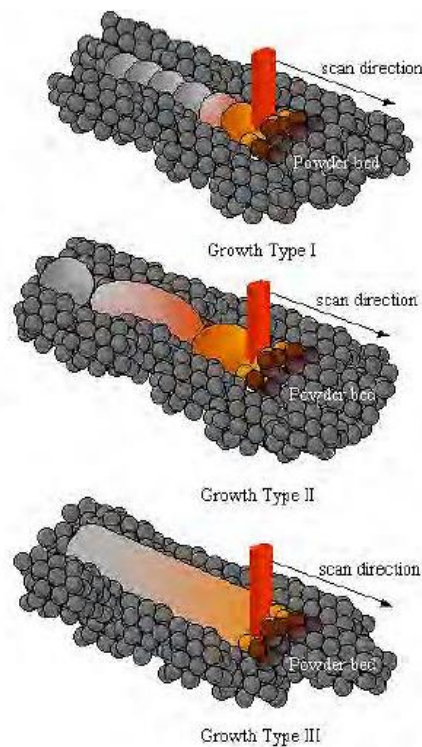


**Figure 2.7 Types of Single track formation [19]**

### ***Balling effect in L-PBF process***

The balling effect involves the wetting characteristics of solid powder. It can be described by the interfacial tensions. The wetting characteristics of solid powder relates with the surface tension of the liquid-vapor interface, solid-vapor interface and solid-liquid interface [31]. The equilibrium of surface tension is controlled by the contact angle, which is angle between the surface of solid powder and the tangent to the surface of the liquid as shown in Figure 2.8.

If contact angle ( $\theta$ ) is below  $90^\circ$ , the wettability can be improved. In contrast, if the contact angle ( $\theta$ ) is larger than  $90^\circ$  the wettability is limited.

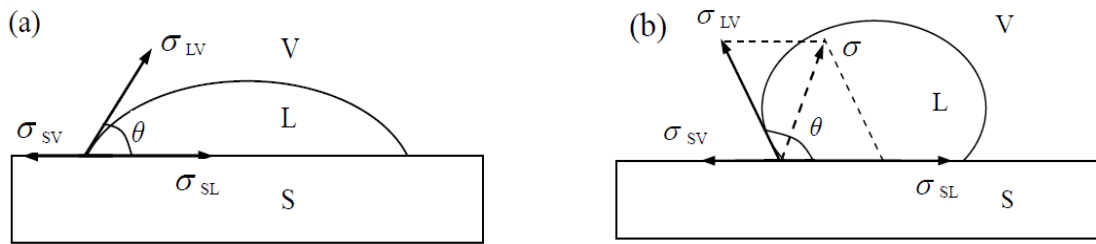


**Figure 2.8 Schematic of wetting characteristic (a) wetting system (b) non-wetting system [31]**

The contact angle is the angle measured between surface tension of liquid-vapor and surface tension of solid-liquid interface. Young Equation is used to calculate contact angle which can be expressed as

$$\cos \theta = \frac{\sigma_{SV} - \sigma_{SL}}{\sigma_{LV}} \quad (2.15)$$

Where  $\sigma_{SV}$  is surface tension of solid – vapor interface,  $\sigma_{SL}$  is surface tension of solid-liquid interface,  $\sigma_{LV}$  is surface tension of liquid-vapor interface and  $\theta$  is contact angle [31].

### ***The mechanism of balling effect***

The mechanism of balling effect is explained step by step as shown in Figure 2.9. When the incident laser heat energy is rapidly absorbed by the metal powder, the surface melting of the metal powder can be occurred. Consequently, a liquid phase can be formed between the metal powder adjacent, which reducing the surface area of powder and promoting the aggregating of metal powder. When then laser spot diameter is larger than the original powder size, metal powder can melt together and becoming to coarsening agglomerates. At lower surface tension, the balling shape of metal powder can be formed which has larger dimension than the original size [31].

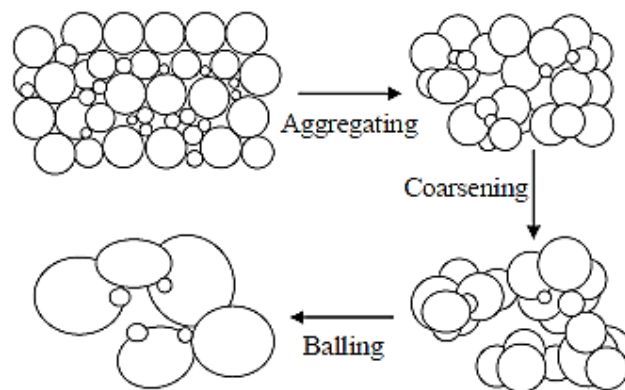


**Figure 2.9 Schematic of the balling effect mechanism in L-PBF process [31]**

### *Solidification in conventional process and L-PBF process*

After the construction of material melting, the material solidification can be formed. The solidification process involves with solidification parameters such as growth rate ( $R$ ), cooling rate, under cooling ( $\Delta T$ ), temperature gradients ( $G$ ) and alloys composition ( $C$ ) [29]. All these parameters have significant influence on solidified microstructure. The solidified microstructure can change from planar to cellular, columnar dendritic and equiaxed dendritic. All these microstructures are arised based on solidification theory [32]. The solidified microstructure is controlled by effects of ratio  $G/R$ . At the lower ratio of  $G/R$ , the columnar dendritic and equiaxed dendritic microstructure is formed and at higher ratio of  $G/R$  the planar and cellular microstructure can be formed [29]. Figure 2.10 shows the relationship of temperature gradient with growth rate on solidified microstructure.

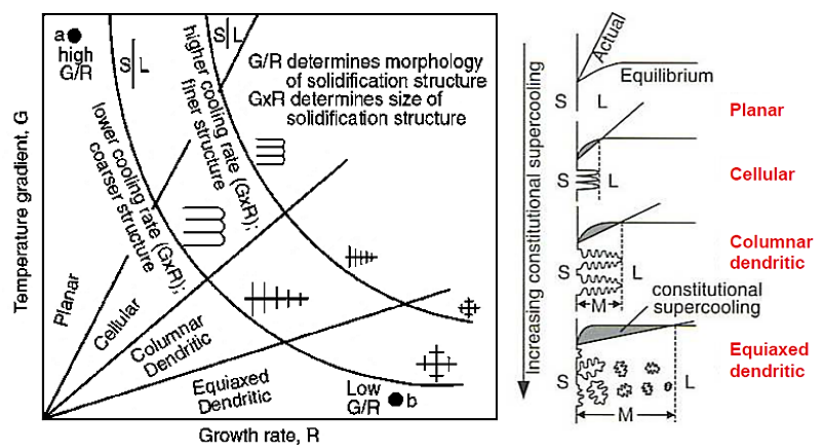


**Figure 2.10 The relationship of temperature gradient with growth rate on solidified microstructure [29]**

Solidification in the conventional process such as welding process and casting process, the mechanism of the solidification process occurs by nucleation and growth transformation. In nucleation and growth transformation, the nuclei of the solid phase are arised and grown to grain structure. In welding process, the weld microstructure depends on the solidification behavior of the weld pool which has effects on size and shape of grains, segregation and porosity. During the weld metal solidification, grains tend to grow perpendicularly towards the weld pool boundary along the maximum temperature gradient as shown in Figure 2.11 [33].

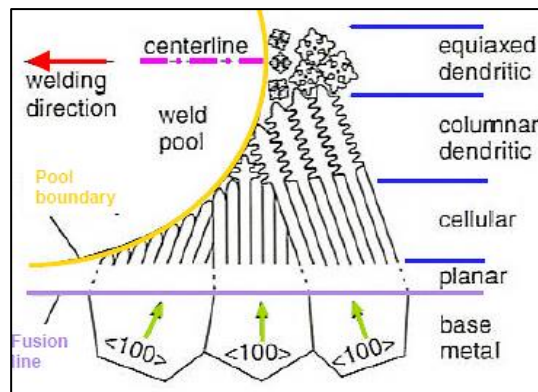


**Figure 2.11 Types of solidification structure in welding process [33]**

In casting process, after molten metal is poured in to mold, the solidified metal can takes place. The important parameters in the process are type of metal, thermal properties of mold and metal. A thermal gradient is perpendicular to the interface and opposite the heat flow direction during the solidification process [34] as shown in Figure 2.12. The thermal gradient increases into the liquid phase. This also depends on constitution supercooling also known as undercooling. The undercooling is the process of lowering the temperature of a liquid or a gas below its freezing point without it becoming a solid. Figure 2.13 presents the microstructure in casting process consist of chill zone, columnar zone and equiaxed zone.

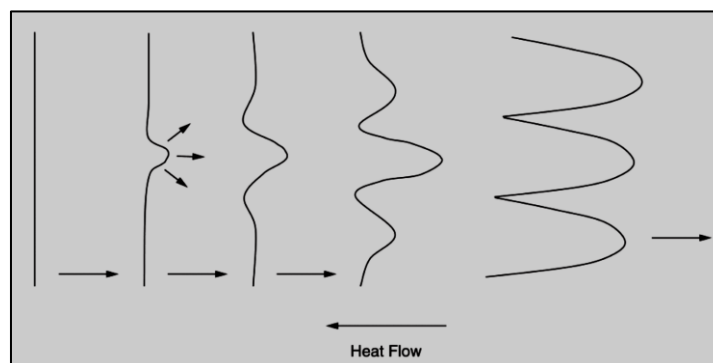


**Figure 2.12 Heat flow direction in solidification process [35]**

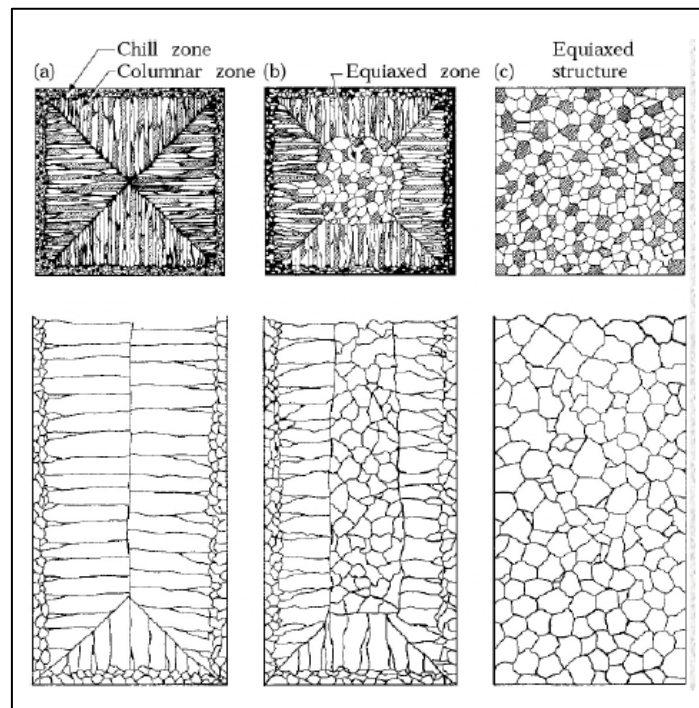


**Figure 2.13 Types of microstructure in casting process [36]**

For L-PBF process, the rapid microstructure solidification is formed by the effect of the temperature gradient ( $G$ ) and growth rate ( $R$ ). The ratio  $G/R$  is high enough to simplify planar and cellular grain growth. However, the repeat melting of the next layer will decrease the dendrites and equiaxed grains at the centerline of melt pool [37].

### **2.3. Stainless steel types (AISI 304, 316L and 420)**

Stainless steel is a low carbon high alloy steel. The main alloy elements consist of 10.5 to 30 % Cr, 8 to 20 % Ni and varied amount of Mo, C, Si, Mn, S, N and P. The features of stainless steel are excellent corrosion resistance, good formability, ductility and good wear resistance. It can be applied in various industries such as food processing, medical sector, automotive sector chemical and petroleum sector, etc. The stainless steel can be classified into five types: ferritic, austenitic, martensitic, duplex and super austenitic or hardening precipitate. Each type has a different chemical compositions and mechanical properties depending on contain of alloy elements [38].

***AISI 304 stainless steel***

AISI 304 stainless steel consists of 18 to 20 % Cr and 8 to 10.5 % Ni and varied amount of C, Si, Mn, S, N and P. It is the most common type of stainless steel used around the world. AISI 304 stainless steel has good corrosion resistance and formability. The typical applications are food processing equipment, kitchen benches, sinks, troughs, equipment and appliances [39]. The chemical compositions of AISI 304 are shown in Table 2.1.

**Table 2.1 Chemical composition (%wt.) of AISI 304 stainless steel [39]**

<b>Grade</b>	<b>C</b>	<b>Mn</b>	<b>Si</b>	<b>P</b>	<b>S</b>	<b>Cr</b>	<b>Mo</b>	<b>Ni</b>	<b>N</b>
304	0.08	2.00	0.75	0.045	0.030	20	-	10.5	0.01

***AISI 420 stainless steel***

AISI 420 stainless steel is a martensitic type which contains 12 to 14 percent chromium and high carbon. This form of stainless steel can be hardened by heat treatment process. In the hardened condition, AISI 420 has high strength, high hardness and good corrosion resistance to the atmosphere, fresh water, crude oil, and good wear resistance [40]. AISI 420 is commonly used for surgical equipment, turbine blade and plastic injection mold. The chemical composition of AISI 420 martensitic stainless steel are shown in Table 2.2.

**Table 2.2 Chemical composition (%wt.) of AISI 420 martensitic stainless steel [40]**

<b>Grade</b>	<b>C</b>	<b>Mn</b>	<b>Si</b>	<b>P</b>	<b>S</b>	<b>Cr</b>	<b>Mo</b>	<b>Ni</b>	<b>N</b>
420	0.15	1.00	1.00	0.040	0.033	14	-	-	-

### *AISI 316L stainless steel*

AISI 316L stainless steel is an austenitic stainless steel that contains 16 to 18 % wt. Cr and 10 to 14 % wt. Ni. This type of stainless steel provides excellent corrosion resistance. It also has good ductility, toughness, weldability and formability. The AISI 316L austenitic stainless steel cannot be hardened by heat treatment process due to low carbon. AISI 316L austenitic stainless steel is widely used in various industries such as food industry, chemical industry, and medical sector. It is useful in many applications, for instance, food processing equipment, kitchenware, chemical storage tank, and medical equipment. The chemical compositions and mechanical properties of AISI 316L austenitic stainless steel are shown in Table 2.3 and 2.4. [41].

**Table 2.3 The chemical compositions (%wt.) of AISI 316L stainless steel [41]**

Type	C	Mn	Si	P	S	Cr	Mo	Ni	N
AISI 316L	0.03	2	1	0.045	0.015	16-18	2-3	10-14	0.03

**Table 2.4 Mechanical properties of AISI 316L stainless steel [41]**

Type	Tensile stress (MPa)	Yield stress (MPa)	Elongation (%)	Hardness Rockwell B (HRB)	Hardness Brinell (HB)
AISI 316L	485	170	40	95	217

## **2.4. Microstructural evolution of AISI 316L stainless steel**

### *Basis microstructure of AISI 316L stainless steel*

The microstructure of AISI 316L austenitic stainless steel is an austenite phase, which is face center cubic structure (F.C.C) and nonmagnetic. The austenite phase can be formed during the solid state transformation of ferrite, or solidification with austenite stabilizer elements such as Ni, Mn, Si and C [42]. Figure 2.14 represents the ternary phase diagram of austenitic stainless steel grades.

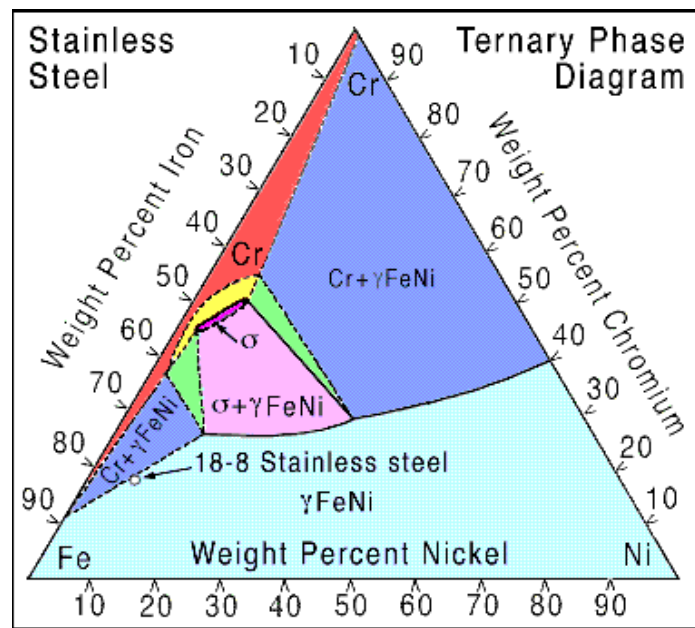


Figure 2.14 The ternary phase diagram of AISI 316L stainless steel [43]

### *The solidification modes of austenitic stainless steel*

The solidification modes of austenitic stainless steel can be divided to four modes including austenitic (A), austenitic-ferritic (AF), ferritic–austenitic (FA) and ferritic (F) [19]. The solidification modes have a significant effect on the microstructural evolution of austenitic stainless steel. The solidification of austenitic stainless steel modes depends on the ratio of the equivalent chromium [Cr] and equivalent nickel [Ni] as described in Equation (2.16) and (2.17) [44]. Figure 2.15 shows the relationship between the solidification modes with  $Cr_{eq}/Ni_{eq}$  and microstructure.

$$[Cr]_{eq} = \%Cr + \%Mo + 1.5\%Si + 0.5\%Nb + 2\%Ti \quad (2.16)$$

$$[Ni]_{eq} = \%Ni + 0.5\%Mn + 30\%C \quad (2.17)$$

Figure 2.16 illustrates the Schaeffler diagram. It is often used to predict the influence of chemical composition alloy elements on microstructural evolution in welding process by using the equivalent chromium [Cr] and equivalent nickel [Ni] [45, 46]

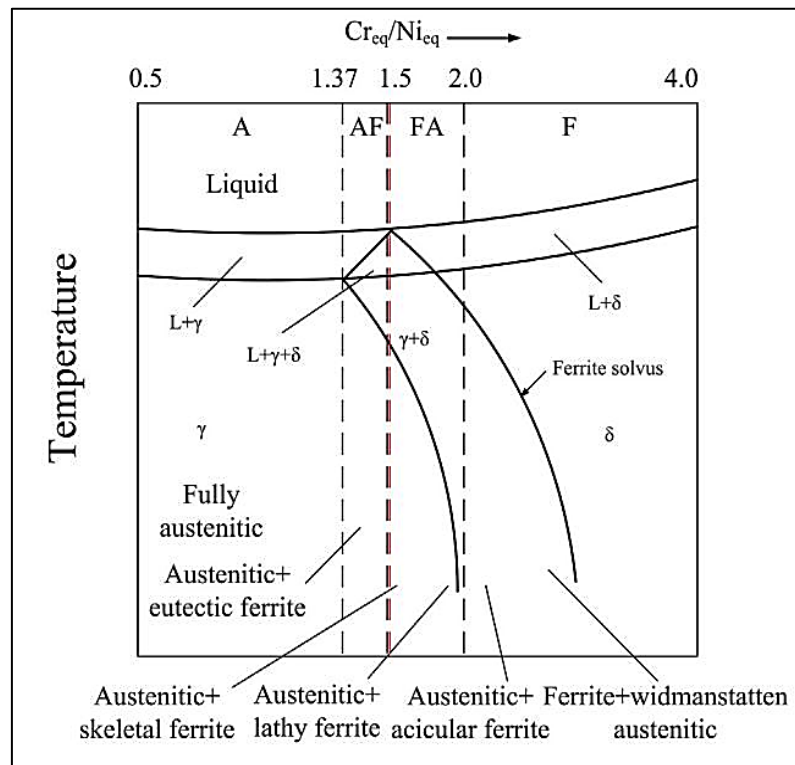


Figure 2.15 The relationship between the solidification modes with  $C_{req}/Ni_{eq}$  and microstructure [44]

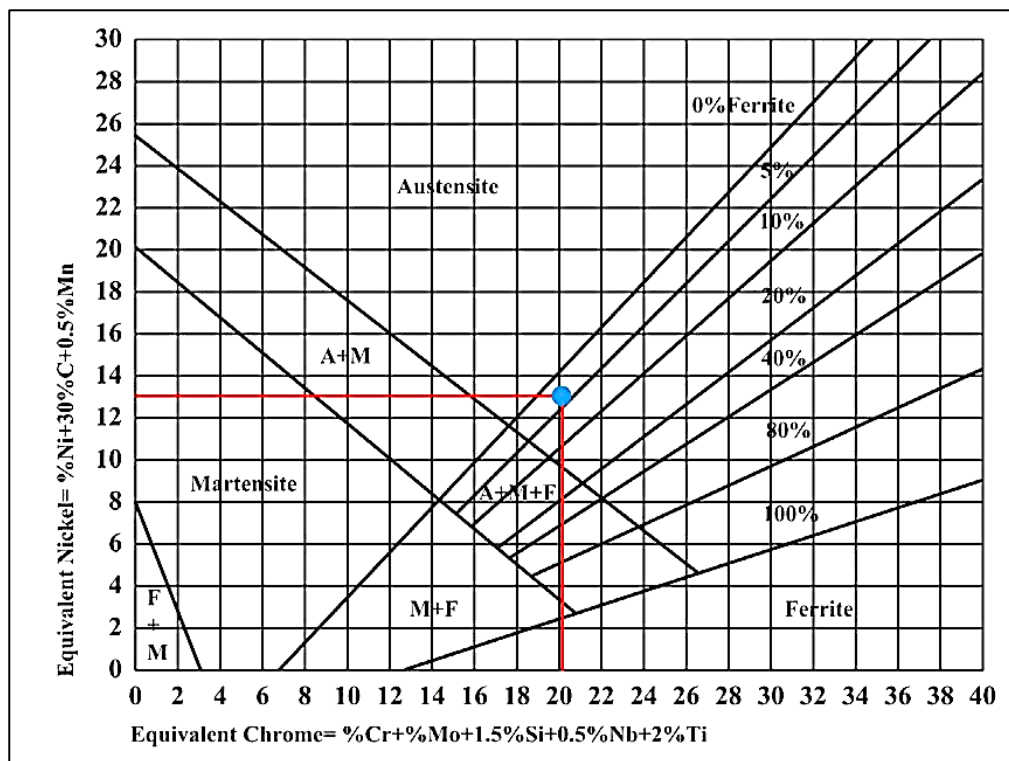
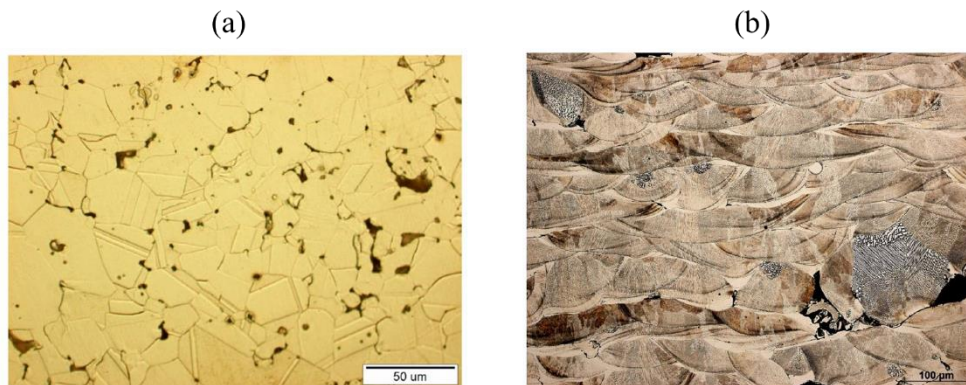


Figure 2.16 The Shaefler diagram [44]

***The influence of rapid cooling rate on the microstructure of AISI 316L stainless steel***

The cooling rate in solidification process of metal is classified into low, medium and high cooling rates. These parameters play a significant role in the evolution of stainless steel microstructure. At the low cooling rates ( $10^{-1}$  to  $10^1$  K/s) and medium cooling rates ( $10^1$  to  $10^3$  K/s) have minor effects on microstructure transformation. Whereas, high cooling rates ( $10^2$  to  $10^7$  K/s) has a significant effect on the solidification process in which different the microstructure transformation can be occurred. Examples of process that cause high cooling rate are laser beam welding and electron beam welding [47, 48]. In L-PBF process, the rapid melting, rapid solidification, rapid cooling rate and the micro melt pools can be formed in microstructure [37]. The rapid cooling rate is a major influence in non-equilibrium phase and refinement of grain. L-PBF process has different heat transfer mechanism from the conventional process such as casting, welding, and forming [49, 50]. The microstructure of L-PBF process consists of melt pools, fine grain and sub grain structure [51]. The cellular-columnar structure is general microstructure of AISI 316L stainless steel solidified under rapid cooling rate [52]. The comparison of AISI 316L microstructure at low cooling rate and rapid cooling rate is shown in Figure 2.17 (a), (b).



**Figure 2.17 The comparison of AISI 316L microstructure at (a) low cooling rate and (b) rapid cooling rate [52]**

## **2.5. Laser powder bed fusion of AISI 316L stainless steel**

Laser powder bed fusion additive manufacturing of AISI 316L stainless steel has been studied by several researchers [53]. There has been more than 100 publications on the L-PBF of metal alloy steel since 2003. Most of the publications on

metal alloys are based on AISI 316L stainless steel [53]. Jandin et al. [54] reported the first paper of AISI 316L stainless steel was fabricated by L-PBF process. The result showed the incomplete melting and high porosity of metal powder when using low laser power and high scanning speed. However, it was not success. Until 2010, Tolosa et al. reported the achieved 99.9 % of relative density with L-PBF process of AISI 316L stainless steel [55]. I. Yadroitsev and I. Smurov [56] studied the effect of process parameters such as laser power, scanning speed and layer thickness on the laser tracks formation of AISI 316L. It was found that the stability zones occur when the melted track is continuous and instability can be formed when the tracks are not continuous. The results showed that the continuous of single track could be appeared by using the proper laser power and scanning speed. R. Li et al. studied the effect of scanning speed on balling behaviour of AISI 316L. They found that the scanning track widths are narrowed gradually when the laser scanning speed increases [57]. The balling effect can be classified into two types including the ellipsoidal balls with dimension of about 500  $\mu\text{m}$  and the spherical balls with dimension of about 10  $\mu\text{m}$ . The balling effect can be controlled by effect of process parameter such as laser power, scanning speed and the oxygen content in atmosphere. I. Yadroitsev and I. Smurov investigated the effect of hatch distance on surface morphology during selective laser melting. The process parameters used in the study were laser power with 50 W and the scanning speed with 0.14 m/s. The varied hatch spacing are from 60 up to 280  $\mu\text{m}$  with a step of 20  $\mu\text{m}$ . They summarized that the aperture between two neighboring tracks is increased and leads to separation with an increase of hatch spacing [58]. R. Li et al [59] studied the gradient porosity of AISI 316L stainless steel fabricated by L-PBF process. The results showed that the porosity is strongly influenced by scan speed. The results indicate that the structure exhibits a gradually increased porosity and a reduced molten pool size along the gradient direction of scan speed variation. J.A. Cherry et al [60]. investigated the effect of process parameters on the microstructural and mechanical properties of 316L stainless steel parts by selective laser melting. The results reveal that the hardness of material increases when the porosity is decreased. V. Sufiiarov et al. studied the selective laser melting process of AISI 316L powder. The results from the study show that the laser powder bed fusion process can produce parts with higher mechanical properties than that of the conventional manufacturer [61]. Moreover, the mechanical properties in L-PBF process are higher than conventionally manufactured such as forging, casting and machining due to rapid cooling and the fine cellular sub-

grain microstructure. The fine cellular sub grain microstructure can be formed at the high solidification [62, 63]. J.P. Choi et al [64] investigated the densification behavior of AISI 316L stainless steel parts fabricated by selective laser melting by variation in laser energy density. It was found that the densification behavior of SLM processed SS316L parts was controlled by effect laser energy density (E). In the study, the AISI 316L parts with a microhardness of 240 Hv, UTS of 570 MPa, EL of 40%, and  $\sigma_{0.2}$  of 530 MPa were achieved by using the laser energy density of 58.4 J/mm<sup>3</sup>. The mechanical properties of AISI 316L stainless steel fabricated by L-PBF process compared with the conventional method is presented in Table 2.5.

**Table 2.5 The comparison of mechanical properties of AISI 316L stainless steel fabricated by L-PBF process and the conventional method [7]**

Specimens	Yield stress (MPa)	UTS (MPa)	Elongation (%)	References
L-PBF	532	573	41	J.P.choi
AS-cast	262	552	55	43
Wrought (cold finish)	155	525-623	30	43
Wrought (hot finish)	170	480	40	

Z. Brytan [52] reported the comparison of vacuum sintered with selective laser melting process of AISI 316L stainless steel. The results present that applications of selective laser melting (SLM) make it possible to double increase the mechanical properties of components manufactured from austenitic stainless steel type AISI 316L compared to sintering in a vacuum. The materials microstructure from L-PBF process generally consist of overlapped melted pool tracks with crystallised grains of cellular-columnar structure oriented according to thermal gradient direction. The cellular-columnar microstructure is typical for AISI 316L stainless steel solidified under rapid cooling rate and rapid solidification. The cellular sub-grains have the same orientation within the same coarse grain. Whereas, the cellular sub-grains are oriented in different directions among the coarser grains. This is due to the change in direction of the heat flux and the temperature gradients during melting. The typical of defects in L-PBF process are voids between melted pools of different size, unmelted powder particles,

small spherical porosity preferentially located between molten pools. An example of microstructure with typical defects of AISI 316L is shown in Figure 2.18 [52].

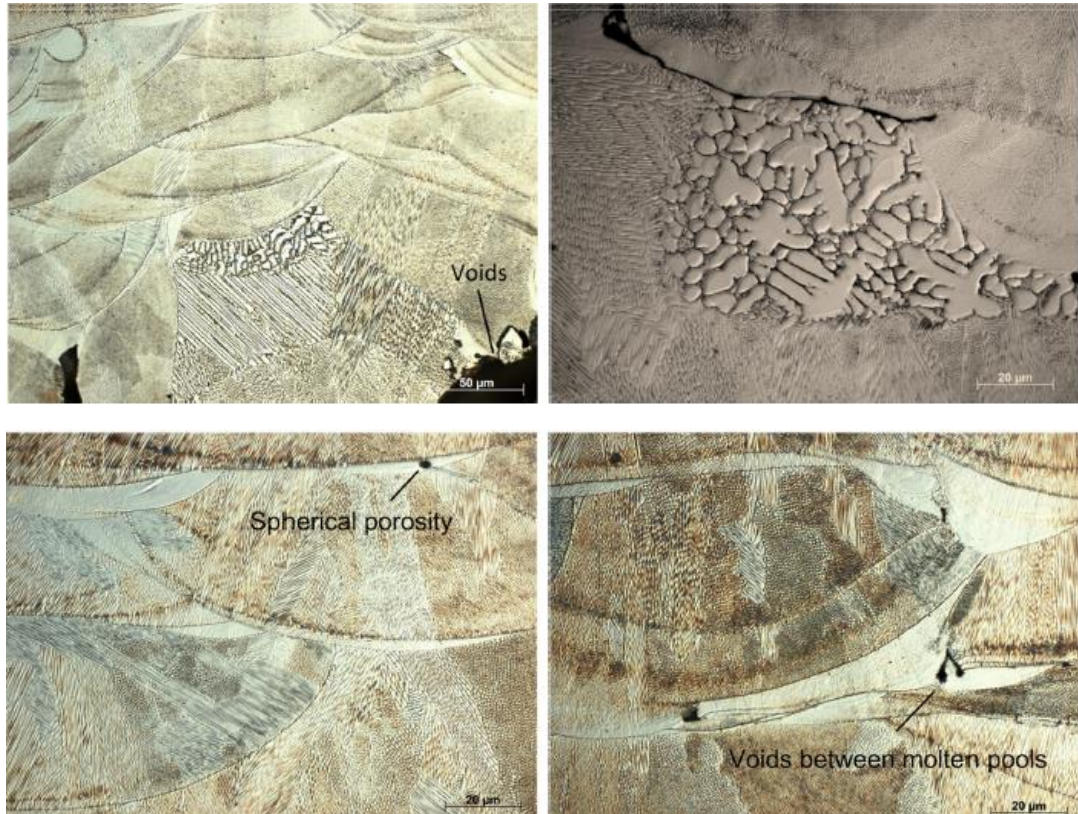


**Figure 2.18** An example of microstructure with typical defects [52]

## 2.6. Numerical modelling in L-BPF Process

Several researchers [65, 66, 67, 68] have investigated and built models to simulate the temperature distribution, Molten fluid flow, melting solidification and melted track characteristic phenomena. Y. Li and D. Gu [69] developed a 3D model to study the thermal behavior of L-PBF process of pure titanium powder. The study considers the temperature-dependent thermos physical parameters and the Gaussian distribution of the heat flux. In the study, they found that: (1) the average temperature of the powder bed gradually increased during laser scanning because of the heat accumulation, (2) the maximum temperature gradient in the molten pool increased slightly when the scan speed was increased from 50 to 200 mm/s, but increased significantly when the laser power was increased from 100 to 200 W, (3) the width and depth of the melt pool decreased when scan speed was increased from 50 to 200 mm/s, (4) the microstructure was investigated to verify the reliability of the physical model and there was less balling and pore formation with power 150 W and speed 100 mm/s

which are the optimum condition for liquid formation and wettability in this case. Figure 2.19 shows an example of mesh and temperature distribution during L-PBF process simulation with power 100 W and scanning speed 100 mm/s. Figure 2.20 shows the influence of the scan speed (a) and laser power (b) on the width and depth of the molten pool. Figure 2.19 (c) shows an example of SEM images of surface morphology of L-PBF-processed Ti sample with laser power 150 W and scanning speed 100 mm/s.

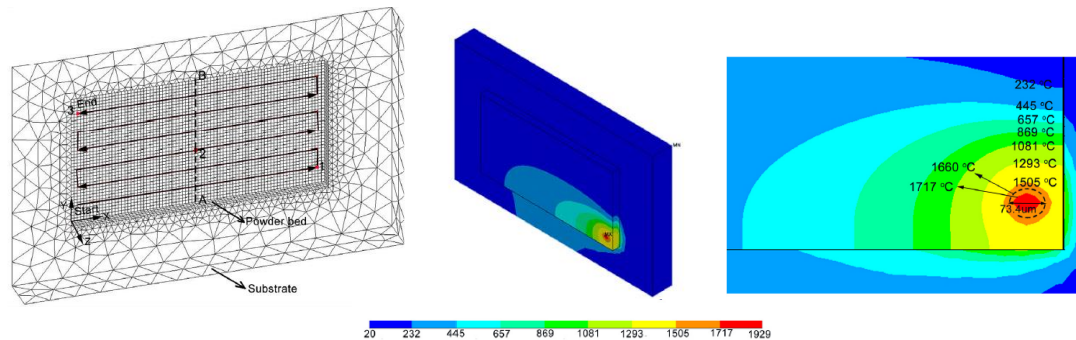


**Figure 2.19** An example of temperature distribution during L-PBF process with power 100 W and scanning speed 100 mm/s [69]

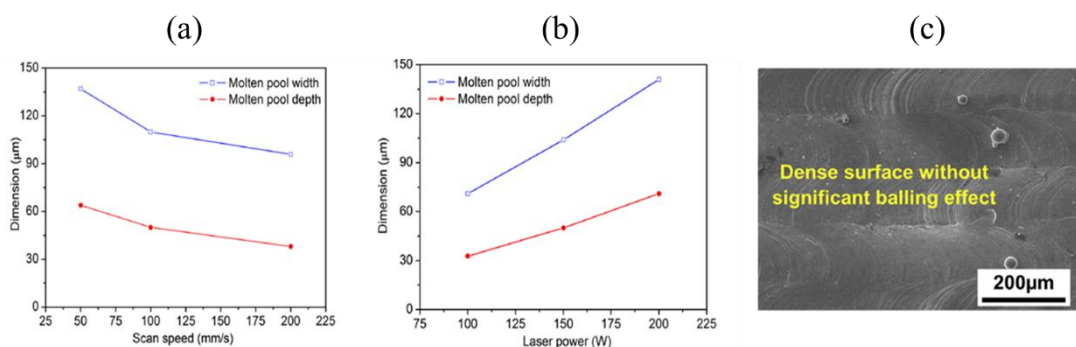


**Figure 2.20** The influence of the scan speed (a) and laser power (b) on the width and depth of the molten pool An example of SEM images of surface morphology of L-PBF-processed Ti sample with laser power 150 W and scanning speed 100 mm/s (c) [69]

Y.S. Lee and W. Zhang [9] solved the 3D transient numerical mesoscale model of Inconel 718 powder bed with a mesh size of 3 micron considering the volume of fluid method (VOF), Marangoni effect, particle size distribution and packing density. Figure 2.21 presents the results of molten pool simulation with scanning speed 1.1 m/s, laser power 150 W and packing density 45%. A commercial software Flow-3D was used in this work. From this study, they found that too fast scanning speed and too low

laser power can increase the chance of discontinuous molten pool and the balling effect.

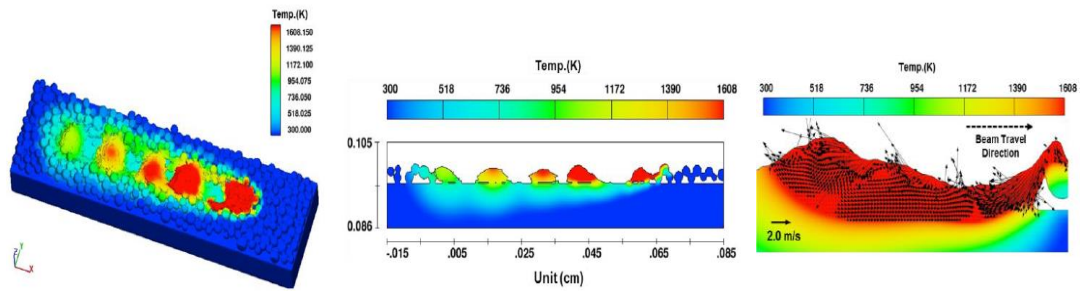


**Figure 2.21 The results of molten pool simulation with scanning speed 1.1 m/s, laser power 150 W and packing density 45% [9]**

N. P. Lavery et al. [70] conducted a review of Computational Modelling Additive Layer Manufacturing – multi-scale and multi-physics. The results from the microscale model simulation using FLUENT software indicated that the laser beam energy source was modelled using a moving source term along the top boundary with the Discrete Ordinate radiative heat transfer model which had to be programmed in FLUENT using User Defined Functions (UDFs). The model considers melting and solidification by using an enthalpy-porosity technique [71]. A metal powder melt pool modelling using FLUENT is illustrated in Figure 2.22 below.

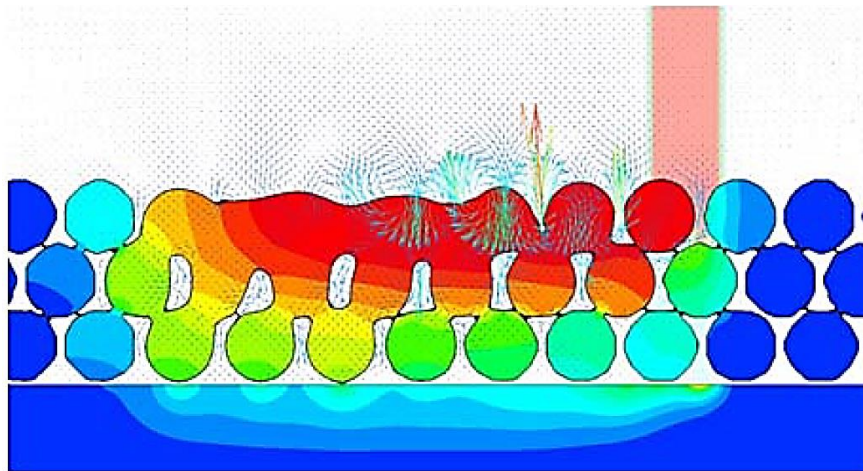


**Figure 2.22 A metal powder melt pool modelling using FLUENT software [70]**

K.-H. Leitz [72] studied the physical phenomena of L-PBF process using by COMSOL Multiphysics with *Computational Fluid Dynamics* and the *Heat Transfer* module. It was found that the computer simulation can be used to explain the melt pools and molten fluid flow characteristic. Molten fluid flow characteristic of steel powder bed in SLM process is shown in Figure 2.23.

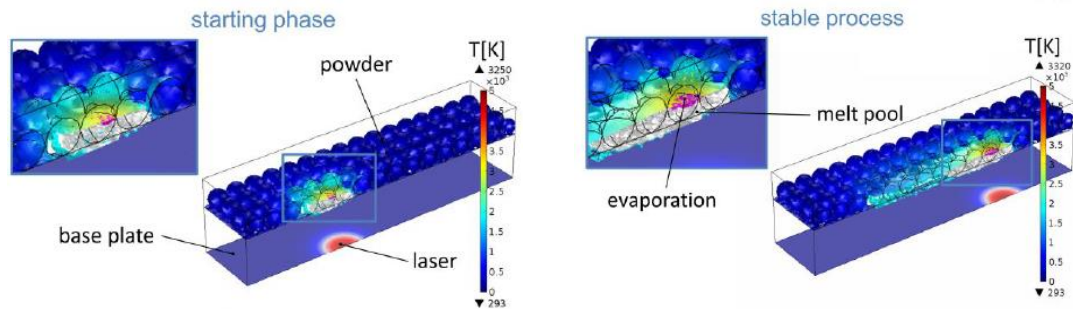


**Figure 2.23 Molten fluid flow characteristic of steel powder in SLM process [72]**

Y.C.Wu et al. [73] developed a three-dimensional (3D) numerical model for parametric study of surface morphology for selective laser melting (SLM) on Ti6Al4V powder bed with numerical and experimental method. They found that the results of the numerical model were verified experimentally, and demonstrated to have good accuracy. The surface morphology after laser melting was calculated by the VOF technique. As the laser power increases, the surface morphology roughens; however, with increasing scanning speed, the surface morphology initially becomes smoother and then roughens again. The melt track width in SLM can be decreased with an increased scanning speed. Figure 2.24 shows the comparison of the simulation results and the experiment results.

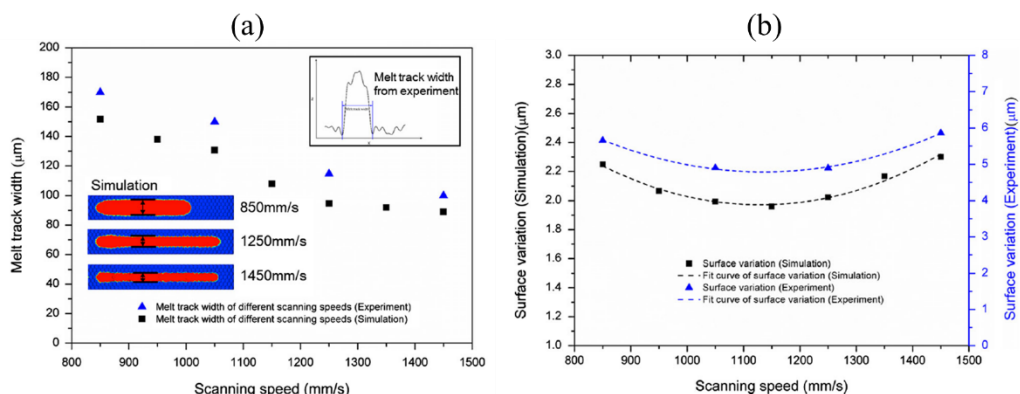


**Figure 2.24 Comparison of simulation results and experiment results [73]**

Although great efforts have been put into the field of L-PBF thermal analysis by many researches, but there are still many areas of improvement required in this

numerical modeling as well as in the experimental measurement and control side. Better understanding of the input energy model including laser beam power distribution and effect of process parameters on the temperature field and molten pool characteristics of various kinds of metal powder bed are still needed. The investigation of relationship between process parameters and temperature field by numerical studies will provide clearer comprehension which can be beneficial to the improvement of the L-PBF process optimization. In addition, the information of temperature field will be useful for the simulation of the thermal-stress model and for the prediction of the mechanical properties, microstructure transformation and part distortion in the future work.

## **2.7. Other metal additive manufacturing**

Over the past two decades, metal additive manufacturing (AM) has evolved from 3D printer to create the rapid prototype. The AM technologies used in metal industry are material extrusion, laser powder bed fusion or selective laser melting, binder jetting, and direct energy deposition. In terms of applications, AM process has been widely used in the development of the final parts in aerospace sector, automotive sector, jig and fixture and medical sector. L-PBF process has been described in section 2.2.

### ***Material Extrusion***

Material extrusion process has a similar operation method to that of metal injection molding (MIM). The material extrusion process begins with mixing the metal powder with polymer binder. Then, the materials are extruded through the nozzle to create the 3D parts layer fashion. The advantage of this technique simplified with this new technology is to provide a safe working environment where the operators can work without excess metal powder. Figure 2.25 shows the schematic of materials extrusion process [74].

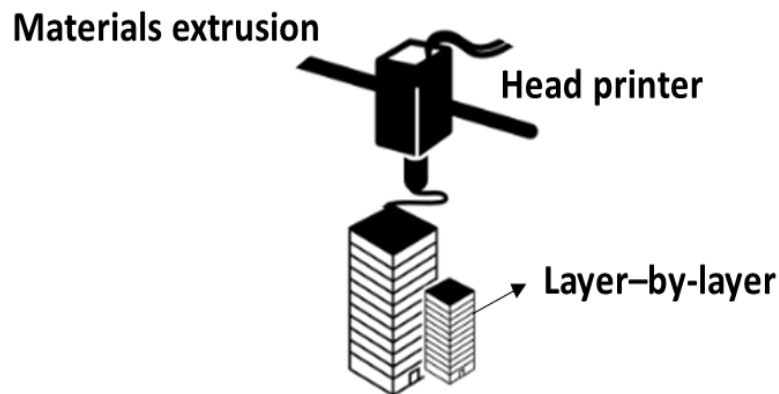


**Figure 2.25 Schematic of Materials extrusion process [75]**

### ***Binder jetting***

The Binder jetting technology is one of the main processes in additive manufacturing. This method works by creating metal powder across the work space by a powder roller. Then, the polymer binder is dropped from a print bar to the powder bed to produce the 3D object layer upon layer. The green body from this method needs to be sintered in an atmosphere furnace for near full density and strong mechanical properties [74]. This technology is used for printing the complex topology shape parts.

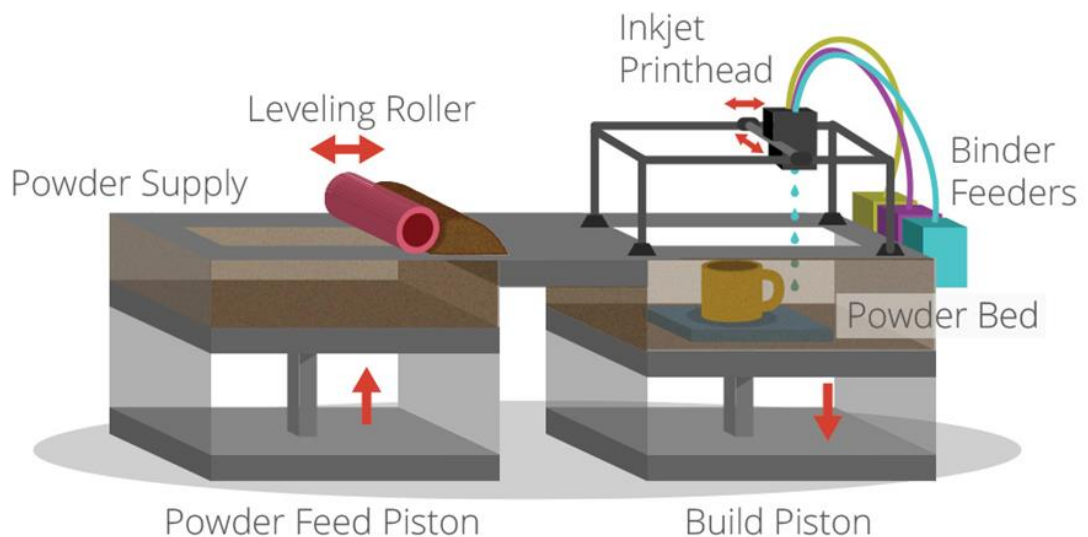


**Figure 2.26 Schematic of binder jetting process [76]**

### *Direct energy deposition*

The direct energy deposition technology (DED) is a material joining process by using the thermal energy heat source for melting the materials. DED is generally used for large parts with manufacturing high performance super alloys [75]. This method can combine easily with conventional processes to complete machining. The metallic materials commonly used in the DED process are Titanium, Inconel, Stainless steel, Aluminium and the related alloys for aerospace applications [74].

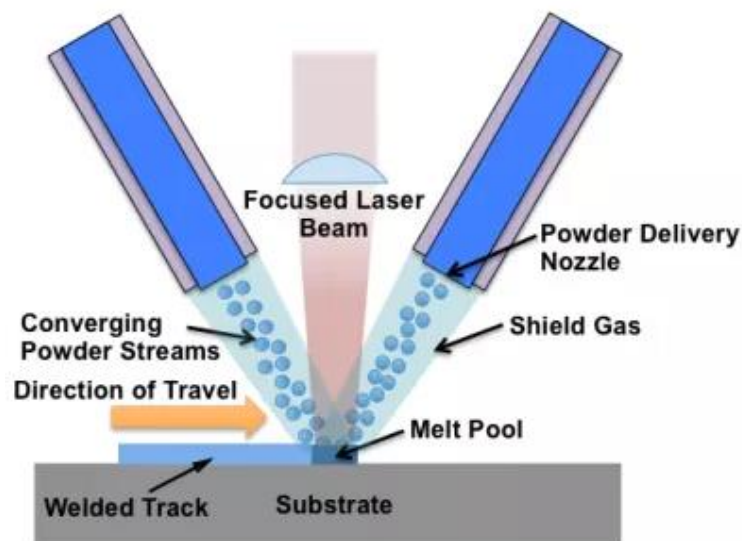


Figure 2.27 Schematic of Direct energy deposition [77]

---

## Chapter 3 Methodology

The work in this thesis was divided into two parts: the numerical study with experimental validation and the experimental study with material characterization. The numerical study was applied in the first part of the thesis in order to study the effect of process parameters on physical phenomena in L-PBF process of stainless steels with different grades including AISI 304, AISI 420 and AISI 316. In the second part of the study, the effect of laser process parameters on single track formation, layer formation, the microstructure and the microhardness of AISI 316L stainless steel fabricated by L-PBF process were investigated by the experimental study.

### 3.1. The numerical study with experimental validation

In first part of the study, the numerical study was used to study the physical phenomena including temperature distribution, melt pool geometry, single track formation and layer formation of the stainless steels by using the computer simulation method in L-PBF of the stainless steels. Three cases of the numerical studies on the stainless steels are described as follows:

#### 3.1.1 A numerical study on the thermal transient 2D Model with moving laser heat source of AISI 304 stainless steel plate

This numerical study aims to study the 2D thermal transient model of moving laser heat source with changeable direction of motion in order to investigate the effect of process parameters, e.g., power intensity, scanning speed and hatch spacing on the temperature distribution of the AISI 304 stainless steel plate.

##### a) Simulation model

Fourier heat conduction Equation is used to simulate a heat transfer process in the work piece. The governing Equation for heat conduction is described in Equation (2.4). Equations (2.5), (2.6) and (2.7) are the initial boundary conditions with

surface convection and radiation respectively. Figure 3.1 shows the conductivity coefficient and the specific heat capacity

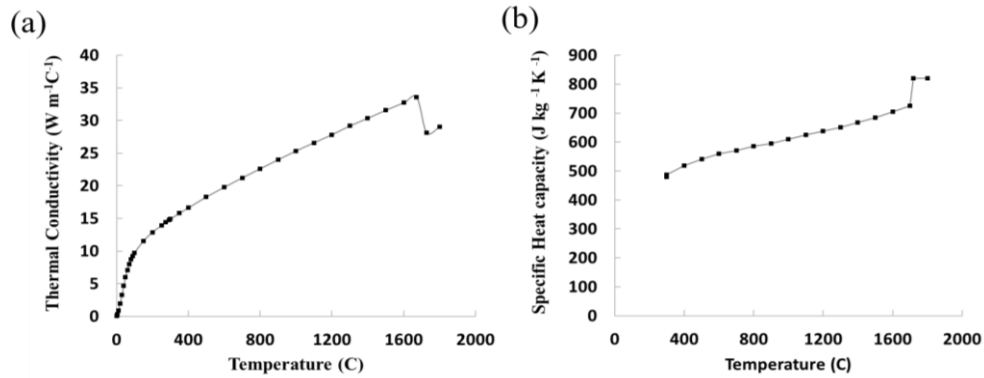


**Figure 3.1 Thermal properties of AISI 304; (a) The Thermal conductivity coefficient of AISI 304, (b) The specific heat capacity of AISI 304 [78]**

The Gaussian heat flux source model used in this study is described [79] as in Equation (3.1)

$$q = \frac{2P}{\pi\omega^2} e^{-\frac{[(x-x_0)^2+(y-y_0)^2+(z-z_0)^2]}{\omega^2}} \quad (3.1)$$

$q$  is heat flux on the surface,  $\omega$  is radius of beam,  $I_0$  is power intensity,  $(x_0, y_0, z_0)$  is instantaneous position of the center of the heat flux which is on the moving path at distance of  $x, y, z$  from start point,  $v$  is velocity of moving heat source,  $t$  is time.

The Gaussian heat energy source model is described [79] as in Equation (3.2)

$$E = I_0 e^{-\frac{[(x-x_0)^2+(y-y_0)^2+(z-z_0)^2]}{\omega^2}} \cdot e^{-AC(z-z_0)} \quad (3.2)$$

$E$  is heat energy,  $AC$  is absorption coefficient.

## b) computer simulation setup

This computer simulation was performed by commercial simulation software ANSYS 18.1. Figure 3.2 shows the user interface of ANSYS thermal transient program with uploaded CAD model, which was used to analyze the temperature distribution of the AISI 304 stainless steel plate. The geometry and moving path of laser heat source are shown in Figure 3.3 (a). A computational mesh of around 70,000 cells was used for the simulation. The mesh is shown in Figure 3.3 (b). The process parameters of moving laser heat source are listed in Table 3.1. The temperature history during the process is measured by the probes at six points as shown in Figure 3.3 (a). The distance between each point is 1 mm.

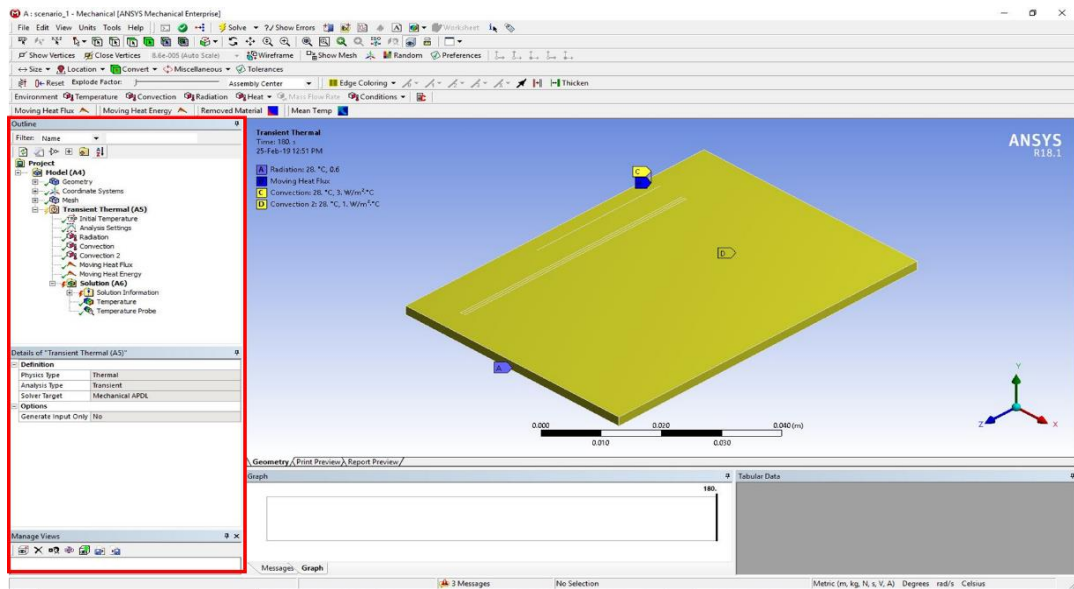


Figure 3.2 Setup simulation in ANSYS 18.1 program

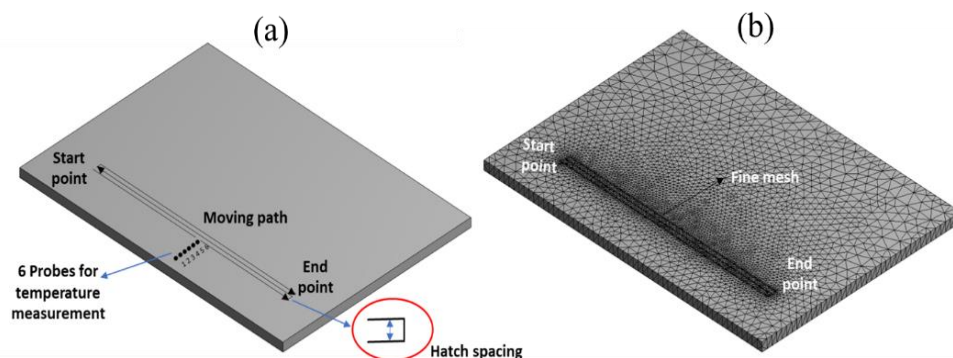


Figure 3.3 CAD model (a) The geometry and moving path of laser heat source, (b) mesh elements of the work piece model

**Table 3.1 Process parameters for the numerical simulation of moving laser heat source**

<b>Moving laser heat source parameter</b>	<b>Value (Unit)</b>
Power intensity ( $I_0$ )	200 – 480 W/mm <sup>2</sup>
Scanning speed ( $v$ )	0.68 and 1.32 mm/s
Hatch spacing ( $H$ )	0.5 and 1 mm
Absorption coefficient (AC)	0.30
Emissivity	0.6
Convection coefficient	3 (W/m <sup>2</sup> .°C)
Initial temperature ( $T_0$ )	27-28 °C
Time ( $t$ )	120, 180 sec

Five cases of numerical simulations with different parameters of moving laser heat source are shown in Table 3.2.

**Table 3.2 Five cases of numerical simulations with different parameters of moving laser heat source**

<b>Scenario</b>	<b>Power intensity (W/mm<sup>2</sup>)</b>	<b>Scanning speed (mm/s)</b>	<b>Hatch spacing (mm)</b>
1	200	1.32	0.5
2	200	1.32	1
3	200	0.68	0.5
4	200	0.68	1
5	480	0.68	0.5

### c) Experimental setup

The AISI 304 stainless steel plate with a dimension of  $50 \times 70 \times 2 \text{ mm}^3$  were used as specimens in this experiment. Figure 3.4 (a) shows the laser source device, JenLas® fiber ns 50, at Center Innovation of Design and Engineering for Manufacturing (Col-DEM), KMUTNB which has maximum power of 50 W. The laser focus position, the diameter of laser spot, and the power intensity used in this experiment are 18 cm, 0.35 mm, and  $200 \text{ W/mm}^2$  respectively. The specimen and experimental setup are shown in Figure 3.4 (b) The thermocouple probe is attached with the specimen at the same position as the probe point no.1 of the numerical model as shown in Figure 3.3 (a). The experiment tests are conducted in order to validate the results from numerical simulation. The parameters of the moving laser heat source used in the experiment were as same as those used in numerical simulations (see Table 3.1).

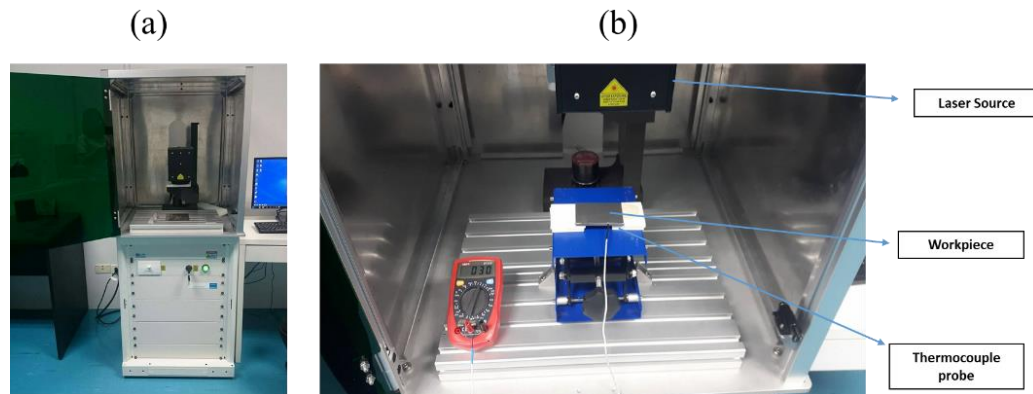


**Figure 3.4 The experiment setup (a) Laser source device at Center Innovation of Design and Engineering for Manufacturing (Col-DEM), KMUTNB, (b) Specimen and experimental setup**

### 3.1.2 Thermal and single track formation simulation in Laser powder bed fusion (L-PBF) process of AISI 420

The 3D powder bed model simulation was studied by CFD simulation software Flow-3D (Flow-weld) to investigate the effect of process parameters including Laser power and scanning speed on the temperature distribution and melt pool geometry during the L-PBF process. The results from this study were validated with the experimental results from the previous research study on Fabrication and Characterization of AISI 420 Stainless Steel Using Selective Laser Melting [30]

### a) Simulation model

Heat transfer simulation model in L-PBF process are consist of heat conduction, heat convection, heat radiation respectively [16]. Considering the melting and solidification phenomena, the enthalpy including latent heat evolution arising from phase change effect during the process can be applied in modelling [9]. The molten fluid flow simulation model of L-PBF process is based on numerical solution of mass, energy and momentum conservation as described in Equations (2.9), (2.10), (2.11) and the Volume of Fluid (VOF) method is used to track the position and shape of the molten pool surface as shown in Equation (2.12) [9]. The molten fluid flow is assumed to be incompressible and Newtonian with laminar flow. The Gaussian laser moving heat source model is described in Equation (3.1).

### b) Computer simulation setup

The 3D model simulation was performed by commercial CFD simulation software Flow-3D (Flow-weld). The material used in this study was AISI 420 stainless steel with the average particle size of 20  $\mu\text{m}$ . The 3D computational mesh of around 375,000 cells were used in this simulation. Figure 3.5 presents the user interface of the simulation setup in the Flow-3D program with CAD model. Figure 3.6 shows the schematic of the powder bed and scanning direction of moving laser beam. The materials properties of AISI 420 stainless steel from Flow-3D database and process parameters used in this study are listed in Table 3.3.

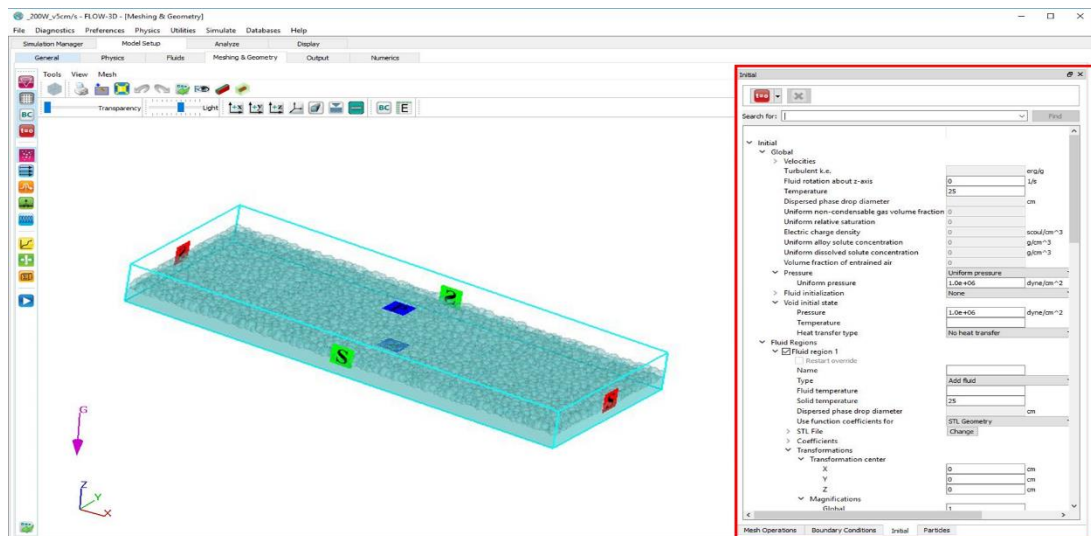


**Figure 3.5 The simulation setup in the Flow-3D program**



**Figure 3.6 The schematic of the powder bed and scanning direction of moving laser beam**

The thermal-physical properties of AISI 420 martensitic stainless steel including density, thermal conductivity, specific heat are plotted in Figure 3.7.

[80]

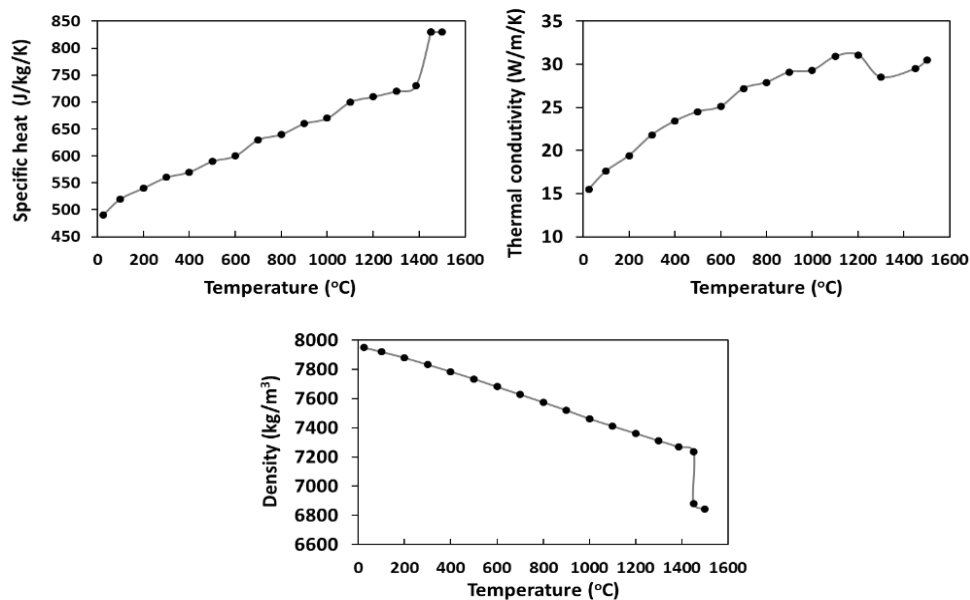


**Figure 3.7 Thermal-physical properties of AISI 420 stainless steel including density, thermal conductivity, specific heat [80]**

**Table 3.3 Materials properties of AISI 420 stainless steel and Process parameters used in this simulation study**

Materials properties and process parameters	Value (unit)
Liquidus	1510 (°C)
Solidus	1454 (°C)
Latent heat of fusion	$3.04 \times 10^9$ (J/kg)

Viscosity	0.05 (kg/m/s)
Surface tension	1.8 (kg/s <sup>2</sup> )
Laser power	120, 140 (Watt)
Scanning speed	0.4, 0.6, 0.8 (m/s)
Layer thickness	50 (μm)
Laser beam spot size	80 (μm)

Six cases of the numerical simulations with varied process parameters are shown in Table 3.4 below.

**Table 3.4 Case study of the numerical simulation with different process parameters**

Cases	Laser power (Watt)	Scanning speed (m/sec)	Layer thickness (μm)	Laser spot size (μm)
1	120	0.4	50	80
2	120	0.6	50	80
3	120	0.8	50	80
4	140	0.4	50	80
5	140	0.6	50	80
6	140	0.8	50	80

### **3.1.3 Numerical study and experimental validation on single track formation and layer formation of AISI 316L stainless steel fabricated by L-PBF process**

The effect of process parameters including laser power, scanning speed and hatch spacing on single track formation and layer formation of AISI 316L stainless steel fabricated by L-PBF process was investigated by CFD simulation software Flow-

3D / Flow-weld. The results from the simulation of this study were validated with the experimental results.

a) Simulation model

The same Equations as used in the simulation model in 3.1.2 were applied with different material properties to investigate single track formation and layer formation of AISI 316L stainless steel.

b) Computer simulation setup

The numerical simulation setup started with preparing the metal powder bed CAD model by using Flow-DEM software in order to obtain the STL file. After that the STL file of metal powder bed was uploaded to the CFD simulation software (Flow-weld) to obtain the single track formation and layer formation of the AISI 316L stainless steel fabricated by L-PBF process. The AISI 316L stainless steel with the particle size between  $20\ \mu\text{m}$  and  $53\ \mu\text{m}$  were used in the study. The schematic of simulation domain for single track formation is shown in Figure 3.8. The computation domain with laser moving path is shown in Figure 3.9. The hatch spacing was determined by using overlap ratio to create the layer formation. The overlap ratio is described as in Equation 3.3 [81]. The hatch spacing of  $90\ \mu\text{m}$  and  $135\ \mu\text{m}$  were used in the study as shown in case studies 9 and 10 (See in Table 3.6). The materials properties from Flow-3D database and process parameters used in this study are shown in Table 3.5.

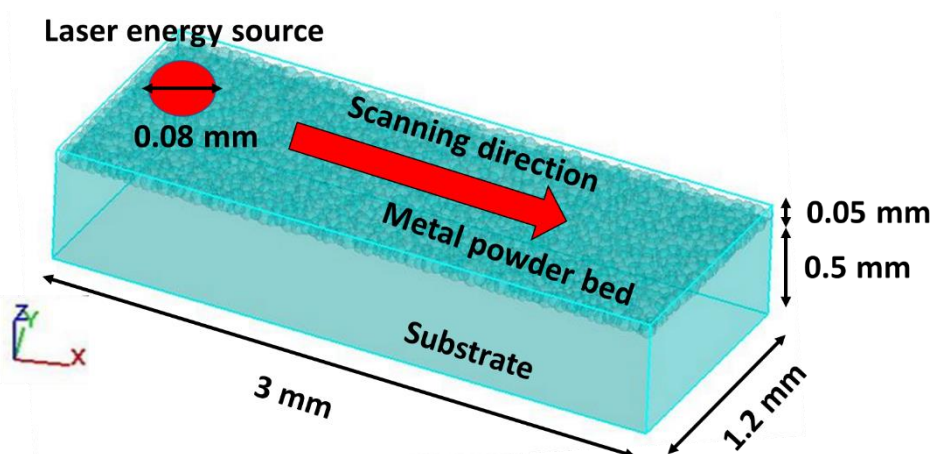


**Figure 3.8** The schematic of simulation domain for single track formation

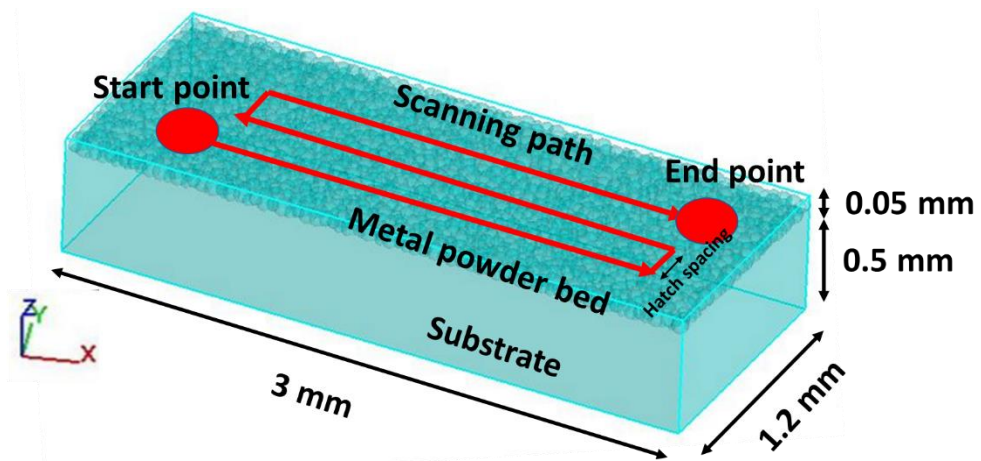


**Figure 3.9** The schematic of simulation domain for layer formation

$$\text{Overlap ratio (\%)} = ((1 - H) / W) \times 100 \quad (3.3)$$

H is hatch spacing ( $\mu\text{m}$ ), W is melted track width ( $\mu\text{m}$ )

**Table 3.5** Materials properties of AISI 316L stainless steel and Process parameters used in this simulation study

Materials properties and process parameters	Value (unit)
Liquidus	1424 ( $^{\circ}\text{C}$ )
Solidus	1401 ( $^{\circ}\text{C}$ )
Latent heat of fusion	$2.6 \times 10^9$ (J/kg)
Viscosity	0.08 (kg/m/s)
Surface tension	1.8 ( $\text{kg/s}^2$ )
Laser power	125, 150, 175, 200 (Watt)
Scanning speed	50, 75, 100, 125, 150 (mm/s)
Hatch spacing	Overlap 25 %, 50 % of melted track width
Layer thickness	50 ( $\mu\text{m}$ )
Laser beam spot size	80 ( $\mu\text{m}$ )

The thermal-physical properties of AISI 316L stainless steel including density, thermal conductivity, specific heat are shown in Figure 3.10 [80].

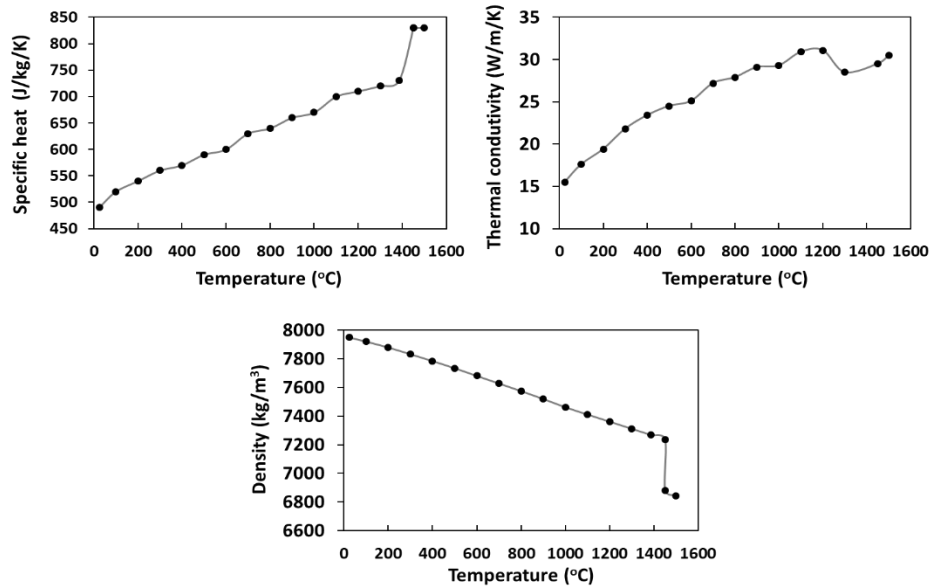


**Figure 3.10 Thermal-physical properties of AISI 316L stainless steel including density, thermal conductivity, specific heat [80]**

Ten cases of numerical and experimental studies with different process parameters are shown in Table 3.6.

**Table 3.6 The case study of numerical simulation with different process parameters**

Case	Laser power (Watt)	Scanning speed (mm/sec)	Layer thickness ( $\mu\text{m}$ )	Laser spot size ( $\mu\text{m}$ )	Hatch spacing ( $\mu\text{m}$ )	Condition
1	200	50	50	80	-	Single line
2	200	75	50	80	-	Single line
3	200	100	50	80	-	Single line
4	200	125	50	80	-	Single line
5	200	150	50	80	-	Single line

6	125	100	50	80	-	Single line
7	150	100	50	80	-	Single line
8	175	100	50	80	-	Single line
9	200	100	50	80	135	25 % of melted track width
10	200	100	50	80	90	50 % of melted track width

### c) Experimental setup

The AISI 316L stainless steel powder with particle size between 20  $\mu\text{m}$  and 53  $\mu\text{m}$  were used in this experiment. The mild steel plate SS400 with the dimensions of 8 cm x 8 cm x 0.8 cm was used for material substrate. The laser energy source device, YLR-300AC at ImplanTable Medical Device Technology Research Team lab, Assistive Technology and Medical Devices Research Center, National Science and Technology Development Agency, NSTDA which has maximum power 300 W was used as energy heat source in this work. Figure 3.11 shows the experimental setup. The results from experiment tests are validated with the results from numerical simulation. The process parameters used in the experiment was the same as that in the numerical simulations case studies (See Table 3.6).



**Figure 3.11** The experimental setup

## 3.2. The experimental study with material characterization

### 3.2.1 Materials

The materials used in the experiment was AISI 316L stainless steel spherical-shaped powder which is particularly used in additive manufacturing process [82] from Hoganas Belgium S.A factory with the metal powder size of 20-53  $\mu\text{m}$ . The chemical compositions of AISI 316L stainless steel are shown in Table 3.7.

**Table 3.7 The chemical compositions of stainless steels including AISI 304 and AISI 316L [82]**

Types	Chemical compositions (%wt.)								
	C	Mn	Si	P	S	Cr	Mo	Ni	N
AISI 316L	0.03	2	1	0.045	0.015	18.5	3	14	0.03

### 3.2.2 Experimental process

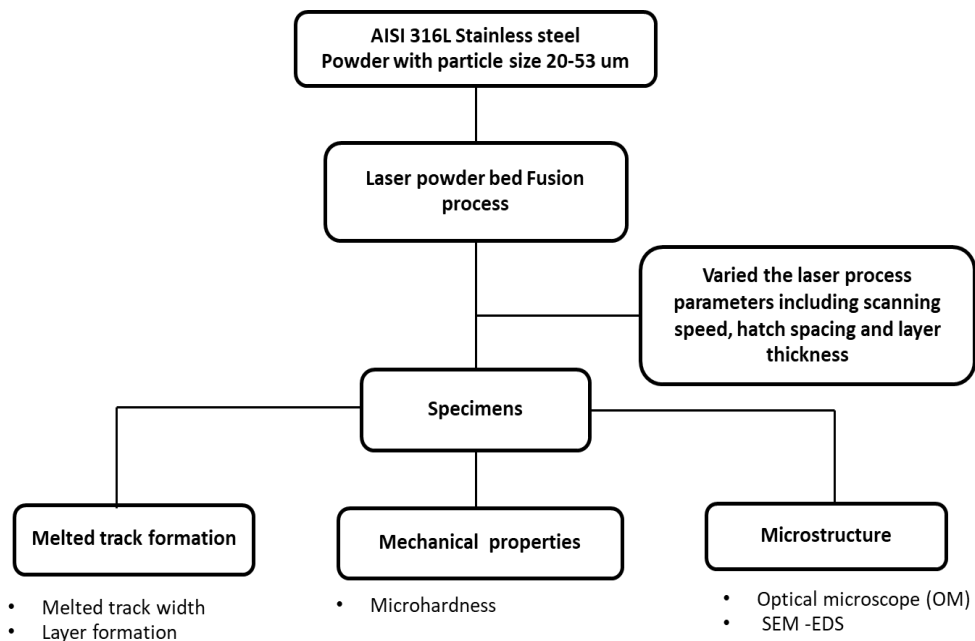


**Figure 3.12 The experimental process in the second part**

The effect of laser process parameters on single track formation, layer formation, the microstructure and the microhardness of AISI 316L stainless steel fabricated by L-PBF process were investigated by the experimental study. The experimental process in the second part of the thesis are illustrated in Figure 3.12. The experimental process is described as follows:

### 1. Creating the building platform and gas chamber

The building platform and gas chamber in the L-PBF system were designed and built to create the specimens to investigate the single track formation, layer formation microstructure and microhardness of AISI 316L stainless steel fabricated by L-PBF process as shown in Figure 3.13.

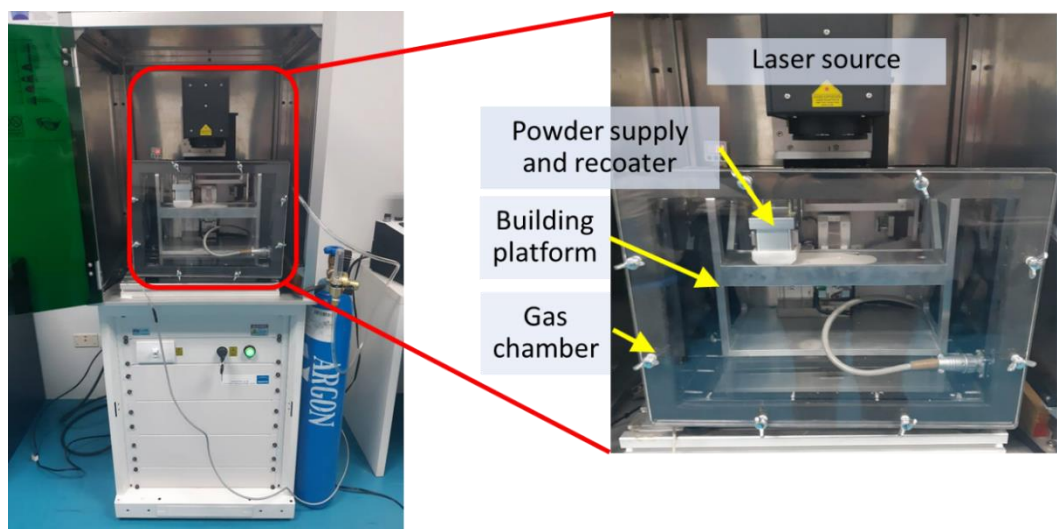


**Figure 3.13** The building platform and gas chamber

### 2. Creating specimens

The process of creating specimens started with defining the layer thickness of the specimens. After that the metal powder was raked by the recoater on the work space to create metal powder bed. Then, the laser energy source 50 watt with continuous wave (CW) mode was used as heat energy to melt the metal powder bed layer by layer. Figure 3.14 (a) shows the laser heat source interacting with metal powder bed in L-PBF process. An example of the layer formation is shown in Figure 3.14 (b).

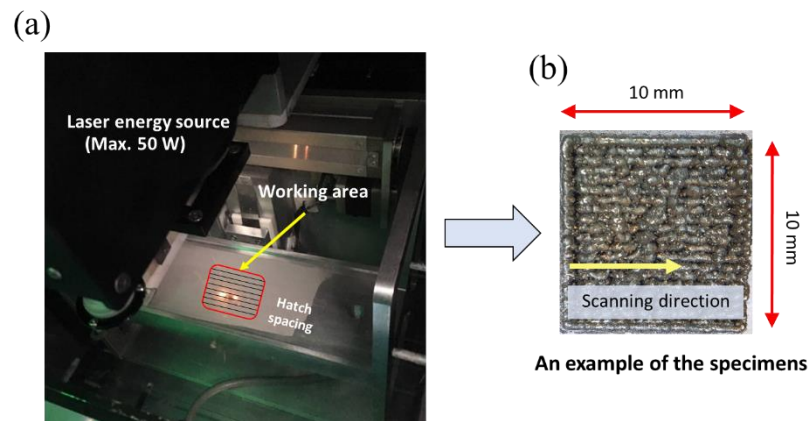


**Figure 3.14 Creating specimens (a) The laser heat source interacting with metal powder bed in L-PBF process, (b) An example of the specimens**

### 3. Melted track width and layer formation analysis

The laser melted track width and layer formation were analyzed by the Stereomicroscope and macro camera as shown in Figure 3.15 (a), (b).



**Figure 3.15 The analysis equipment (a) Stereomicroscope, (b) macro camera**

### 4. Microstructure analysis

The microstructure of the AISI 316L stainless steel was characterized by the optical microscope and the scanning electron microscope (SEM). The microstructure analysis process is described as follows:

a) Cutting the specimens

First, select the interested position of specimens, then cut the specimens into four sections by the cutting machine as shows in Figure 3.16 (a). The cut specimen are shown in Figure 3.16 (b).



**Figure 3.16 The process of cutting the specimens, (a) cutting machine, (b) The cut specimens**

b) Hot mount process

After cutting the specimens into four sections, they were mounted by the hot mount process as shown in Figure 3.17 (a), (b).

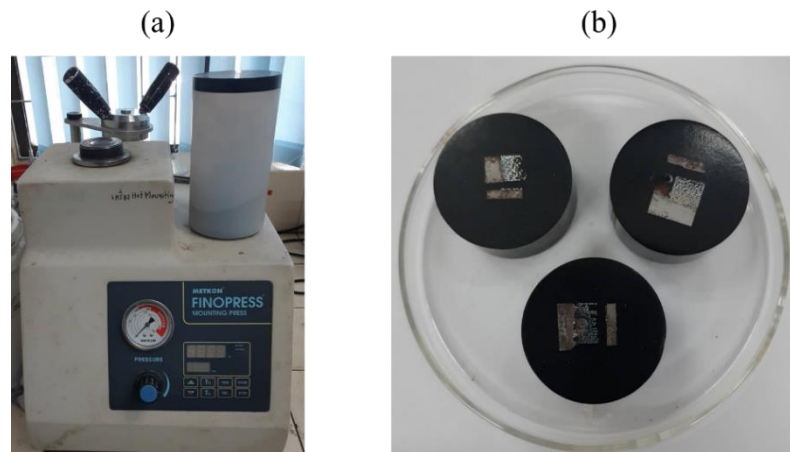


**Figure 3.17 The hot mounting process (a) Hot mounting machine, (b) The section of specimens inside hot mount resin**

c) Grinding process

The hot mounted specimens were grinned with sand paper from coarse grit to fine grit (500 to 2000) step by step to make the surface smooth and flat as shown in Figure 3.18.



**Figure 3.18 Grinding process**

d) Polishing process

After the grinding process, the hot mounted specimens were polished on the polishing paper with the alumina alpha suspension 0.3 and 0.1 micron to make the polishing surface as shown in Figure 3.19.



**Figure 3.19 Polishing process**

e) Surface etching process

To analyze the microstructure, the hot mounted specimens were etched by acid. The acids used in this process were mixed by nitric acid ( $\text{HNO}_3$ ),

glycerol ( $C_3H_8O_3$ ) and hydrochloric acid (HCl) with a ratio of 1:2:3. as shown in Figure 3.20.



**Figure 3.20** The acids used in etching process

f) Taking pictures of the microstructure of AISI 316L stainless steel

The microstructure of AISI 316L stainless steel fabricated by L-PBF process was investigated by optical microscope at 20x and 50x magnification as shown in Figure 3.21.

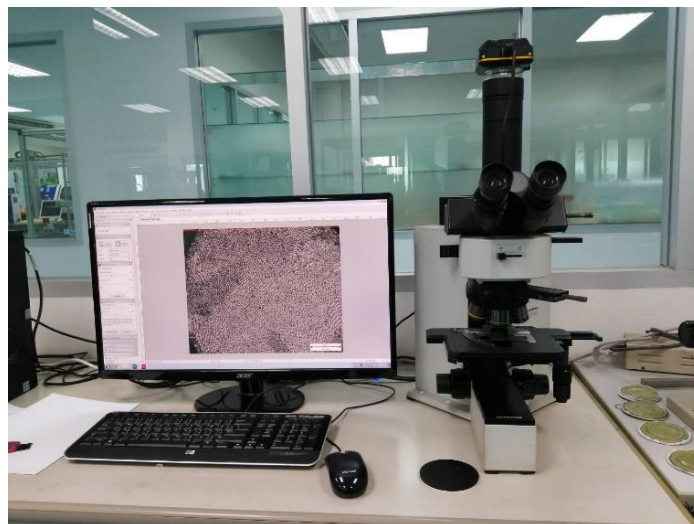


**Figure 3.21** The process of microstructure analysis

## 5. Characterizing the microstructure

The microstructure of AISI 316L was analyzed at 5,000x, 10,000x and 20,000x magnification, focusing on the microstructure of the material at the surface of the specimen by the Scanning Electron Microscope (SEM) as shown in Figure 3.22. The SEM with energy dispersive spectroscopy technique (SEM/EDS) technique was used to characterize the structure of the material and to investigate the amount of chemical composition of specimens.



**Figure 3.22 Scanning electron microscopy**

## 6. Testing the microhardness

The hardness properties of AISI 316L stainless steel fabricated by L-PBF process were carried out by measuring the Vickers hardness along the cross-section area of the specimens as shown in Figure 3.23. The investigation began with putting the specimen on the testing Table, then selecting the interested areas of the specimens. The structure of the specimens was pressed by the indenter to investigate the hardness property of the specimens. The applied test load used in the test was 100-gram force (gf).



**Figure 3.23 Testing the hardness properties**

The details of process parameters for case studies in the experiment are shown in Table 3.8. The laser power, scanning speed, layer thickness and hatch spacing used in the experiment are 50 watt, 5 mm/s, 10 mm/s, 15 mm/s, 50-300  $\mu\text{m}$  respectively.

**Table 3.8 The six cases experiment study of single single track formation with different the scanning speed**

<b>Cases</b>	<b>Material</b>	<b>Laser Power (Watt)</b>	<b>Scanning speed (mm/s)</b>	<b>Hatch spacing (mm)</b>	<b>Layer thickness (<math>\mu\text{m}</math>)</b>	<b>Atmosphere</b>
1	AISI 316L	50	5	0.3	50	Argon
2	AISI 316L	50	10	0.3	50	Argon
3	AISI 316L	50	15	0.3	50	Argon
4	AISI 316L	50	5	0.1	300	Argon
5	AISI 316L	50	5	0.3	300	Argon
6	AISI 316L	50	5	0.5	300	Argon

## Chapter 4 Results and Discussion

### 4.1. Computer simulation results

#### 4.1.1 The numerical simulation results of the thermal transient 2D Model with moving laser heat source of AISI 304 stainless steel plate

##### a) Temperature distribution

Temperature distribution in the numerical specimen model from the scenario 1 at time 30 sec, 70 sec and 101 sec are shown in Figure 4.1. The contour shape of temperature distribution is influenced by the history and direction of moving laser heat source. At 30 sec (a), the temperature contour has a comet-shape with the tail opposite to the laser moving direction. The tail deviates toward the lower side since the upper zone has more volume for heat conductive transfer. The maximum temperature in the specimen model is 1361°C in the region under direct irradiation. At 70 sec (b) and 101 sec (c), the comet-shape area of temperature distribution are expand due to the heat accumulation during the back and forth moving of laser heat source on the specimen.

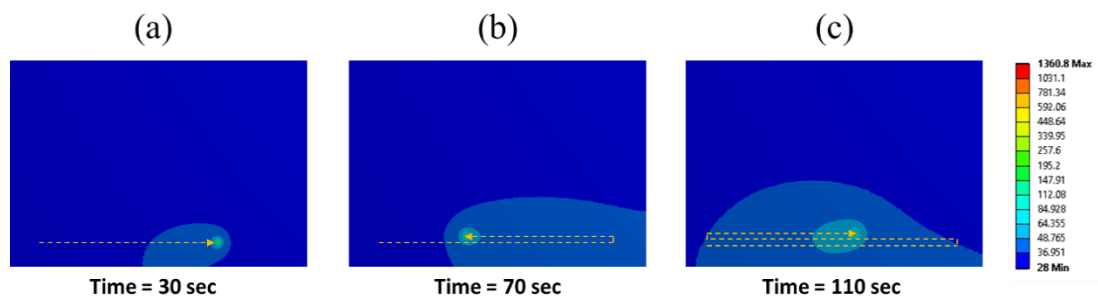


**Figure 4.1** Temperature distribution in the numerical specimen model from the scenario 1 at time (a) 30 sec, (b) 70 sec and (c) 101 sec.

b) Effect of scanning speed and hatch spacing

The numerical simulation results from test scenario 1 and 2 were validated with the experimental results as shown in Figure 4.2. The graphs show the temperature history at the probe point no.1 (see in Figure 4.3). The temperature peak took place after the moving of heat source passed that area. The temperature profile of scenario 1 (hatch spacing 0.5 mm) is slightly higher than that of scenario 2 (hatch spacing 1 mm), e.g., the second peak of scenario 1 and 2 are 184 °C and 176 °C respectively. The comparison of the results from numerical simulations and experiments shows good agreement with minor difference. The peak of the results from experiment are slightly lower than that of the simulation. Figure 4.3 shows the effect of moving laser heat source parameters, e.g., scanning speed and hatch spacing, on the temperature history at the probe point no.1 from the 4 scenarios of numerical simulation. When the scanning speed is decreased from 1.32 mm/s to 0.68 mm/s, the first temperature peak of the graph is increased from 128 °C to 194 °C. Different hatch spacing slightly affects the temperature history at probe point no.1 as can be seen from Figure 4.3. At the second temperature peaks in the graph, with the increasing of hatch spacing from 0.5 mm to 1.0 mm, the temperature peak is decreased for around 5-10 °C.

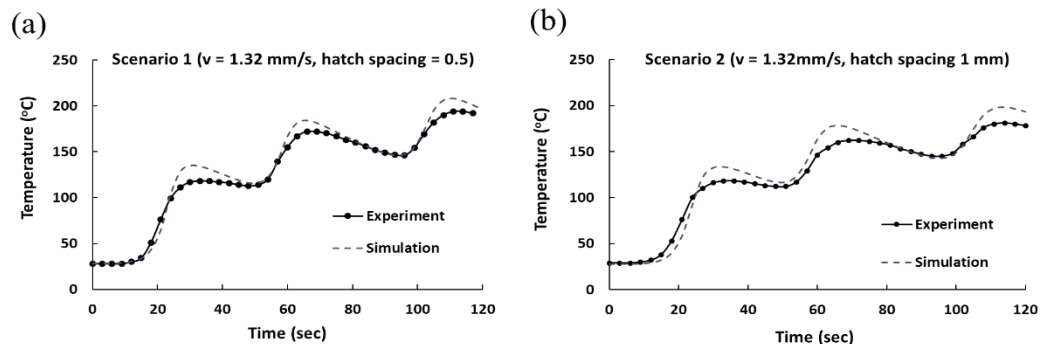


**Figure 4.2 Temperature History at The Probe Point No.1 of Specimen in (a) Scenario 1 and (b) Scenario 2**

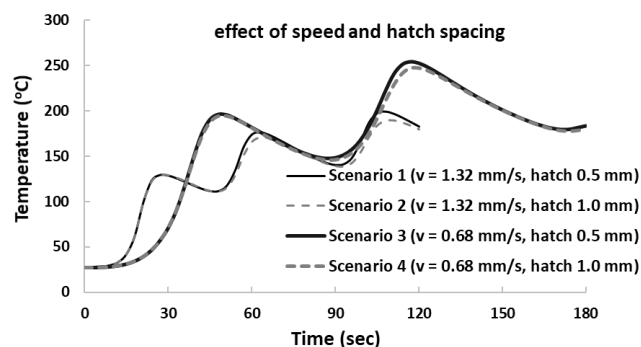


**Figure 4.3 Comparison of Temperature History at The Probe Point No.1 From the 4 Scenarios of Numerical Simulation**

c) Temperature history at six probe points

Figure 4.4 shows the temperature histories at six probe points from the numerical simulations of scenario 3 and 5 which have power intensity of 200 W/mm<sup>2</sup> and 480 W/mm<sup>2</sup> respectively. At the probe point no.6 which is the position at the first forth path of laser beam, the first peak temperature was increased from around 1200 °C to 2500 °C after the power intensity was increased from 200 W/mm<sup>2</sup> to 480 W/mm<sup>2</sup>. At the probe point no.1 to no.5, the temperature of both peaks are not so much different, while at the probe point no.6, the second temperature peak is much lower than the first peak.

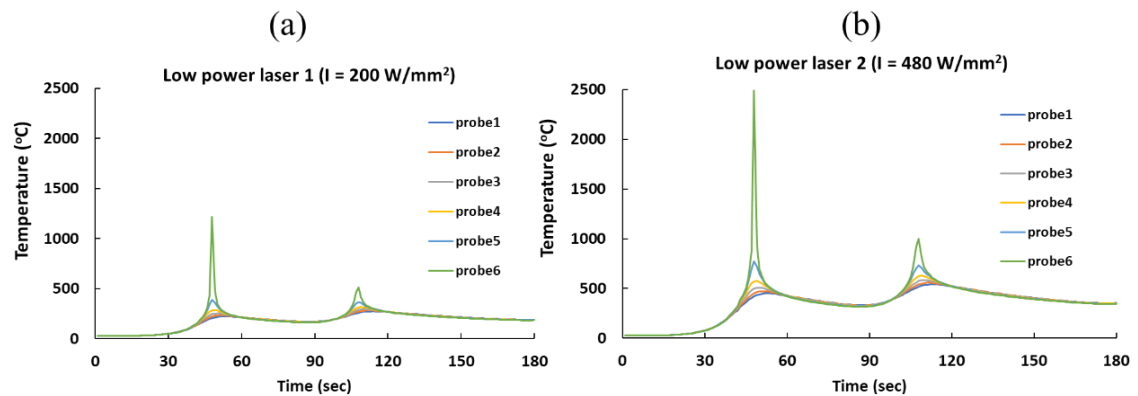


**Figure 4.4 The Temperature History Profile at Six Probe Points of (a) Scenario 3 and (b) Scenario 5**

#### 4.1.2 The computer simulation results of temperature distribution and single track formation of AISI 420 martensitic stainless steel during Laser powder bed fusion (L-PBF) process

a) The effects of process parameters on temperature distribution and melt pool shape

At the higher laser power and lower scanning speed, the temperature field has a larger region of heat distribution than that of lower laser power and high scanning speed as shown in Figure 4.5 and Figure 4.6. The temperature distribution is expanded due to the heat accumulation of metal powder bed. This phenomena have a significant effect to the quality of final parts such as thermal stress, distortion and crack. Figure 4.7 shows the effect of scanning speed on melt pool geometry, the geometry of melt pools can be changed from ellipse shape to tear drop shape when the scanning

speed is increased. Melt pool geometry can be controlled the density, porosity and surface roughness of final products.

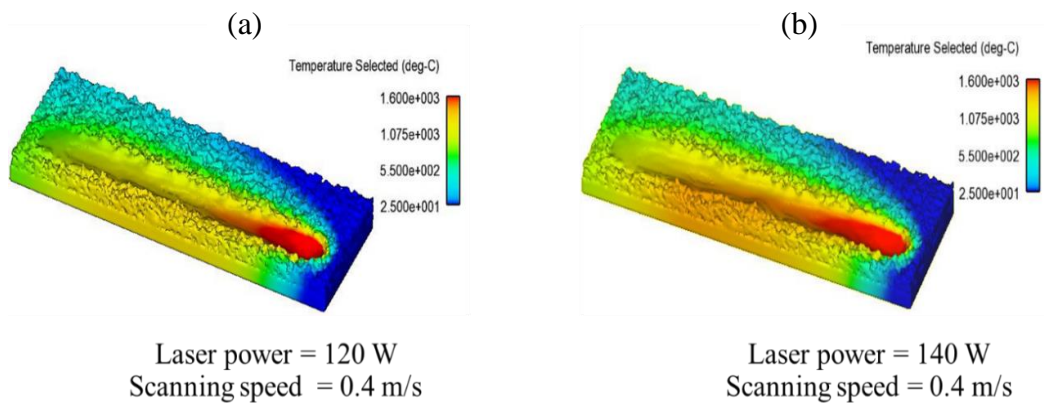


**Figure 4.5 The effect of laser power on temperature field during L-PBF process**

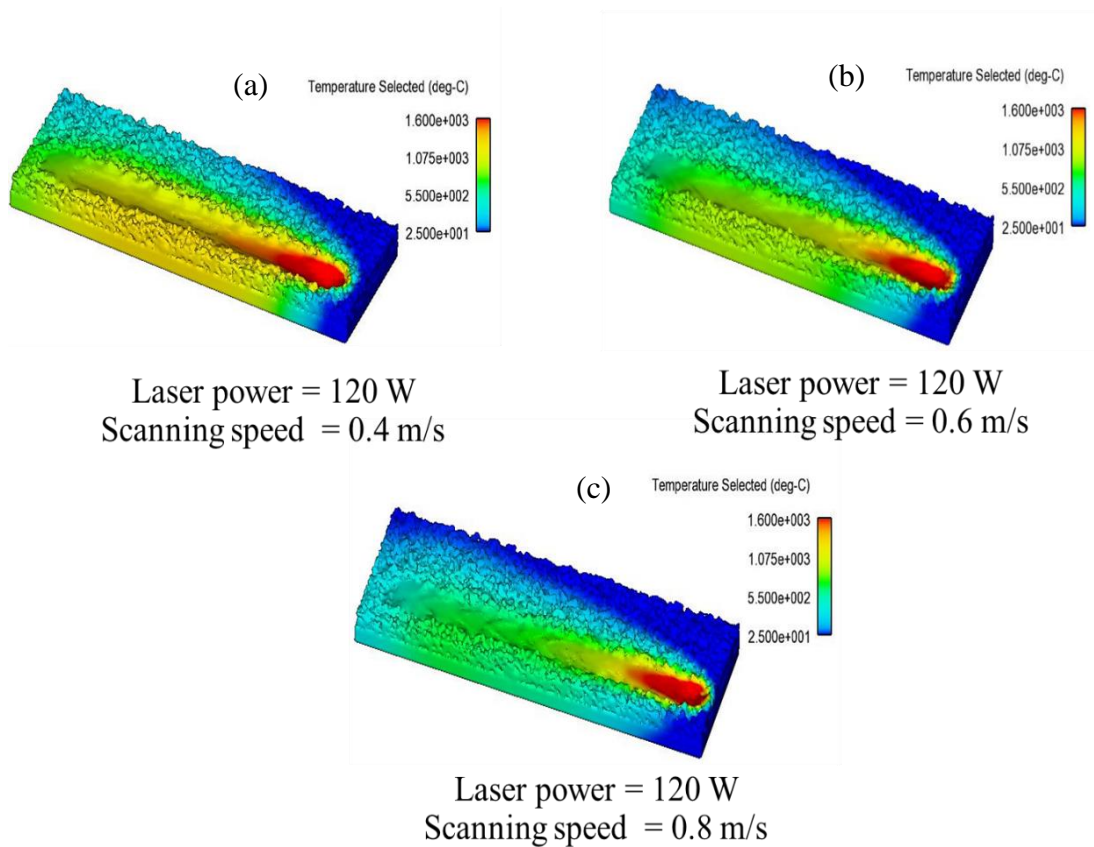


**Figure 4.6 The effect of scanning speed on temperature field during L-PBF process**

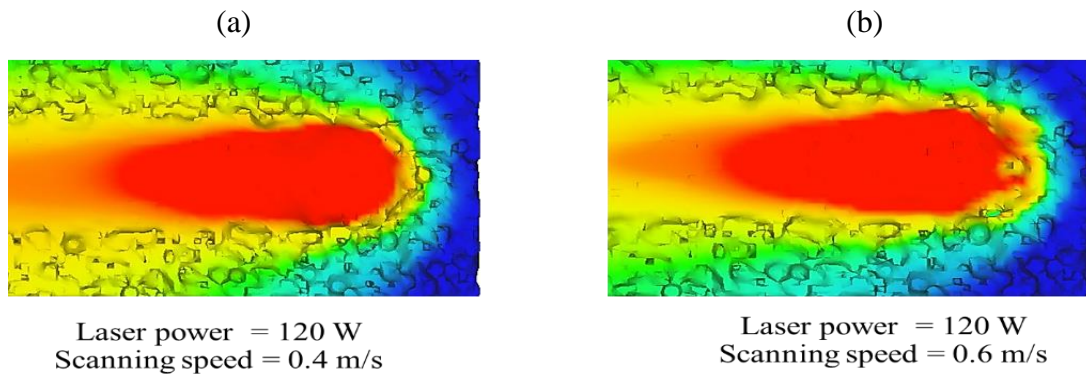


**Figure 4.7 The effect of scanning speed on melt pool geometry**

b) Fluid flow in molten metal pool

Figure 4.8 shows the longitudinal section view of molten metal pool, which is parallel to the laser scanning direction. The temperature distribution and velocity flow field are plotted as the color contours and the arrows. The molten metal pool boundary is presented in red color at 1600 °C, which is the melting temperature of steels. The surface tension at the center of melt pool is lower than the back region of molten metal pool, thereby leading to the backward flow of the molten metal near the surface. The surface tension will induce the Marangoni flow from lower surface tension region to higher surface tension region.

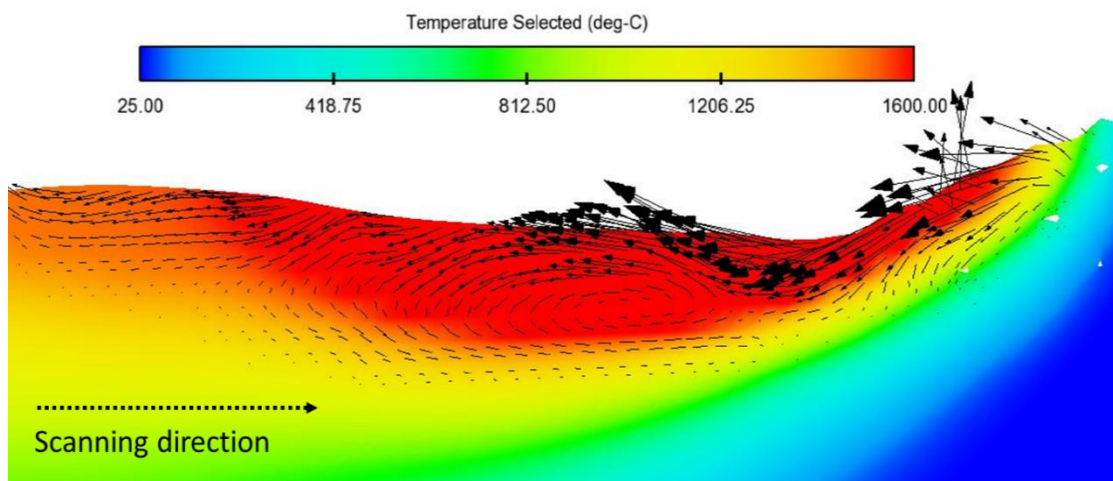


**Figure 4.8 Longitudinal section view of molten metal pool and fluid flow in molten metal pool**

c) The width and depth of single melted track with different process parameters

Figure 4.9 – 4.12 present the effects of process parameters including laser power and scanning speed on single track formation width. The width and depth of single melted track formation are increased when the higher laser power and lower scanning speed are applied. The results from the simulation are consistent with the experimental results as shown in Figure 4.13 (a).

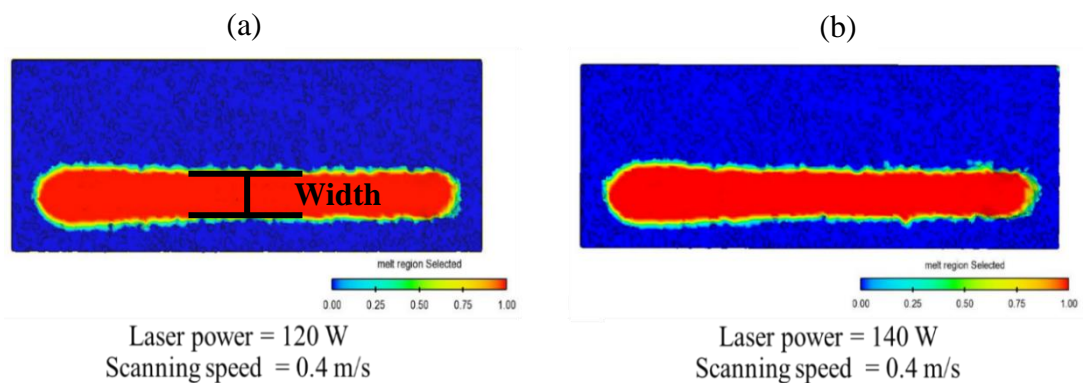


**Figure 4.9 The effect of laser power on the width of single track formation**

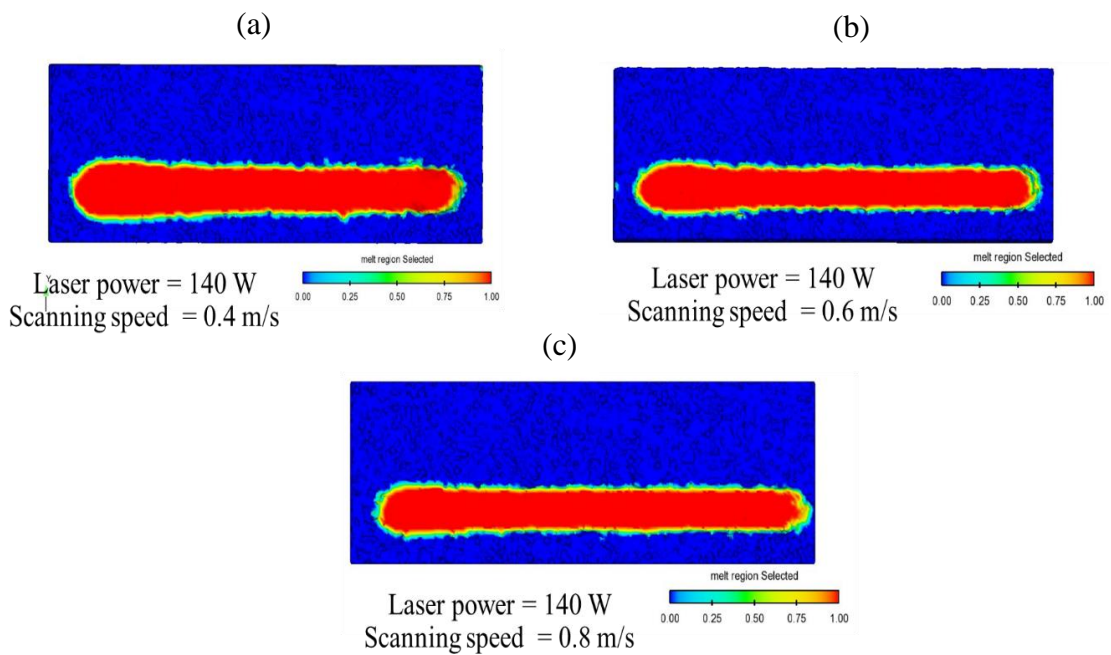


**Figure 4.10 The effect of scanning speed on the width of single track formation**

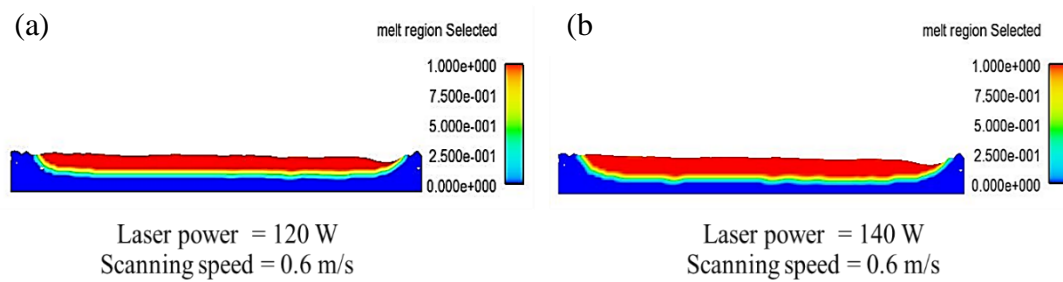


**Figure 4.11 The effect of laser power on single track formation depth**

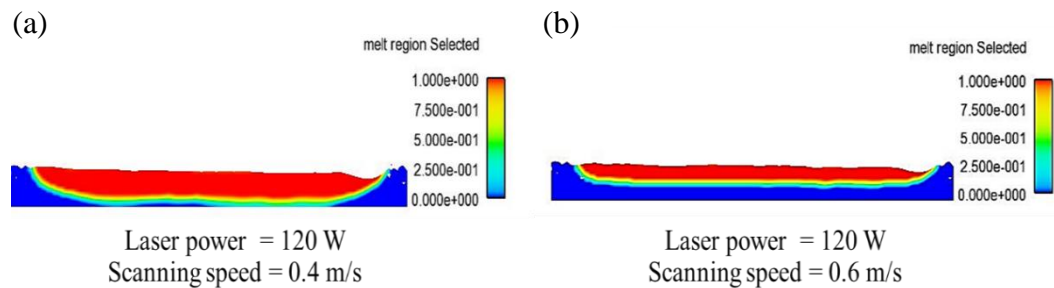


**Figure 4.12 The effect of scanning speed on single track formation depth**

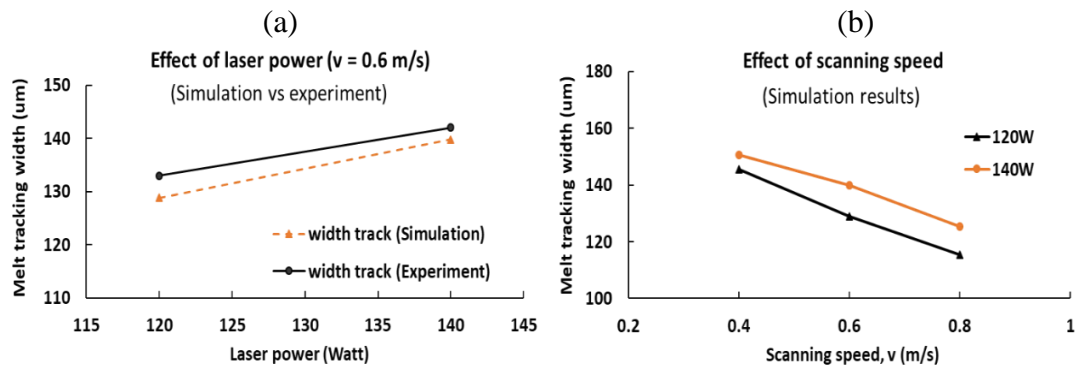


**Figure 4.13 The simulation results validated with experimental results (a), The effect of process parameter on the width of single track formation**

### 4.1.3 The results of the numerical study and experimental validation on single track formation and layer formation of AISI 316L stainless steel fabricated by L-PBF process

In this section, the effect of laser process parameters on single track formation and layer formation of AISI 316L stainless steel fabricated by L-PBF process are discussed. Figure 4.14 shows the measurement of width and depth of melted track obtained by computer simulation. The red color contour shows the melt region and the

blue color presents solid or unmelt region. Figure 4.15 shows an example of average melted track width from experiment using stereomicroscope.

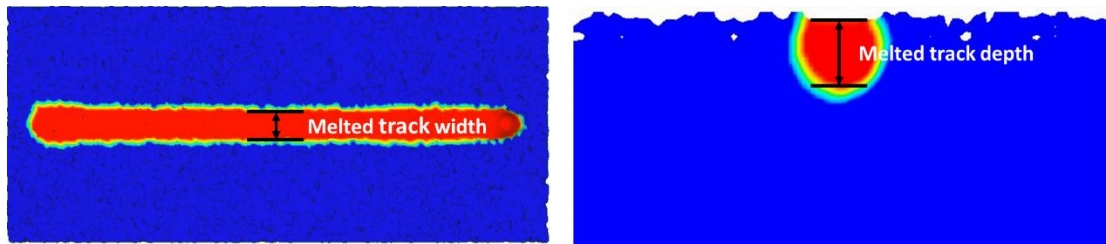


**Figure 4.14** The measurement of width and depth of melted track obtained by computer simulation

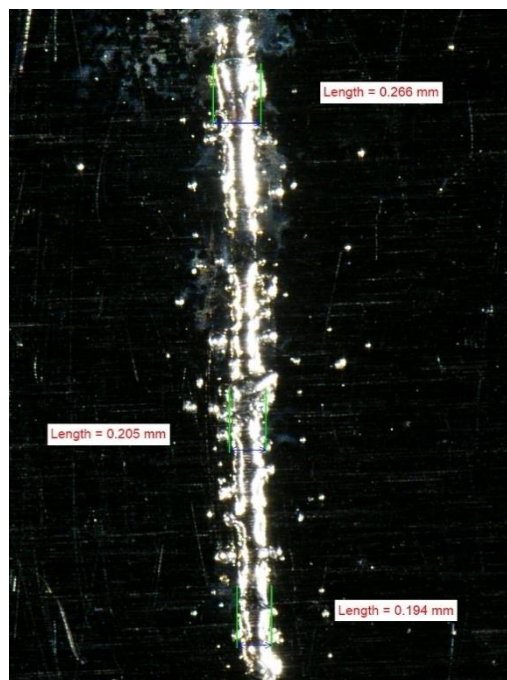


**Figure 4.15** An example measurement the melted track obtained by experiment

a) The effect of scanning speed on melted track width

In the Figure 4.16, the blue triangle and black circle show the width of the simulated and experimental melted tracks with different scanning speed. The results from both the simulation and the experiment present the laser melted track width are narrowed gradually when the scanning speed is increased. The melted track width varies between 139 and 214  $\mu\text{m}$ . The melted track width measured from the experimental study was 10-20  $\mu\text{m}$  wider than that of the simulation. The results from the simulation is in agreement with the experimental results.

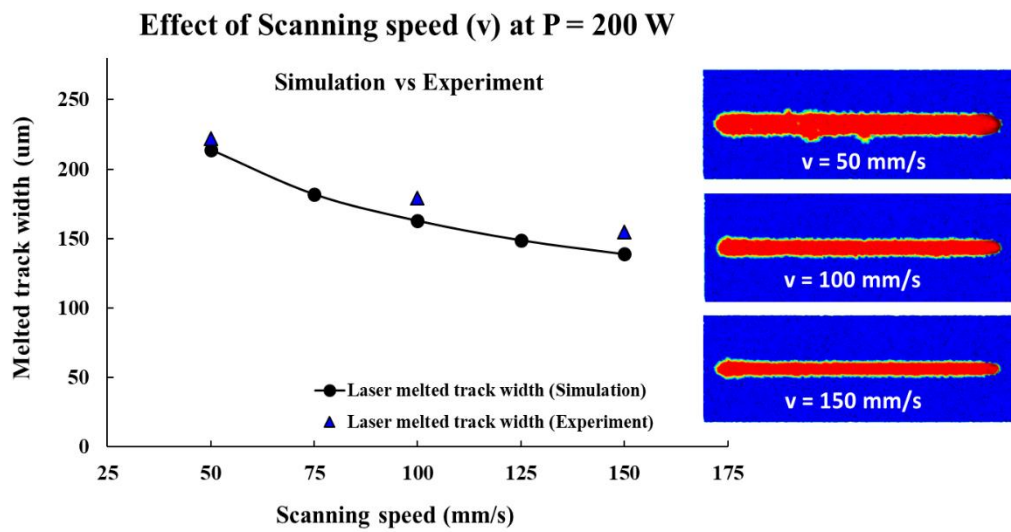


**Figure 4.16** The melted track width with different scanning speed

b) The effect laser power on melted track width

The effect of laser power on melted track width are shown in Figure 4.17. The results from the simulation and the experimental study show the laser melted track width is increased when the higher laser power is applied. The melted track width varies between 133 and 179  $\mu\text{m}$ . Accordingly, the results from the simulation are in agreement with the experimental results.

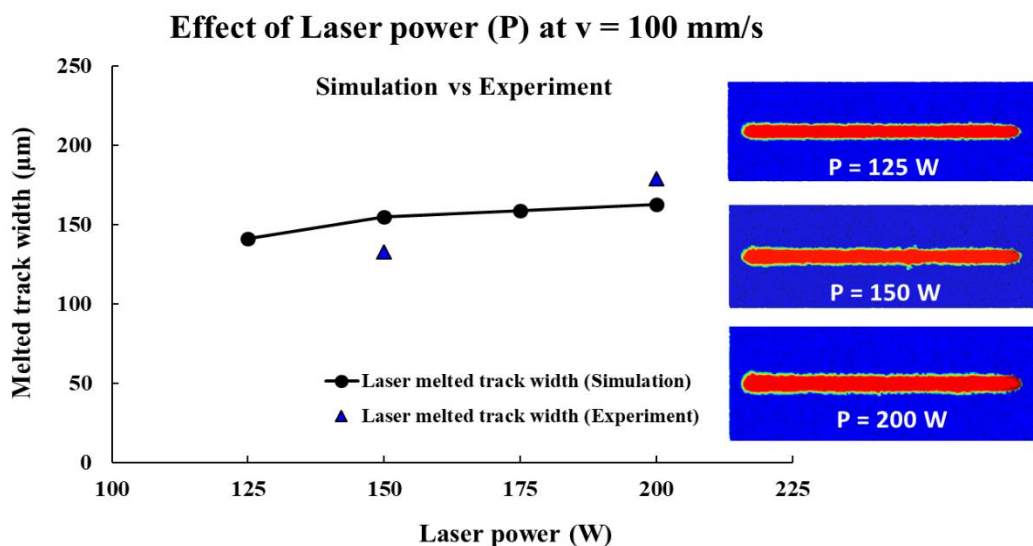


**Figure 4.17** The melted track width with different laser power

- c) The effect of scanning speed and laser power on the depth of melted track

Figure 4.18 and 4.19 show the simulation results of melted track depth with different scanning speed and laser power. In the Figure, the black squares illustrate the results of the melted track depth with different scanning speed and laser power. The results show that the depth of melted track is decreased when the higher scanning speed and lower laser power are applied. The depth of melted track varied from 110  $\mu\text{m}$  to 240  $\mu\text{m}$ .

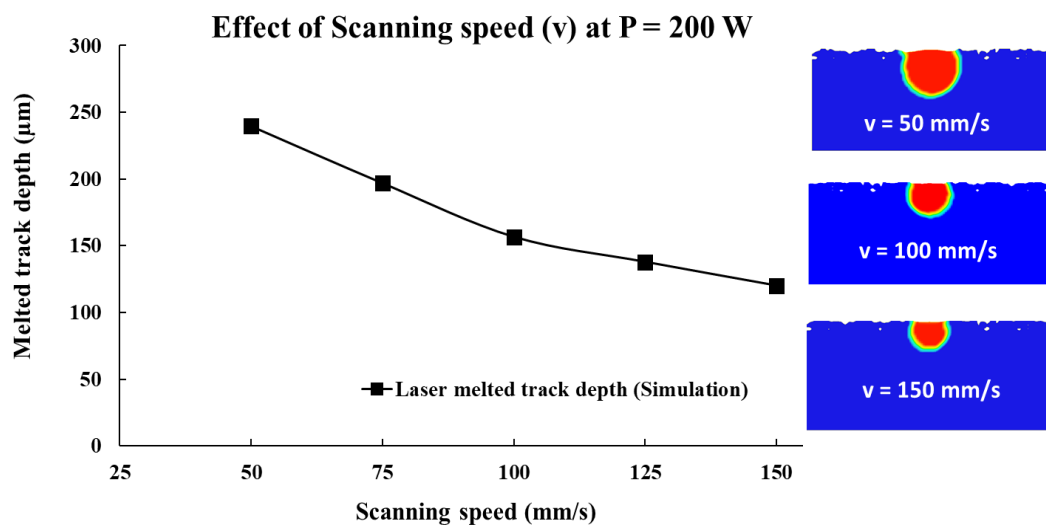


**Figure 4.18** The melted track depth with different scanning speed

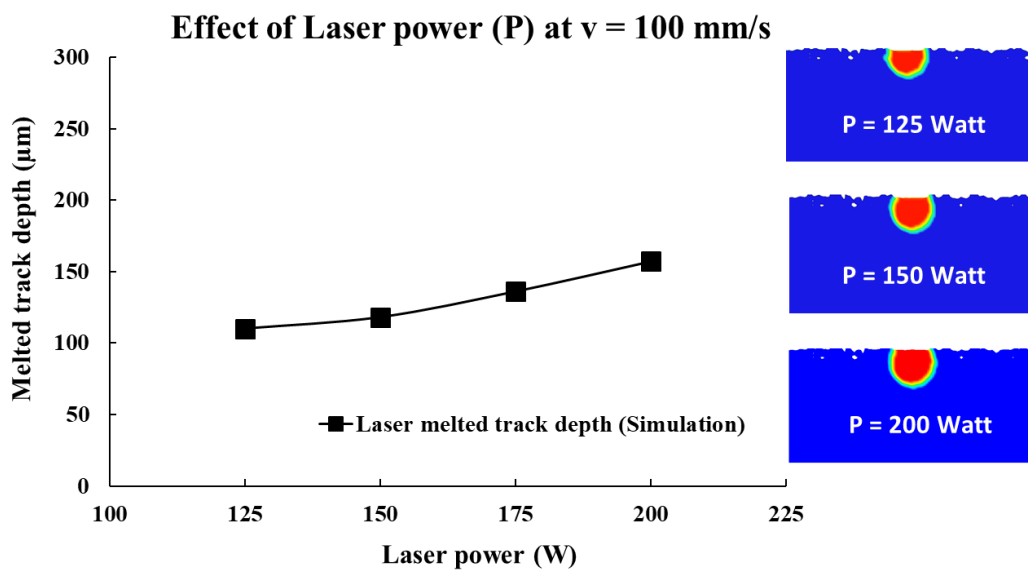


**Figure 4.19** The melted track depth with different laser power

d) The effect of hatch spacing on layer formation

The hatch spacing (distance between two neighboring tracks) is a significant laser process parameter to create full dense parts and smooth surface. Figure 4.20 (a) and (b) present the surface morphologies of the first layer formation with two different hatch spacing. The hatch spacing used in the study were set to 0.09 mm and 0.135 mm. The laser moving path (Zig-zag) was used in the study as shown in Figure 3.9. In the Figure 4.21 (a) and (b), the cross section of layer formation with different hatch spacing (mm) are displayed. The red color contour shows the melt region and the blue color presents solid or unmelt region. In the cross sectional microstructure, the effect of hatch spacing can be observed more clearly. When the gap between two neighboring tracks is increased, the separation with an increase of hatch spacing occurs.

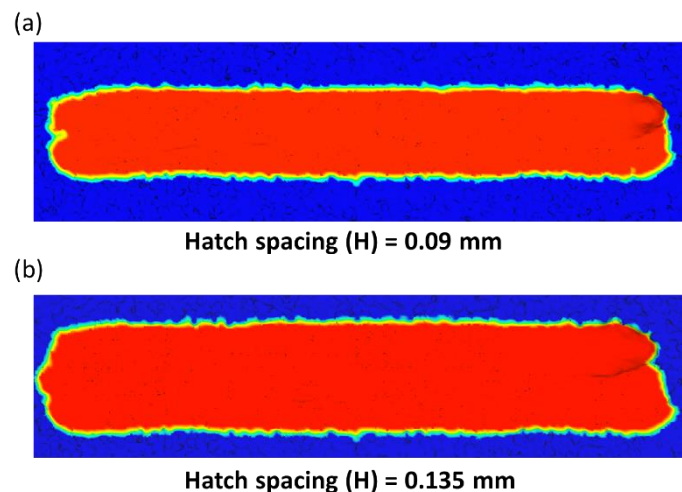


**Figure 4.20** Surface morphologies of the first layer formation with two different

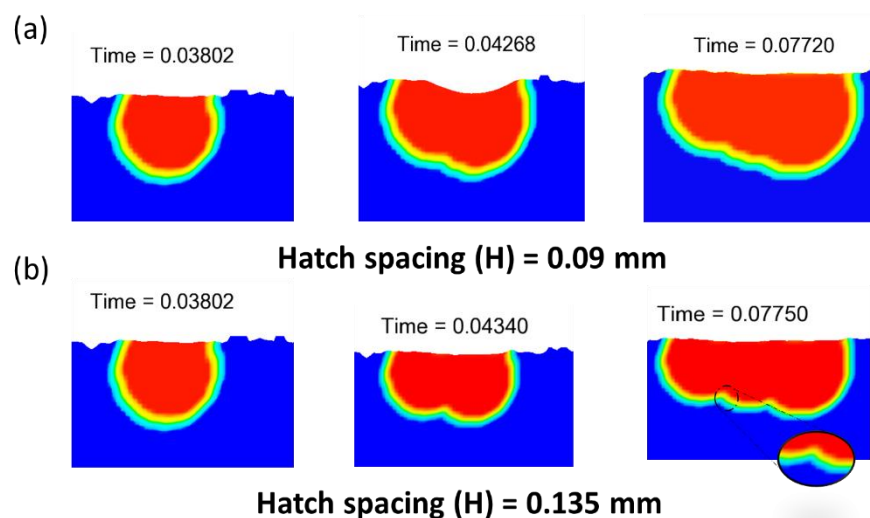


**Figure 4.21** the cross section of layer formation with different hatch spacing

## 4.2. Experimental results

### 4.2.1 The effect of scanning speed on melted track width

Figure 4.22 shows the influence of scanning speed on single track formation width. The average single track formation width varies from 150-250  $\mu\text{m}$ . The result revealed that the melted track width is decreased when the scanning speed is increased. The laser melted track width has a significant effect on determining the overlap rate of hatch spacing to produce the fully dense parts.

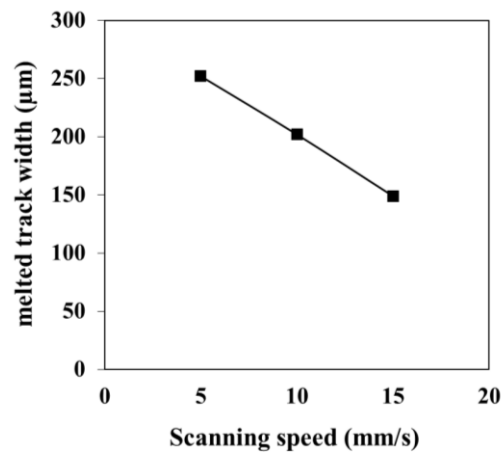


**Figure 4.22** The single track formation width with different scanning speed

### 4.2.2 Melt pool characteristic with low laser power (Max 50 Watt)

At the low laser power (Max 50 Watt), melt pool with low depth of penetration can expose due to low laser energy and oxidation reaction on the surface of melted metal powder. Figure 4.23 presents cross-section of the melt pool with low depth of penetration from (a) experiment, (b) simulation.

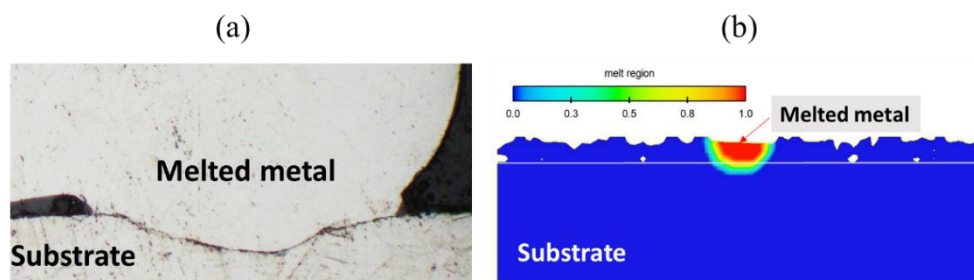


**Figure 4.23** Melt pool characteristic from (a) experiment, (b) simulation

### 4.2.3 Layer formation with different laser process parameters

The layer formation with different hatch spacing (0.1 mm (a) 0.3 mm (b) and 0.5 mm (c)) is shown in Figure 4.24. At  $H = 0.1$  mm, the discontinuous melted tracks

with balling effect were appeared due to oxidation reaction and the insufficient laser heat energy to fully melt the metal powder as shown in Figure 4.24 (a). The pores can be seen inside the layer formation. When increasing the hatch spacing to 0.3 mm, the discontinuous melted track with balling effect can be observed with the reduced balling size as shown in Figure 4.24 (b). Also, the pore fraction inside the layer was reduced. At  $H = 0.5$  mm, the discontinuous melting track with fragment or lack of fusion was observed and the laser melted track is arranged along laser scan pattern as shown in Figure 4.24 (c). In L-PBF process the hatch spacing is the significant process parameter that provide the good quality of products with less porosity. Figure 4.25 presents the layer formation with different scanning speed, 5 mm/s (a), 10 mm/s (b) and 15 mm/s (c). It was discovered that the discontinuous with fragment and instability of laser melted track occur at the scanning speed of 5 mm/s. When the scanning speed is increased to 10 mm/s, more continuous laser melted track was formed. At the scanning speed of 15 mm/s, the laser melted track cannot be completely melted. The pore from separated particles of metal powder inside the layer formation can be found due to insufficient laser energy density. The continuous melt track can be presented when the properly process parameters are applied.

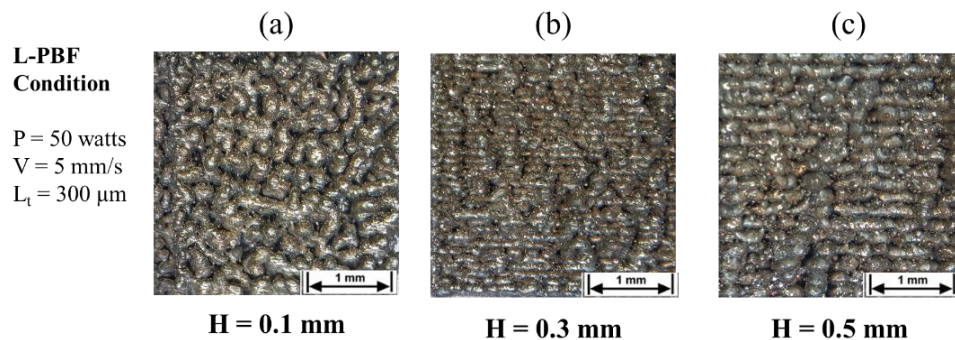


**Figure 4.24** The layer formation with different hatch spacing, (a)  $H = 0.1$  mm, (b)  $H = 0.3$  mm, (c)  $H = 0.5$  mm

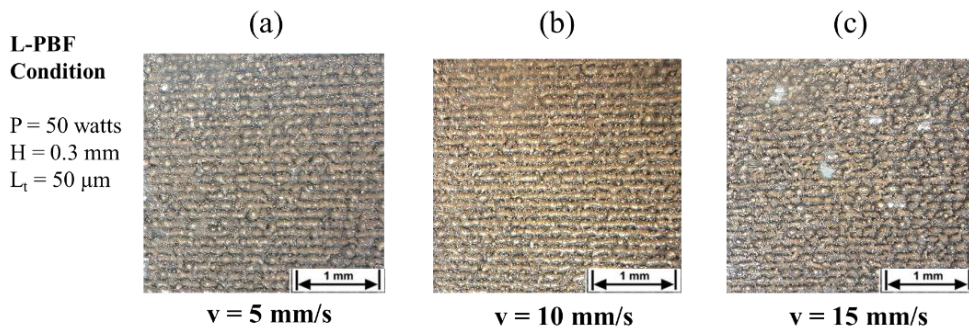


**Figure 4.25** The layer formation with different scanning speed, (a)  $v = 5$  mm/s, (b) 10 mm/s and (c) 15 mm/s

#### 4.2.4 Microstructure of AISI 316L stainless steel fabricated by L-PBF process

In L-PBF, the rapid melting and rapid solidification can occur with the microstructural evolution process. Figure 4.26 (a) shows the cross-section area of AISI 316L melted particle from case 1. The particle shown in this Figure is the one that has large size due to the balling effect. The microstructure of AISI 316L stainless steel fabricated by L-PBF process consists of cellular columnar structure oriented according to temperature gradient direction during rapid cooling as shown in Figure 4.26 (b), (c) and (d). In the L-PBF, the cellular-columnar structure can be formed due to the sufficiency of the ratio of temperature gradient and growth rate ( $G/R$ ) values. The cellular-columnar structure is a typical microstructure of AISI 316L stainless steel with rapid solidification.

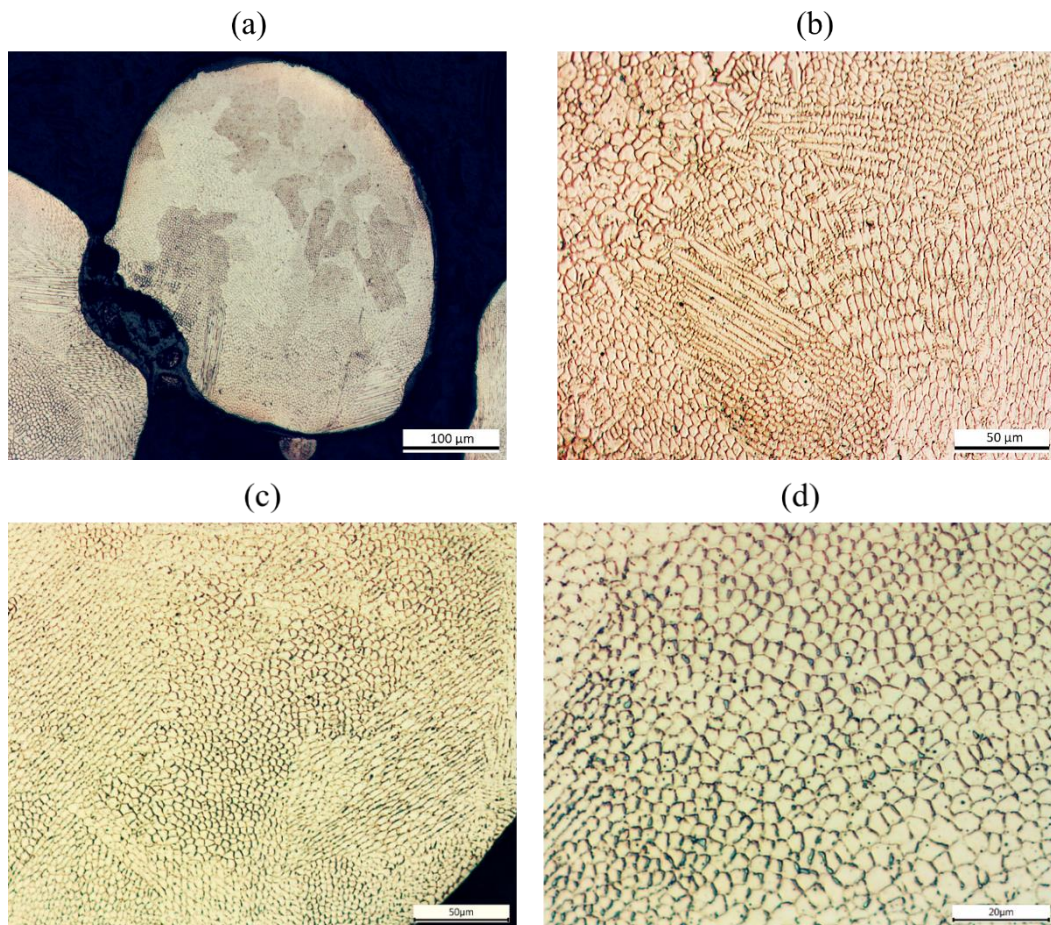


**Figure 4.26 AISI 316L Microstructure (a) cross section area of melted powder bed layer formation , (b), (c), (d) Microstructure of AISI 316L fabricated by L-PBF**

#### 4.2.5 Characterization the microstructure of AISI 316L fabricated by L-PBF process using Scanning electron microscope (SEM)

Figure 4.27 – 4.29 illustrate the cellular structure of AISI 316L stainless steel fabricated by L-PBF process with magnificant 5000x, 10,000x, 20,000x from scanning electron microscope. The chemical compositions of the 316L stainless steel obtained by scanning electron microscope with EDS technique is presented in Figure 4.30 - 4.33. The main chemical compositions of AISI 316L are Fe, Cr, Ni and Mo.

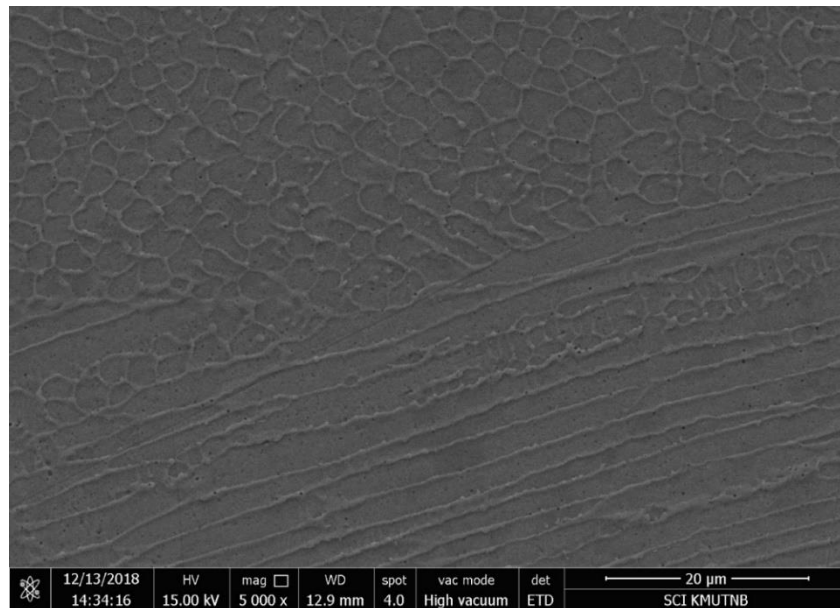


**Figure 4.27** The cellular and columnar dendrite structure of AISI 316L stainless steel fabricated by L-PBF process with magnificant 5000x

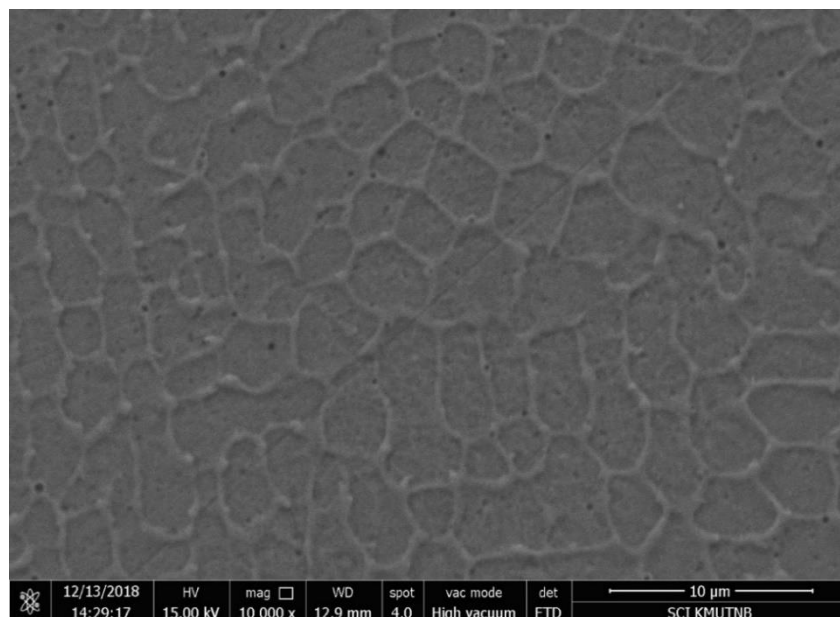


**Figure 4.28** The cellular structure of AISI 316L stainless steel fabricated by L-PBF process with magnificant 10000x

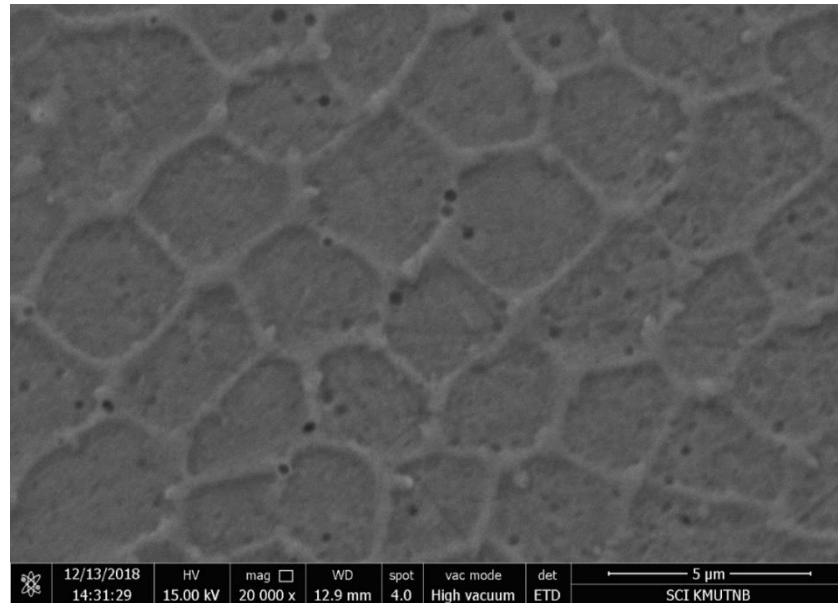


**Figure 4.29** The cellular structure of AISI 316L stainless steel fabricated by L-PBF process with magnificant 20000x

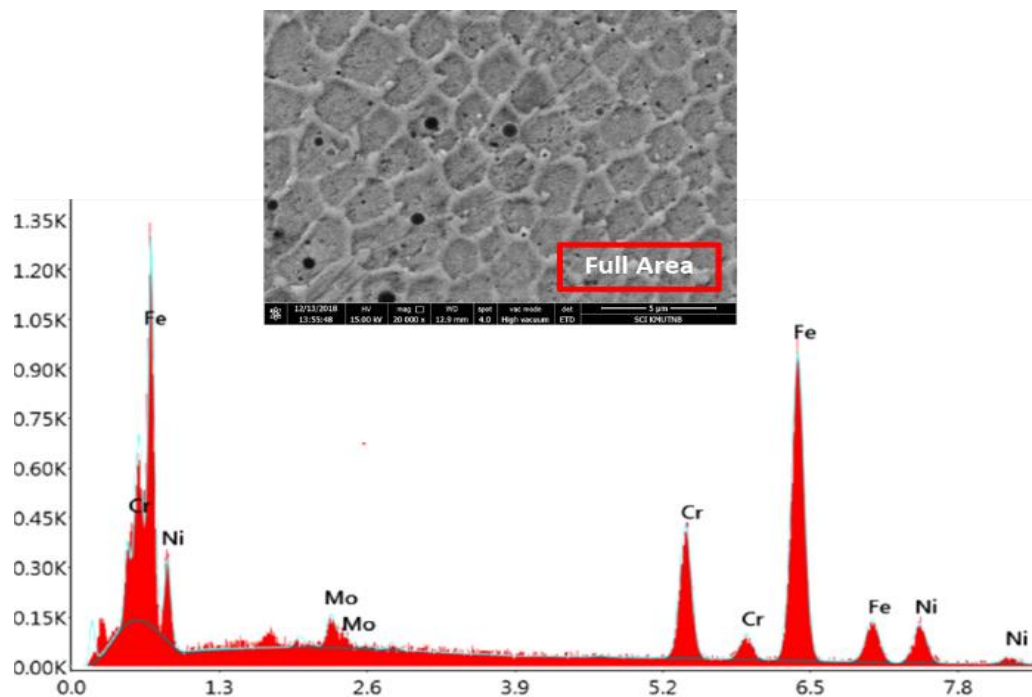


**Figure 4.30** The chemical composition of the cellular structure (full area) obtained by SEM-EDS

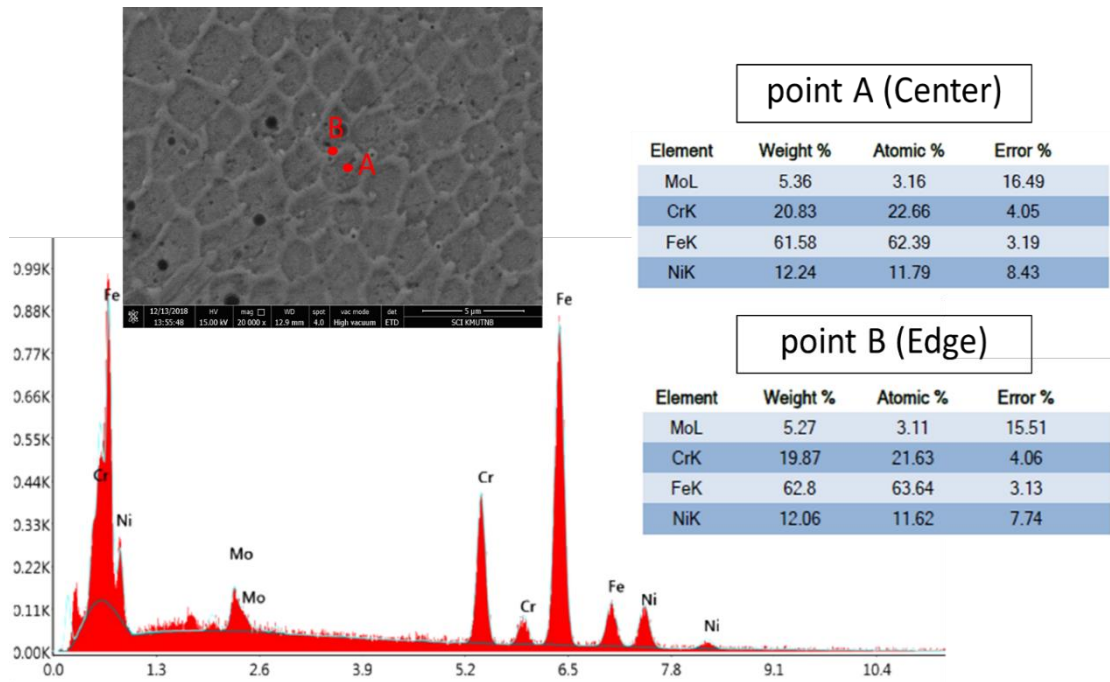


**Figure 4.31** The chemical composition of the cellular structure (point) obtained by SEM-EDS

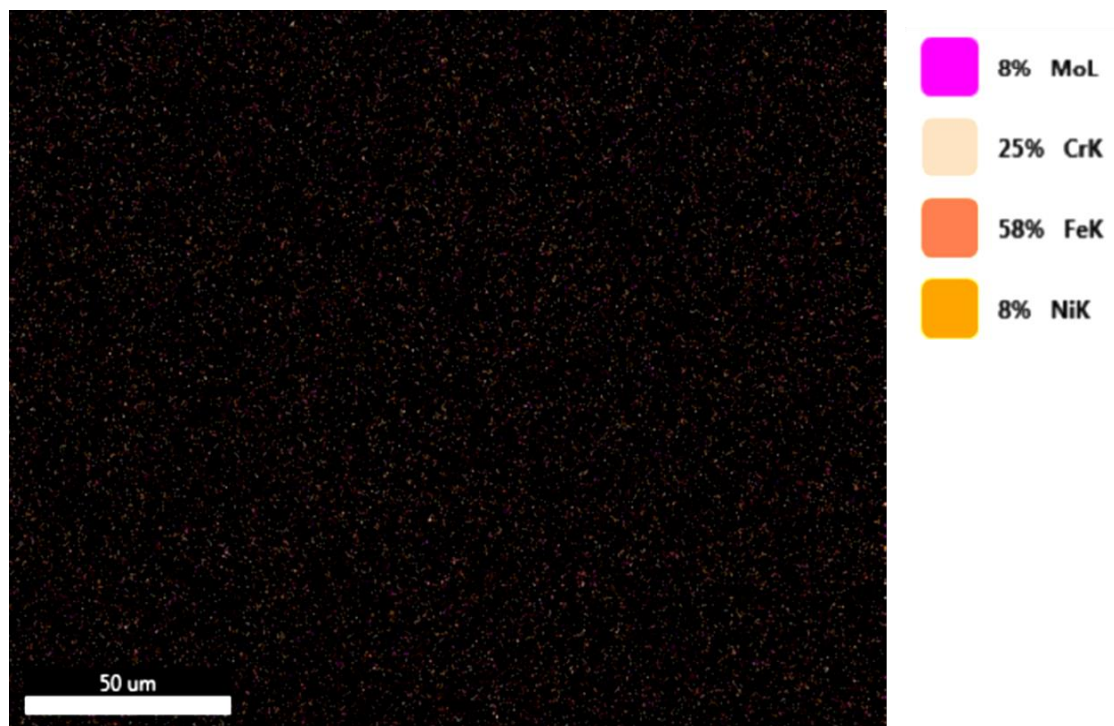


**Figure 4.32** The chemical composition of the cellular structure (Mapping) obtained by SEM-EDS

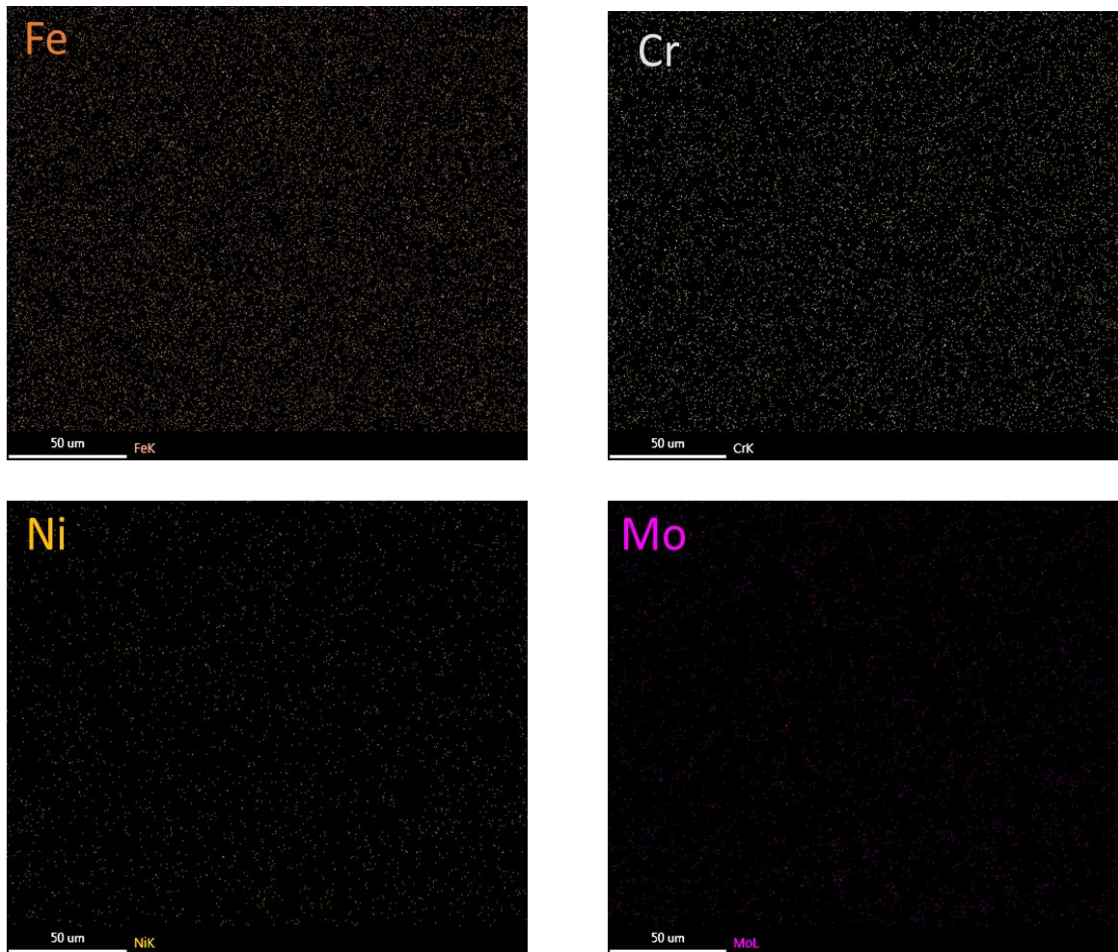


**Figure 4.33 The chemical composition of the cellular structure (Mapping) obtained by SEM-EDS**

#### **4.2.6 The effect of scanning speed and Hatch spacing on cellular structure**

The cellular structure of AISI 316L with different process parameters are shown in Figure 4.34 and 4.35. The ranges of scanning speed used in the experiment were 5 mm/s, 10 mm/s and 15 mm/s. The result revealed that the size of cell spacing is decreased with an increase of scanning speed as shown in Figure 4.34. Figure 4.35 shows the cellular structure with different hatch spacing (0.1 mm, 0.3mm and 0.5 mm). The experimental result presented that the higher the hatch spacing is, the lower the cell spacing size will take place.

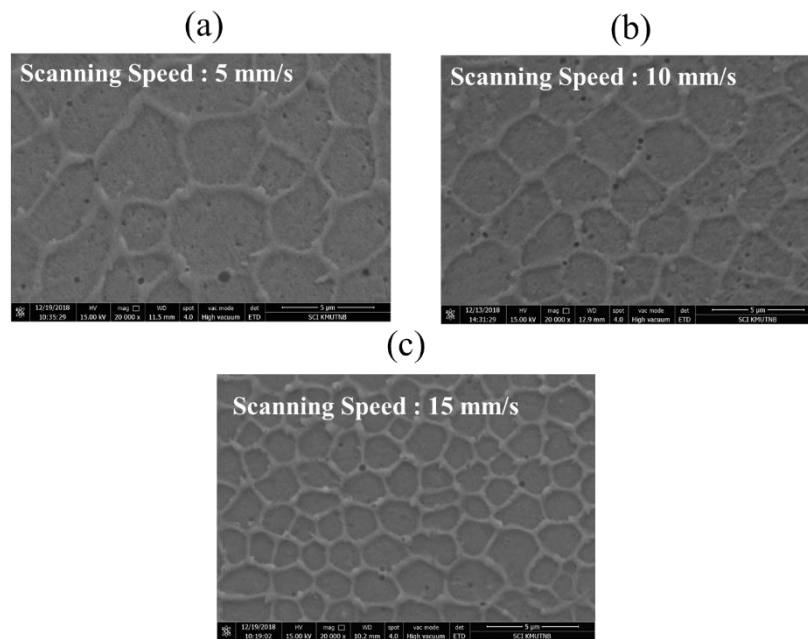


**Figure 4.34** The cellular structure with different scanning speed

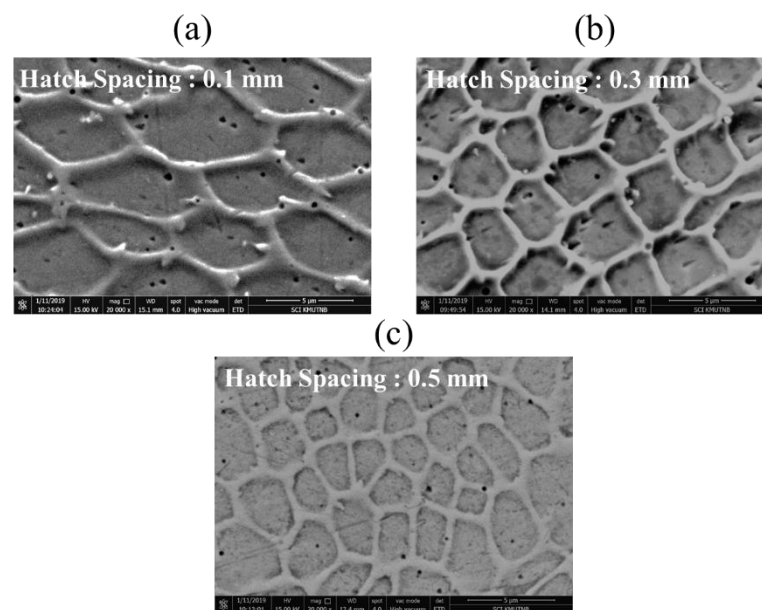


**Figure 4.35** The cellular structure with different hatch spacing

#### 4.2.7 Microhardness of AISI 316L fabricated by L-PBF process

##### *The effect of Hatch spacing on microhardness of AISI 316L*

The micro Vickers hardness of AISI 316L stainless steel fabricated by L-PBF process with different hatch spacings (0.1 mm, 0.3 mm and 0.5 mm) is shown in Figure

4.36. The result indicated that different hatch spacings have minor effects on the microhardness of AISI 316L.

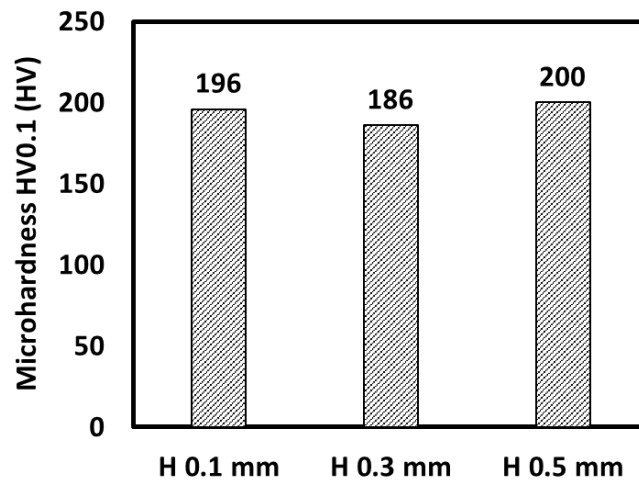


**Figure 4.36** Microhardness of AISI 316L fabricated by L-PBF process

*The microhardness of AISI 316L fabricated by L-PBF compared with conventional process*

The microhardness of L-PBF process compared with conventional process is presented in Figure 4.37. It was found that the laser powder bed fusion process can produce parts with higher microhardness than that of the conventional manufacturer due to the rapid cooling rate with finer grain of materials.

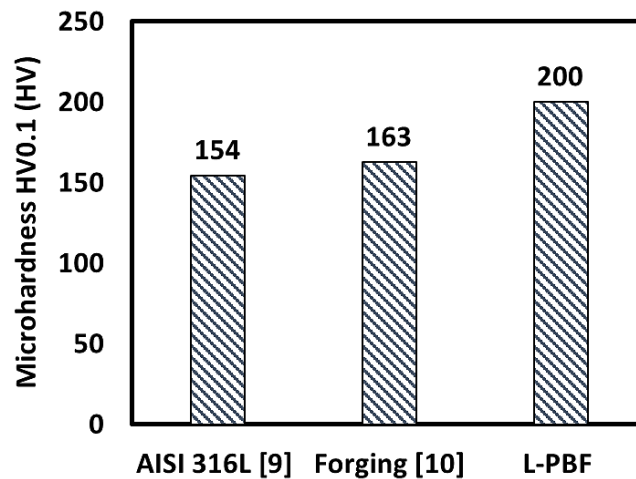


**Figure 4.37** The microhardness of L-PBF compared with the conventional process

---

## Chapter 5 Conclusions

The first part of the thesis was to study the effect of laser process parameters on physical phenomena in L-PBF process including temperature distribution, melt pool geometry, single track formation and layer formation of the stainless steels. The numerical study was applied in the first part of the thesis in order to study the effect of process parameters on physical phenomena in L-PBF process of stainless steels with different grades including AISI 304, AISI 420 and AISI 316. The result obtained from the numerical study were validated with the result from the experimental study.

The numerical results of AISI 304 showed that at some observed position in the specimen, the double speed of the moving heat source results in the decreasing of the temperature for around 30%. The increasing of power intensity from 200 W/mm<sup>2</sup> to 480 W/mm<sup>2</sup> results in the increasing of the temperature at the laser moving path for nearly double. It showed that the results from the simulation are consistent with the experimental results with minor difference.

The results of AISI 420 from the numerical study revealed that at the lower scanning speed, the temperature field has a region of heat distribution larger than that of the higher one. The geometry of melt pools can be changed from ellipse shape to tear drop shape when the scanning speed is increased. The width and depth of laser melting track is increased when the higher laser power and lower scanning speed are applied. The void is found underneath the laser melting track when the scanning speed changes from 0.4 m/s to 0.6 m/s. The results from the simulation is in agreement with the experimental results.

The results from both the simulation and the experiment of AISI 316L presented that the melted track width are narrowed gradually when the lower laser power and higher scanning speed are applied. The melted track width measured from the experimental study was 10-20  $\mu\text{m}$  wider than that of the simulation. The depth of melted track is decreased when the higher scanning speed and lower laser power are applied. The results from the simulation is in agreement with the experimental results.

The second part of the thesis was to study the effect of laser process parameters on the single track formation, layer formation, of AISI 316L stainless steel fabricated by L-PBF process. The results from the experimental study revealed that the laser melted track width is decreased from 250 to 150 micron when the scanning speed is increased from 5 to 15 mm/s. experimental study and material characterization. The discontinuous with fragment and instability of laser melted track occur at the scanning speed of 5 mm/s. When the scanning speed is increased to 10 mm/s, more continuous laser melted track was formed. At the scanning speed of 15 mm/s, the laser melted track cannot be completely melted. The pore from separated particles of metal powder inside the layer formation can be found due to insufficient laser energy density. The discontinuous melted tracks with balling effect were appeared at H 0.1 mm due to oxidation reaction and the insufficient laser heat energy to fully melt the metal powder. The pores can be seen inside the layer formation. When increasing the hatch spacing to 0.3 mm, the discontinuous melted track with balling effect can be observed with the reduced balling size as Also, the pore fraction inside the layer was reduced. At H= 0.5 mm, the discontinuous melting track with fragment was observed and the laser melted track is arranged along laser scan pattern.

In addition, it was found that the microstructure of AISI 316L stainless steel fabricated by L-PBF process consists of cellular columnar structure and dendrite structure oriented according to temperature gradient direction. The size of cell spacing is decreased with an increase of scanning speed and hatch spacing. The experimental result also showed that the L-PBF process can produce the final parts with higher microhardness than that of the conventional manufacturer due to rapid cooling rate and small grain size.

This thesis provides clearer comprehension which can be beneficial to the improvement of the L-PBF process optimization. In addition, the information from this thesis can be useful for the simulation of the thermal-stress model and for the prediction of the mechanical properties, microstructure transformation and part distortion in the future work. Moreover, the results obtained from the experimental study can be useful for the further research studies in metal 3D printing process in the coming future of the fourth industrial revolution in Thailand.

---

## Bibliography

- [1] B. Berman, 3-D printing: the new industrial revolution, *Bus Horizons*, Vol. 5, 2012, pp. 155-162.
- [2] S-curve and new S- curve (New engine of growth), Office of industrial economics, Thailand.
- [3] W. E. Frazier, Metal Additive Manufacturing: A Review, *Journal of Materials Engineering and Performance*, Vol. 23 (6) ,2014, pp. 1917–1928.
- [4] D. L. Bourell, M.C. Leu, J. J. Beaman and D.W. Rosen, A Brief History of Additive Manufacturing and the 2009 Roadmap for Additive Manufacturing: Looking Back and Looking Ahead, US – TURKEY Workshop on Rapid Technologies, 2009, pp. 5-11.
- [5] T. Wohlers, Additive Manufacturing State of the Industry, Wohlers report, 2010, pp. 1-26.
- [6] V. Bhavar, P. Kattire, V. Patil, S. Khot, K. Gujar and R. Singh, A Review on Powder Bed Fusion Technology of Metal Additive Manufacturing, International conference and exhibition on Additive Manufacturing Technologies-AM-2014, Bangalore, India, 2014.
- [7] P. Eriksson, Evaluation of mechanical and microstructural properties for laser powder-bed fusion 316L, Uppsala university, 2018.
- [8] D. Thomas, The Development of Design Rules for Selective Laser Melting, Ph. D Thesis University of Wales Institute Cardiff, 2009.
- [9] Y. S. Lee and W. Zhang, Mesoscopic Simulation of Heat Transfer and Fluid Flow in Laser Powder Bed Additive Manufacturing, International Solid Free Form Fabrication Symposium Austin, 2015, pp. 1154-1165.

- 
- [10] M. Megahed, H. W. Mindt, N. N. Dri, H. Duan and O. Desmaison, Metal additive-manufacturing process and residual stress modeling, *Integrating Materials and Manufacturing Innovation*, Vol. 5 (4), 2016, pp. 1-33.
- [11] Metal 3D Printing: Which Technologies for Which Applications, <https://www.sculpteo.com/blog/2017/05/23/metal-3d-printing-which-technologies-for-which-applications> (accessed on 20 September 2018).
- [12] I. Gibson, D. Rosen, and B. Stucker, *Additive Manufacturing Technologies: 3D Printing, Rapid Prototyping, and Direct Digital Manufacturing*. New York, NY: Springer New York, 2015, ISBN: 978-1-4939-2112-6.
- [13] Loughborough University. Binder Jetting | Additive Manufacturing Research Group, <http://www.lboro.ac.uk/research/amrg/about/binderjetting/> (accessed on 1 May 2018).
- [14] Digital Metal. How Digital Metal works, <https://digitalmetal.tech/home/digital-metal/how-it-works/> (accessed on 1 May 2018).
- [15] S. Matt, Metal 3D Printing: Laser Sintering vs. Bulk Sintering in a Furnace – Pros and Cons, <https://3dprint.com/193946/laser-sintering-vs-bulk-sintering/> (accessed on 5 Jan 2019).
- [16] K. Zeng, D. Pal and B. Stucker, A review of thermal analysis methods in Laser Sintering and Selective Laser Melting, *Journal of Heat Transfer*, 2012, pp. 796-814.
- [17] I. A. Roberts, C. J. Wang, R. Esterlein, M. Stanford and D. J. Mynors, A three-dimensional finite element analysis of the temperature field during laser melting of metal powders in additive layer manufacturing, *International Journal of Machine Tools & Manufacture*, Vol. 49, 2009, pp. 916–923.
- [18] X. Mu, S. Meissner, H. Meissner and A. W. Yu, High-efficiency crystalline fiber waveguide lasers, *SPIE Newsroom*, 2015, pp. 1-3.
- [19] K. Saeidi, *Stainless steel fabricated by laser melting*, Doctoral Thesis Stockholm University, 2016.

- 
- [20] J. Berkmanns, M. Faerber, U. Bheim, Facts about laser technology: Laser cutting. [http://www.laserdeal.com/english\\_technicalinformation](http://www.laserdeal.com/english_technicalinformation). (accessed on 5 Jan 2019).
- [21] K. Carolin, B. Andreas and E. Attar, Fundamental consolidation mechanisms during selective beam melting of powders, *Model Simul Mater Sci Eng*, Vol. 21, 2013, pp. 1-18.
- [22] K. Alexander, B. Andreas and K. Carolin, Modelling of electron beam absorption in complex geometries, *Journal of Physics D: Applied Physics*, Vol. 47 (60), 2014, pp. 1-11.
- [23] M. Chiumenti, E. Neiva, E. Salsi, M. Cervera, S. Badia, C. Davies, Z. Chen, AND C. lee, Numerical modelling and experiment validation in selective laser melting, *Journal of Heat Transfer*, Vol. 130 (6), 2008, pp. 1-21.
- [24] H. S. Carslaw and J. C. Jaeger, *Conduction of Heat in Solids*, Oxford University Press, Amen House London E.C., 1959,
- [25] A. M. Kamara, W. Wang, S. Marimuthu, and L. Li, Modelling of the melt pool geometry in the laser deposition of nickel alloys using the anisotropic enhanced thermal conductivity approach, *Proc. IMechE*, Vol. 225, 2010, pp. 87-99.
- [26] Y. Zhang, A. Faghri, C. W. Buckley and T. L. Bergman, Three-Dimensional Sintering of Two-Component Metal Powders with Stationary and Moving Laser Beams, *Transactions of the ASME*, Vol. 122, 2000, pp.150-158.
- [27] B. Xiao and Y. Zhang, Marangoni and Buoyancy Effects on Direct Metal Laser Sintering with a Moving Laser Beam, *Numerical Heat Transfer*, Vol. 51, 2007, pp. 715-733.
- [28] S. A. Khairallah, A. T. Anderson, A. Rubenchik and W. E. King, Laser powder-bed fusion additive manufacturing: Physics of complex melt flow and formation mechanisms of pores, spatter, and denudation zones, *Acta Materialia*, Vol. 108, 2016, pp. 36 – 45.
- [29] S. David and J. Vitek, *Principle of Weld solidification and Microstructure*, *International trends in Welding Science and Technology*, ASM, 1993, pp. 147-157.

- 
- [30] X. Zhao, Q. Wei, B. Song, Y. Liu, X. Luo, S. Wen, and Y. Shi, Fabrication and Characterization of AISI 420 Stainless Steel Using Selective Laser Melting, *Materials and Manufacturing Processes*, 2015, pp. 1–7.
- [31] Y.F. Shen, D.D. Gu and Y.F. Pan, Balling Process in Selective Laser Sintering 316 Stainless Steel Powder, *Key Engineering Materials*, Vol. 301-306, 2006, pp. 357-360.
- [32] J. Deletian and W. Wood, Principle of joining Metallurgy, *Metals Handbook*, Vol. 6, 1983, pp. 22-49.
- [33] The weld microstructure, [https://mafiadoc.com/the weld microstructure](https://mafiadoc.com/the-weld-microstructure) (accessed on 22 June 2018).
- [34] Ch. Stephen, Metal casting: a sand casting manual for the small foundry, Vol. 2 (4), ISBN 978-0-9702203-3-2, 2014.
- [35] P. Schmidt, Heat transfer during filling in die casting processes, *Materials Science and Engineering: A*, Vol. 173, 1993, pp. 271-274.
- [36] Metal Casting Processes, <https://slideplayer.com/slide/5815332/> (accessed on 30 June 2018).
- [37] B. Song, X. Zhao, S. Li, Ch. Han, Q. Wei, S. Wen, J. Liu, and Y. Shi, Difference in Microstructure and properties between selective laser melting and traditional manufacturing for fabrication of metal parts: A review, *Frontiers of Mechanical Engineering*, Vol. 10 (12), 2015, pp. 111-125.
- [38] Stainless Steel - Properties, Fabrication and Applications, <https://www.azom.com>, (accessed on 5 Jan 2019).
- [39] Stainless Steel - Grade 304 - Properties, Fabrication and Applications, <https://www.azom.com> (accessed on 5 Jan 2019).
- [40] Stainless Steel - Grade 420 - Properties, Fabrication and Applications, <https://www.azom.com> (accessed on 5 Jan 2019).

- 
- [41] Stainless Steel - Grade 316L - Properties, Fabrication and Applications (UNS S31603)., <https://www.azom.com> (accessed on 5 Jan 2019).
- [42] J. W. Elmer, The Influence of Cooling Rate on the Microstructure of Stainless Steel Alloys, Ph.D. Thesis Massachusetts institute of technology, 1988.
- [43] Fe-Cr-Ni ternary phase diagram at room temperature, <https://www.quora.com/What-is-a-ternary-phase> (accessed on 15 August 2018).
- [44] H. Abe and Y. Watanabe, Low-Temperature Aging Characteristics of Type 316L Stainless Steel Welds: Dependence on Solidification Mode, Metallurgical and materials transactions A, Vol. 39, 2008 pp. 1392-1398.
- [45] A. L. Schaeffler, Constitution Diagram for Stainless Steel Weld Metal." Metals Progress Vol. 56 (B), 1949.
- [46] A. L. Schaeffler, Selection of Austenitic Electrodes for Welding Dissimilar Metals, The Welding Journal, Vol. 20 (10), 1947.
- [47] J. M. Yitck, A. Dasgupta. and S. A. Da, Microstructural Modification of Austenitic Stainless Steel by Rapid Solidification." Metallurgical Transactions, Vol. 14 (A), 1983 pp. 1833-1841.
- [48] J. M. Vitck and S. A. Da, Microstructural Analysis of Austenitic Stainless Steel Laser Welds, in Trends in Welding Research in the United States (American Society for Metals. Ohio. 198:). pp. 243-258.
- [49] L. E. Loh, Ch. K. Chua, W. Y. Yeong, J. Song, M. Mapar, S. L. Sing, Z. H. Liu, and D. Q. Zhang, Numerical investigation and an effective modelling on the Selective Laser Melting (SLM) process with aluminium alloy 6061, International Journal of Heat and Mass Transfer, Vol. 80, 2015, pp. 288-300.
- [50] W. Huang, X. Lin, and J. Chen, Laser Solid Forming: Rapid Fabrication of Dense Metal Parts with High Performance. Xi'an: Publishing House of Northwestern Polytechnical University, 2007.
- [51] P. F. Jacobs, Rapid prototyping & manufacturing: fundamentals of stereolithography, Society of Manufacturing Engineers, 1992.

- 
- [52] Z. Brytan, Comparison of vacuum sintered and selective laser melted steel AISI 316L, *Arch. Metall. Mater.*, 2017, Vol. 62 (4), pp. 2125-2131.
- [53] C. Y. Yap, C. K. Chua, Z. L. Dong, Z. H. Liu, D. Q. Zhang, L. E. Loh, and S. L. Sing, Review of selective laser melting: Materials and applications, *Applied physics reviews*, Vol. 2, 2015, pp. 1-20.
- [54] G. Jandin, J. M. Bertin, L. Dembinski, and C. Coddet, *Manufacture of Stainless Steel Parts by Selective Laser Melting Process*, CRC Press, 2005, pp. 431–434.
- [55] I. Tolosa, F. Garciandia, F. Zubiri, F. Zapirain, and A. Esnaola, *International Journal of Advanced Manufacturing Technology*, Vol. 51, 2010, pp. 639–647.
- [56] I. Yadroitsev, and I. Smurov, Selective laser melting technology: from the single laser melted track stability to 3D parts of complex shape, *Physics Procedia*, Vol. 5, 2010, pp. 551-560.
- [57] R. Li, J. Liu, Y. Shi, L. Wang, and W. Jiang, Balling behavior of stainless steel and nickel powder during selective laser melting process, *International Journal of Advanced Manufacturing Technology*, Vol. 59, 2012, pp. 1025-1035.
- [58] I. Yadroitsev, and I. Smurov Surface Morphology in Selective Laser Melting of Metal Powders, *Physics Procedia*, Vol. 12, 2011, pp. 264-270.
- [59] R. Li, J.Liu, Y. Shi, M. Z. Du, and Z. Xie, 316L Stainless Steel with Gradient Porosity Fabricated by Selective Laser Melting, *Journal of Materials Engineering and Performance*, Vol. 19 (5), 2010, pp. 666–671.
- [60] J. A. Cherry, M. Davies, S. Mehmood, N. P. Lavery, S. G. R. Brown, J. Sienz, Investigation into the effect of process parameters on microstructural and physical properties of 316L stainless steel parts by selective laser melting, *International Journal of Advanced Manufacturing Technology*, Vol. 76, 2015, pp. 869–879.
- [61] V. Sufiiarov, E. Borisov, I. Polozov, and D. Masaylo, Study of microstructure and properties of 316L steel after selective laser melting, *Proc. of the METAL 2016 - 25th Anniversary International Conference on Metallurgy and Material*, Brno, Czech Republic, EU, 2016, pp. 659-663.

- 
- [62] Y. Zhong, L. f. Liu, S. Wikman, D. Cui, Z. Shen, Intragranular cellular segregation network structure strengthening 316L stainless steel prepared by selective laser melting, *Journal of Nuclear Materials*, Vol. 470, 2016, pp. 170–178.
- [63] D. Herzog, V. Seyda, E. Wycisk, and C. Emmelmann, Additive manufacturing of metals, *Acta Materialia*, Vol. 117, 2016, pp. 371–392.
- [64] J. P. Choi, G. H. Shin, M. Brochu, Y. J. Kim, S. S. Yang, K. T. Kim, D. Y. Yang, Ch. W. Lee, and J. H. Yu, Densification Behavior of 316L Stainless Steel Parts Fabricated by Selective Laser Melting by Variation in Laser Energy Density, *Materials Transactions*, Vol. 57 (11), 2016, pp. 1952 -1959.
- [65] Y. Zhang, A. Faghri, C. W. Buckley and T. L. Bergman, Three-Dimensional Sintering of Two-Component Metal Powders with Stationary and Moving Laser Beams, *Transactions of the ASME*, Vol. 122, 2000, pp.150-158.
- [66] B. Xiao and Y. Zhang, Marangoni and Buoyancy Effects on Direct Metal Laser Sintering with a Moving Laser Beam, *Numerical Heat Transfer*, Vol.51, 2007, pp. 715-733.
- [67] W. L. Chen, Y. C. Yang and H. L. Lee, Estimating the absorptivity in laser processing by inverse methodology, *Applied Mathematics and Computation*, 2007, pp. 712-721.
- [68] C. Konrad, Y. Zhang, and B. xiao, Analysis of melting and resolidification in a two-component metal powder bed subjected to temporal Gaussian heat flux, *International Journal of Heat and Mass Transfer*, 2005, pp. 3932-3944.
- [69] Y. Li and D. Gu, Thermal behavior during selective laser melting of commercially pure titanium powder: Numerical simulation and experimental study, *Additive Manufacturing*, Vol. 1–4, 2014, pp. 99–109.
- [70] N. P. Lavery, S. G. R. Brown, J. Sienz, J. Cherry and F. Belblidia, A review of Computational Modelling Additive Layer Manufacturing – multi-scale and multi-physics, *Design and Manufacturing*, 2014, pp. 668-690.

- 
- [71] V. R. Voller and C. Prakash, A Fixed-Grid Numerical Modeling Methodology for Convection-Diffusion Mushy Region Phase-Change Problems, *International journal Heat Mass Transfer*, Vol. 30, 1987, pp. 1709-1720.
- [72] K.H. Leitz, P. Singer, A. Plankensteiner, B. Tabernig, H. Kestler, and L.S. Sigl, Multi-physical simulation of selective laser melting, *Metal Powder Report*, Vol. 72 (5), 2017, pp. 333-338.
- [73] Y. Ch. Wu, W.S. Hwang, C.H. San, C. H. Chang, and H.J. Lin, Parametric study of surface morphology for selective laser melting on Ti6Al4V powder bed with numerical and experimental methods, *International Journal of Material Forming*, 2017, pp. 1-7.
- [74] T. D. Ngoa, A. Kashania, G. Imbalzanoa, K.T.Q. Nguyena, and D. Huib, Additive manufacturing (3D printing): A review of materials, methods, applications and challenges, *Composites Part B*, Vol. 143, 2018, pp. 172–196.
- [75] Metal 3D Printing Technology, <https://creatz3d.com.sg/metal-3d-printers/technology/> (accessed on 9 August 2018).
- [76] Binder Jetting 3D Printing: Everything You Need To Know, <https://3dsourced.com/3d-printing-technologies/binder-jetting/> (accessed on 9 August 2018).
- [77] High Level Processes: Directed Energy Deposition, <https://www.bintoa.com/DED> (accessed on 9 August 2018).
- [78] K. C. M, Recommended Values of Thermophysical Properties for Selected Commercial Alloys, Woodhead Publishing, 2002.
- [79] A. Srivastava, Moving heat Source Version 4.1, <https://appstore.ansys.com>, ANSYS, Inc (accessed on 1 Aug 2017).
- [80] Flow3d: Version 11.0.1.2 (2014): User manual, Flow science, Santa Fe, NM, USA.

[81] M. H. Hong, B. K. M, and T. Y. Kwon, The Influence of Process Parameters on the Surface Roughness of a 3D-Printed Co–Cr Dental Alloy Produced via Selective Laser Melting, *Appl. Sci*, Vol. 6 (401), 2016, pp. 1-10.

[82] AMPERPRINT® Additive Manufacturing powders Höganäs, <https://www.hoganas.com/> (accessed on 29 Jan 2019).

---

# Biography

## Personal information

Name: Patiparn Ninpetch  
Date of Birth: 8 /June /1994  
Place of Birth: Prachubkhirikhan province  
Nationality: Thai  
Address: 15/3 M.5, Thakanun, Thongpapoom, Kanchanaburi,  
71180  
Telephone: 080-6517807  
Email: patiparn.nin@gmail.com

## Education

2016- Present                      Master of Engineering in Material and Metallurgical  
Engineering (M.Eng) The Sirindhorn International Thai-  
German Graduate School of Engineering (TGGS), King  
Mongkut's University of Technology North Bangkok  
(KMUTNB), Thailand, GPA: 3.54

2012- 2016                         Bachelor of Engineering in Production Engineering (B.  
Eng) King Mongkut's University of technology North  
Bangkok (KMUTNB), Thailand, GPA: 3.04

2010-2012                         Vocational Education in Machine tool & Maintenance  
Don Bosco Banpong technological college, GPA 3.75

## Experience Internship

2017                                      Powder Metallurgy Research and Development Unit  
(PM\_RDU) National Metal and Materials Technology

Center, Pathum Thani 12120, Thailand, since 15 June 2017 until 30 October 2017

Topic: A Numerical Study on the Thermal Transient Model with Moving Laser Heat Source of AISI 304 stainless steel plate

2015

Powder Metallurgy Research and Development Unit (PM\_RDU) National Metal and Materials Technology Center, Pathum Thani 12120, Thailand, since 2 June 2015 until 29 July 2015

Topic: Study on Microstructures and Mechanical Properties of Sintered and Quenched Fe-Cr-Mo-C steel added with BN

## **International Conferences**

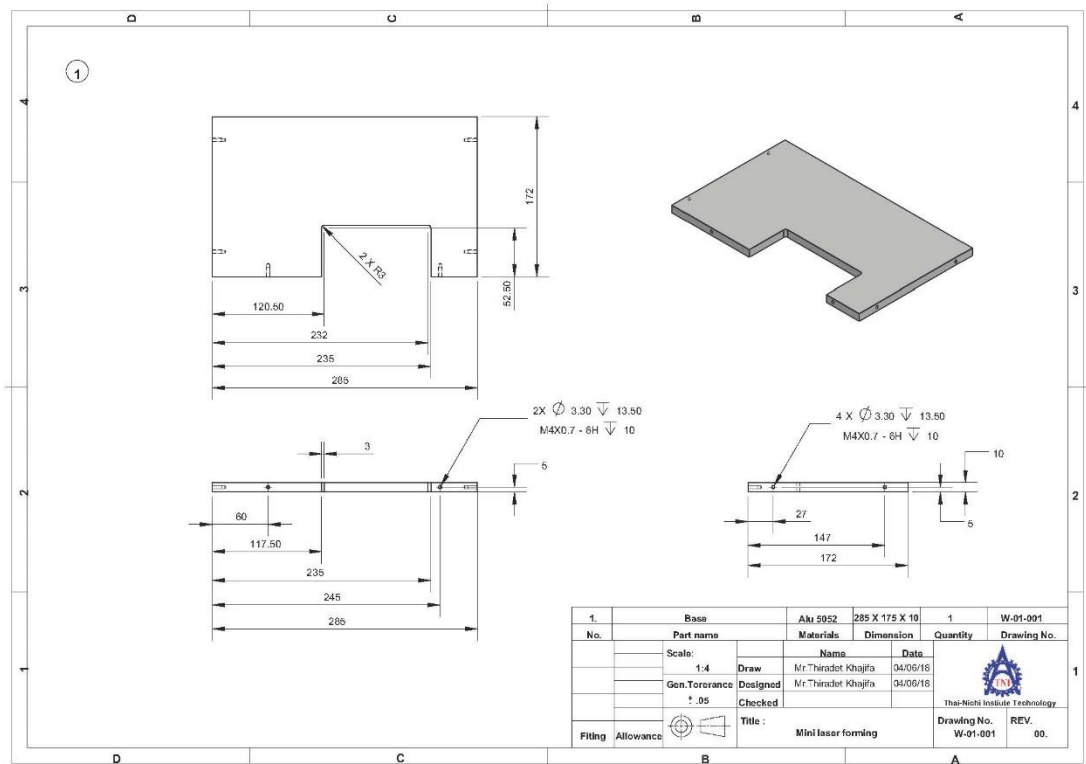
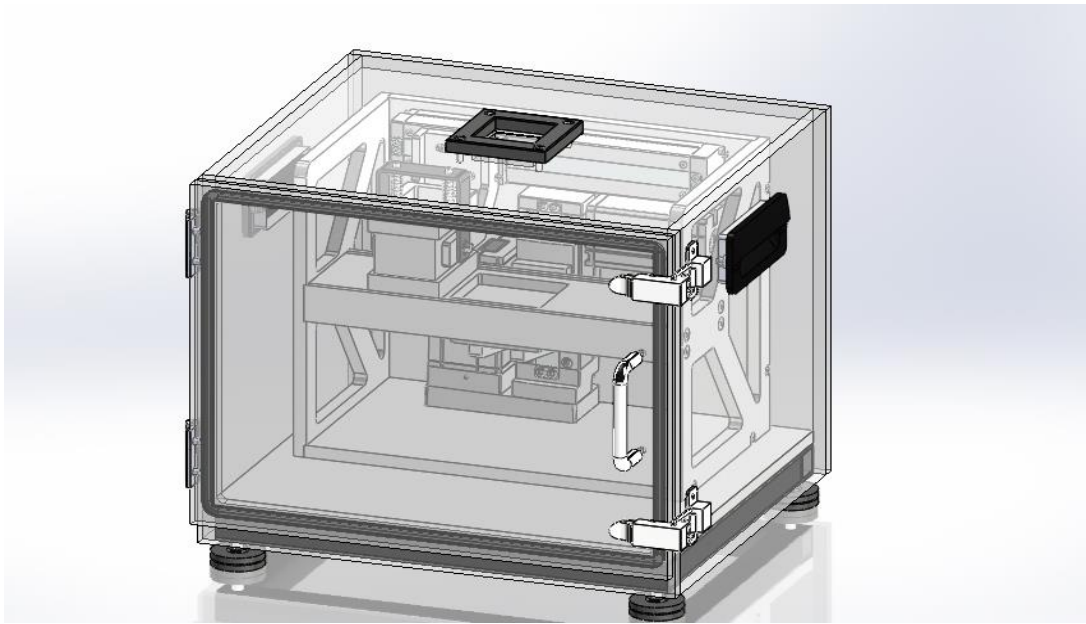
**Patiparn Ninpetch**, Pruet Kowitwarangkul, A Numerical Study on the Thermal Transient Model with Moving Laser Heat Source of AISI 304 stainless steel plate, The First Materials Research Society of Thailand International Conference (1<sup>st</sup> MRS Thailand International Conference) Convention Center, The Empress Hotel, Chiang Mai, Thailand October 31<sup>st</sup> - November 3<sup>rd</sup>, 2017.

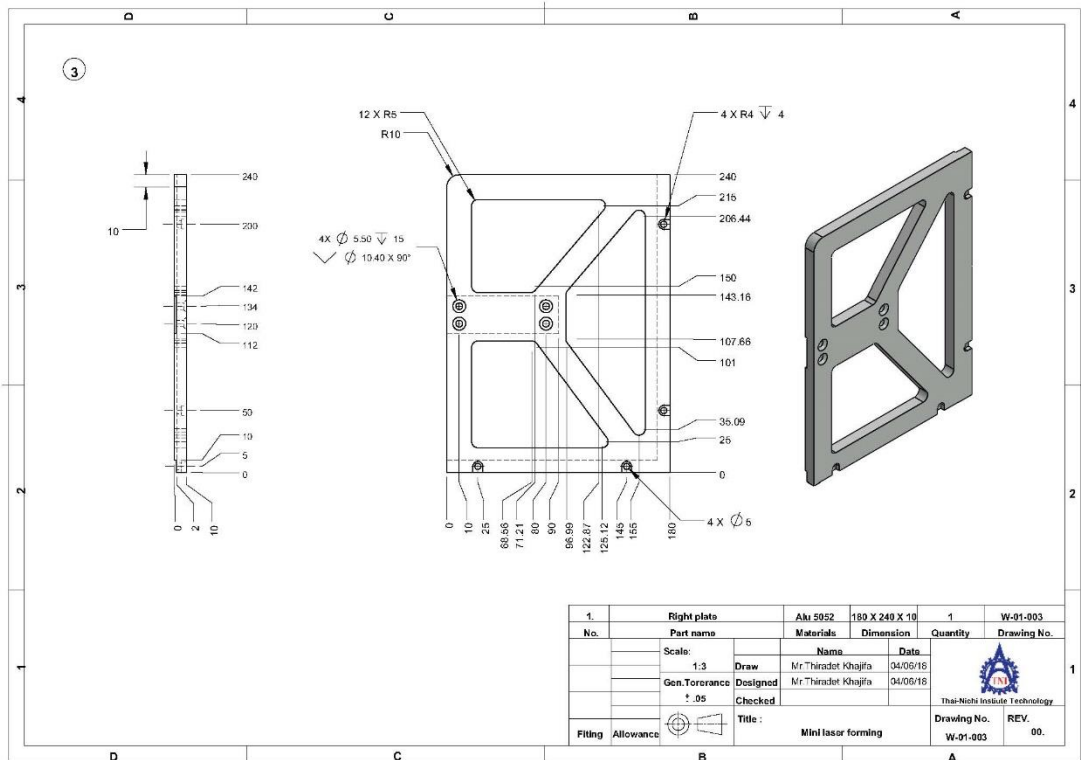
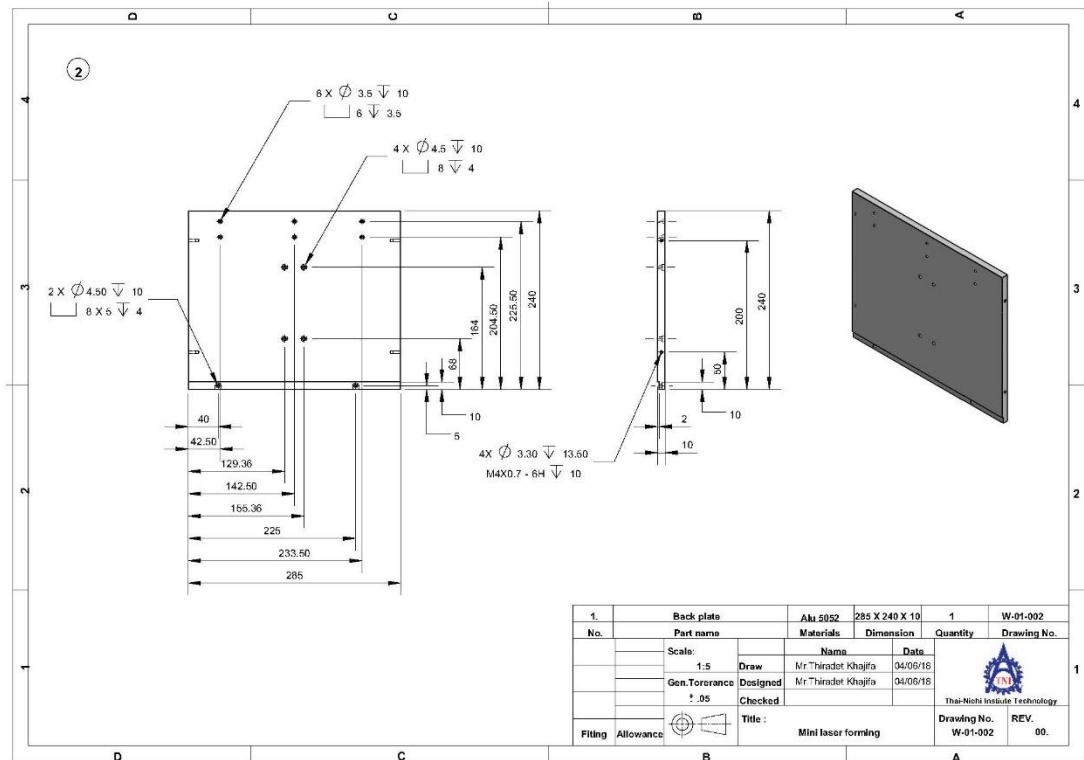
**Patiparn Ninpetch**, Pruet Kowitwarangkul, Sithipong Mahathanabodee, Ruangdaj Tongstri and Phadungsak Ratanadecho, Thermal and Melting Track Simulations of Laser Powder Bed Fusion (L-PBF), International Conference on Materials Research and innovation (ICMARI), The Emerald Hotel Bangkok, Thailand December 17<sup>th</sup> – 21<sup>th</sup>, 2018.

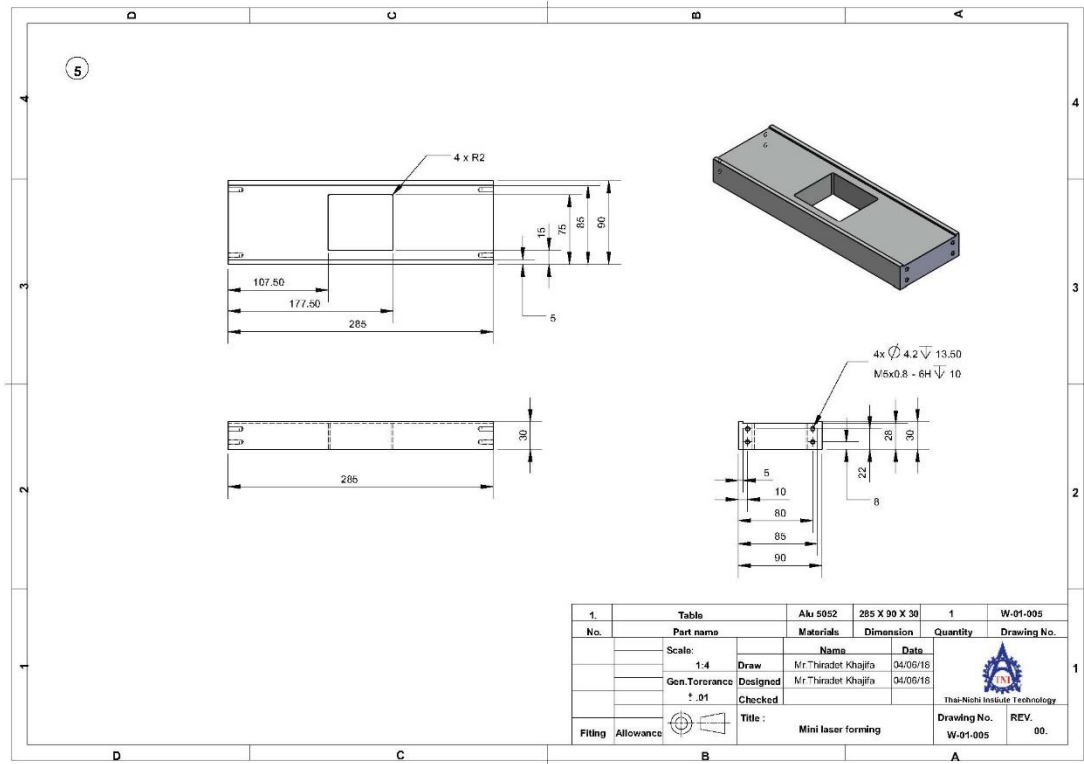
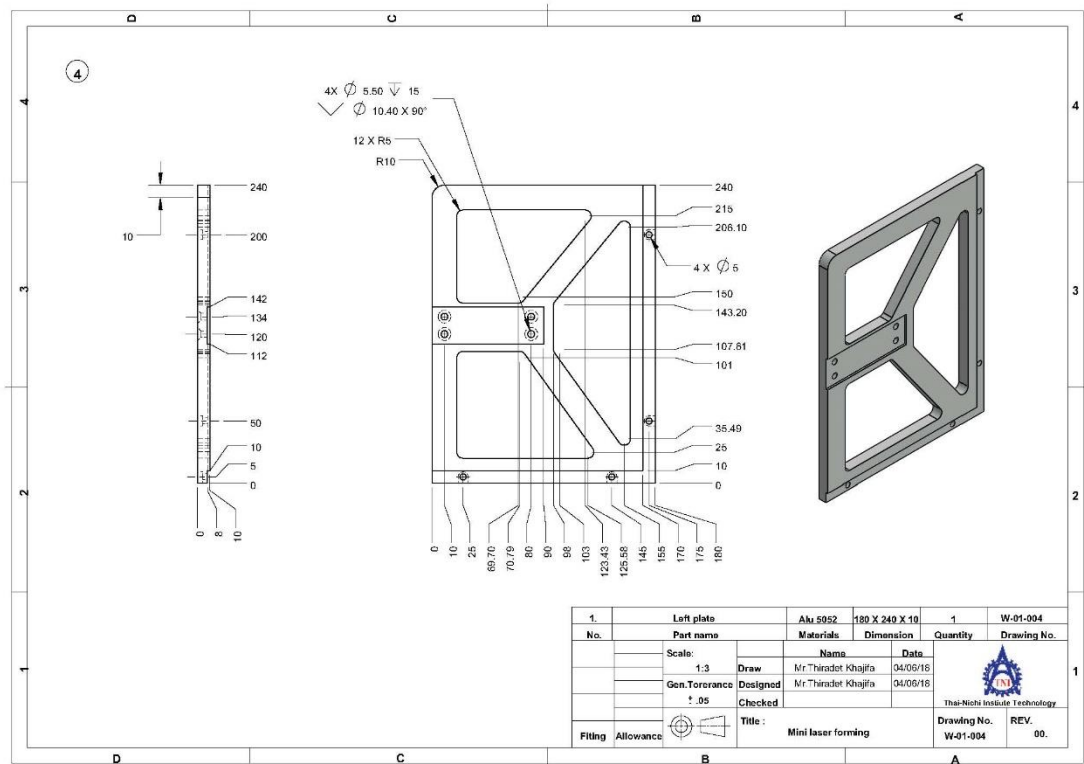
**P. Ninpetch**, N. Teenok, P. Kowitwarangkul, S. Mahathanabodee, R. Tongstri and P. Ratanadecho, The Influence of Laser Parameters on the Microstructure and the Micro Hardness of AISI 316L Fabricated by L-PBF process, IIW Congress Proceedings, 8th Asia Pacific IIW international conference congress, Queen Sirikit national convention centre (QSNCC), Bangkok, Thailand, 20th – 22th March 2019.

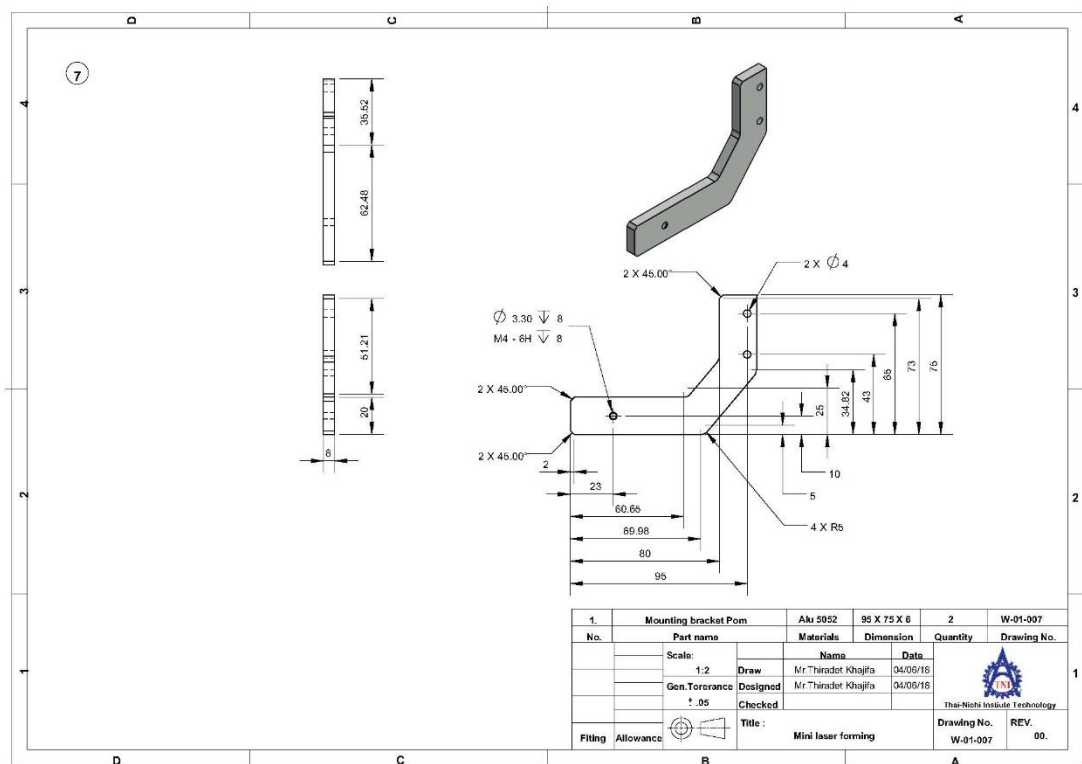
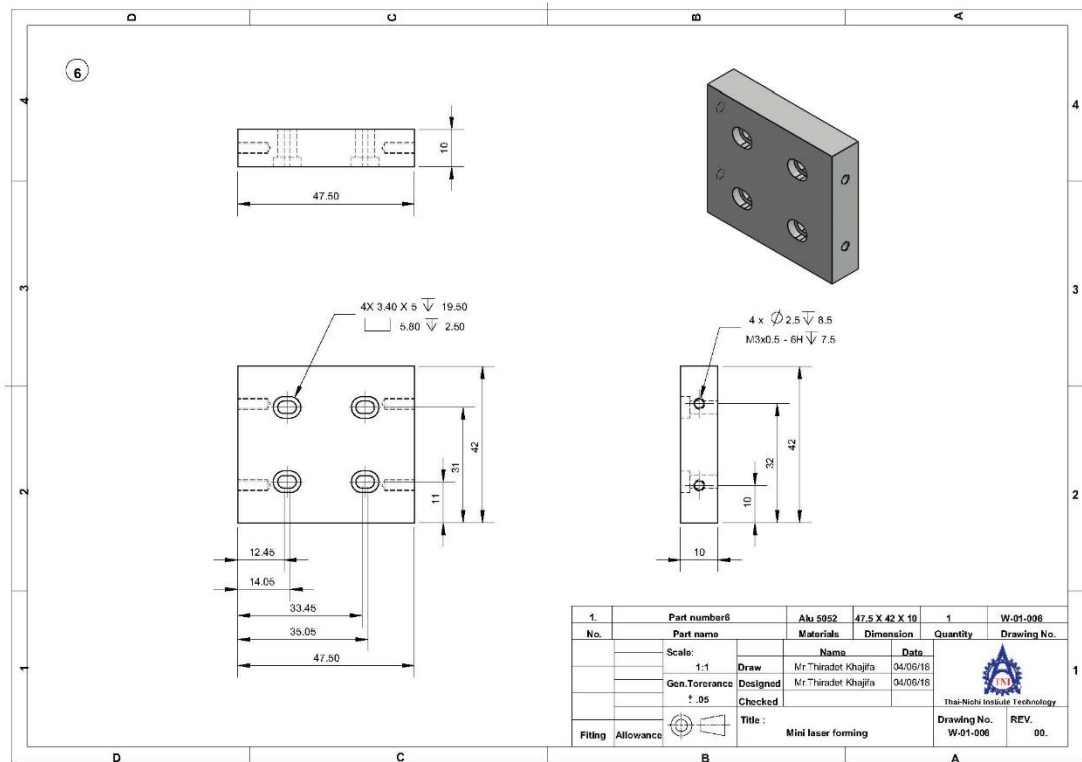
## **Appendix A**

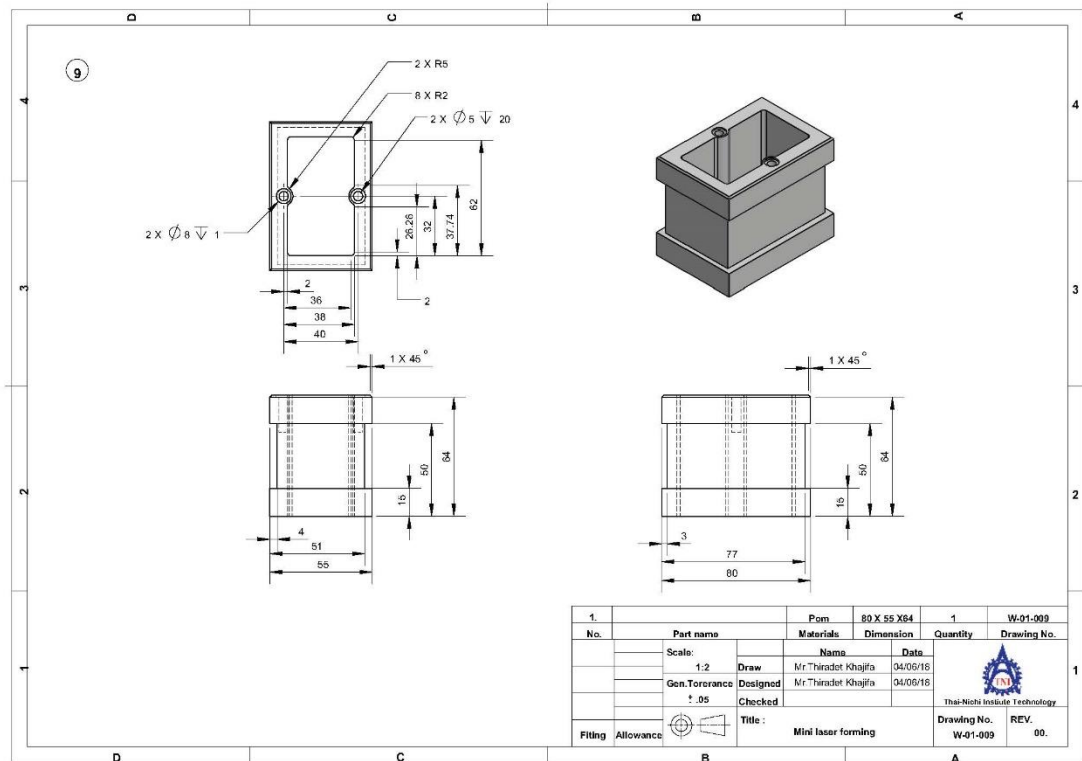
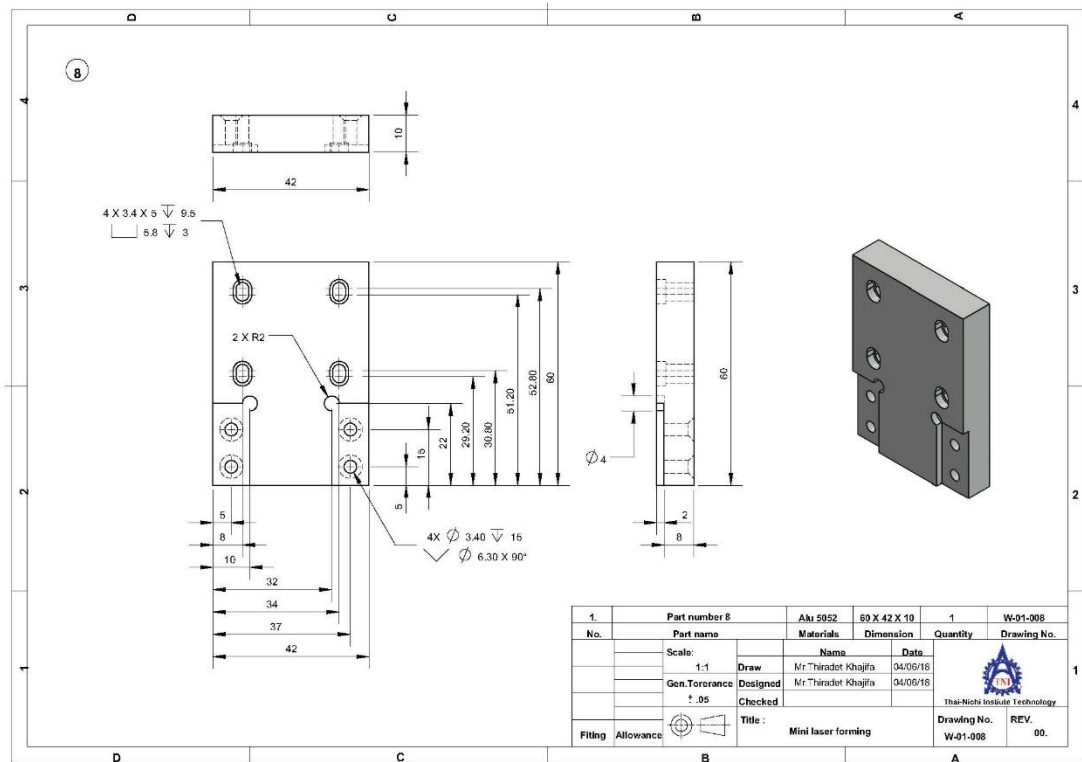
### **Building platform and gas chamber**

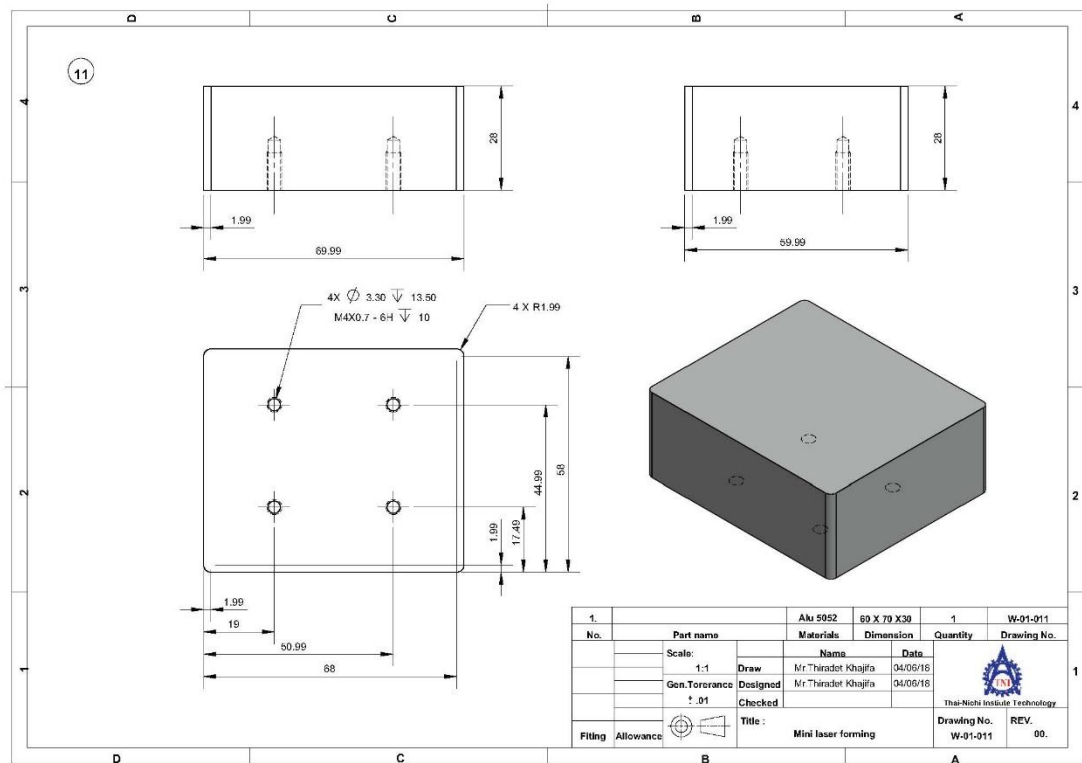
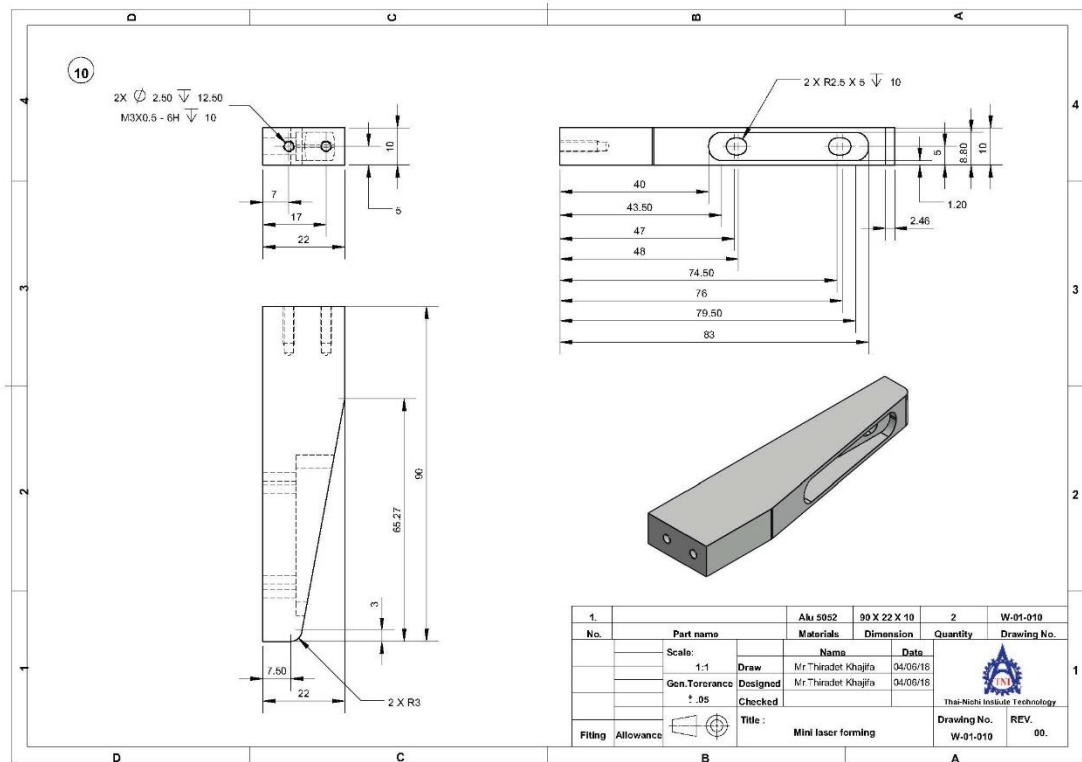


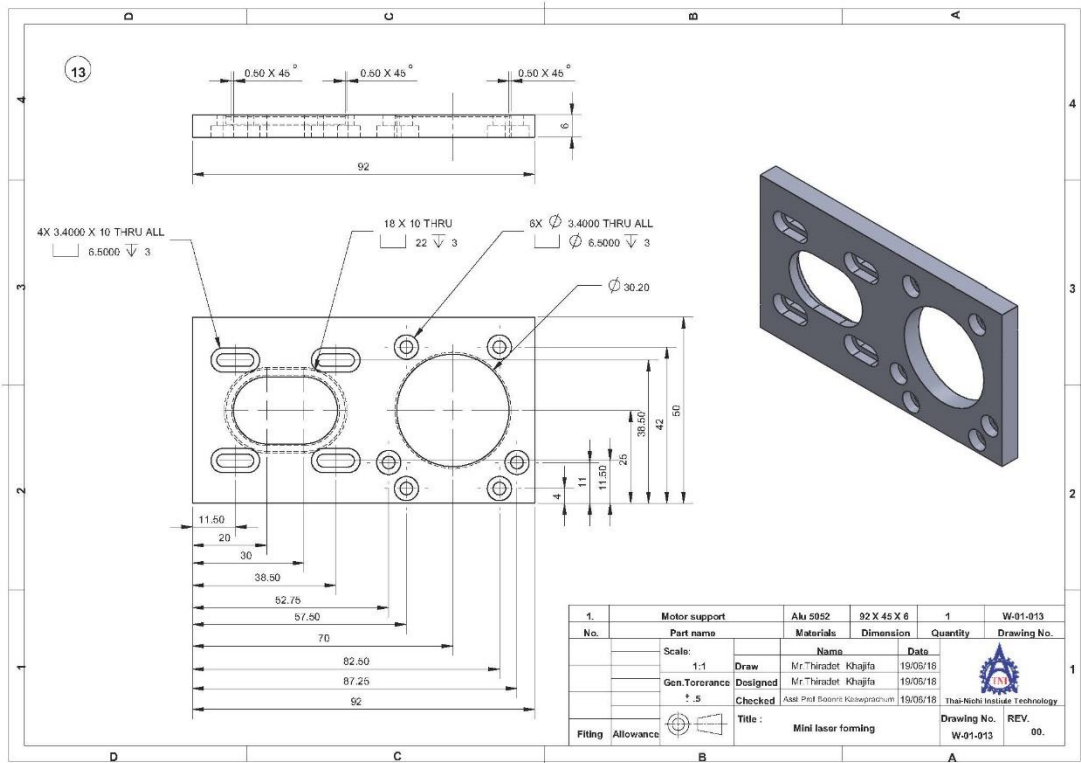
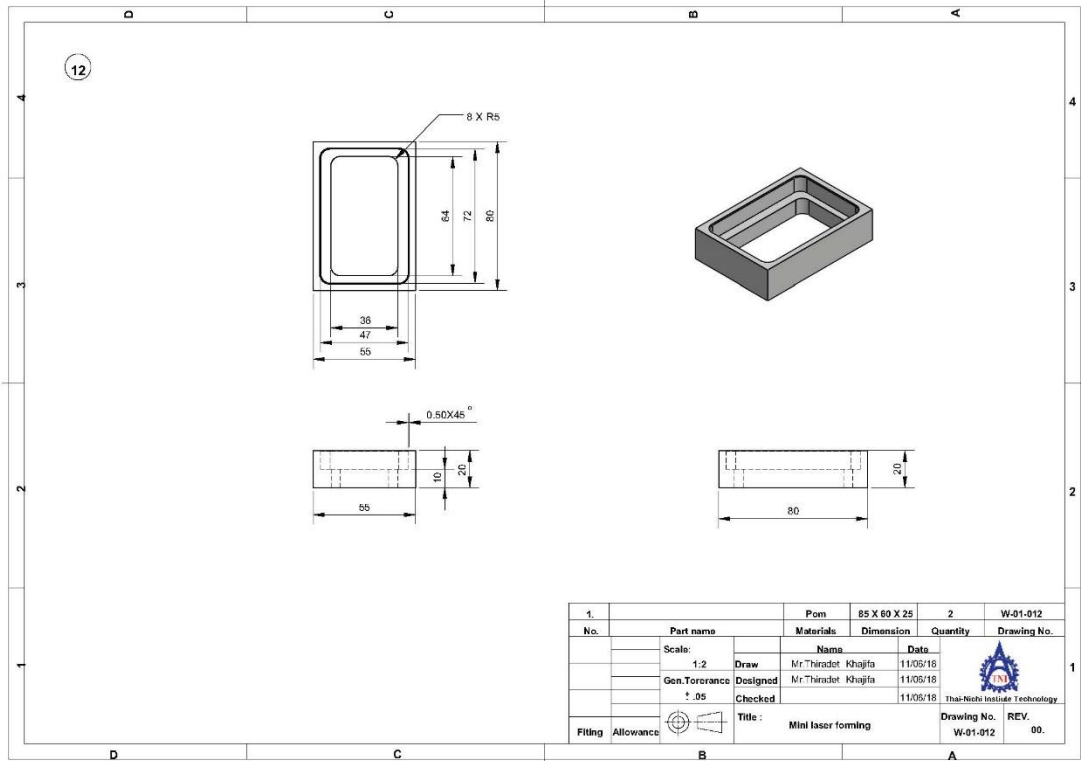












## **Appendix B**

### **Computer Simulation setup**

## Setting up a: Moving laser heat source simulation by ANSYS

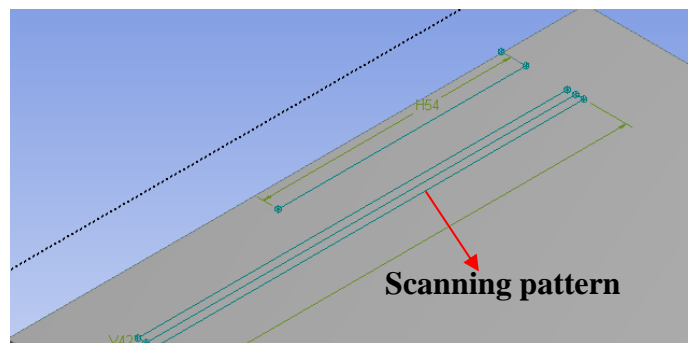
### 18.1

#### - Start program

1. Open ANSYS 18.1 software program, select the Transient thermal module
2. Click the Engineering data to define the material types and material properties

#### - CAD model

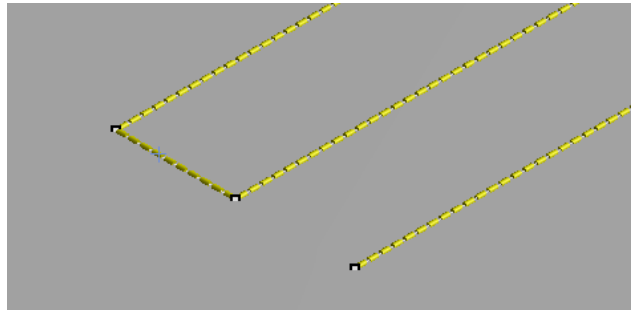
1. Select the geometry model, click edit geometry in design modeler.
2. Select the ZX plane, click sketching, click rectangle, drawing a rectangle and defined dimension.
3. Select extrude to define the thickness of workpiece.
4. Creating plane for draw pattern line, click new plane, click transform 1 (RMB) select offset Z and defined dimension at FD1, Value 1 blank from Details review window, and then click Generate.
5. Create the scanning pattern on the selecting plane.
6. Select the extrude command, click apply at geometry blank, click operation blank and select imprint face, and then click generate.



**Geometry CAD model with scanning pattern**

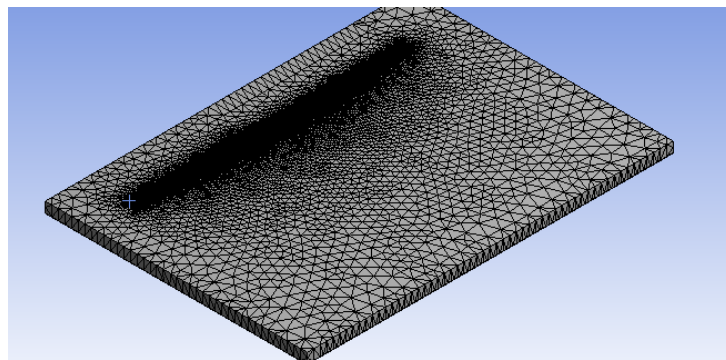
#### - Model

1. Right click model,  Model  , click edit.
2. Click geometry at outline window, click plus symbol (+), click solid and defined the material type in solid window.
3. Right click mesh, select insert, select mesh sizing, click along scanning pattern to create the finer mesh at scanning pattern.



### Edge sizing

4. Determine the element size to define amount of mesh and node, and then click generate.



### Meshing geometry

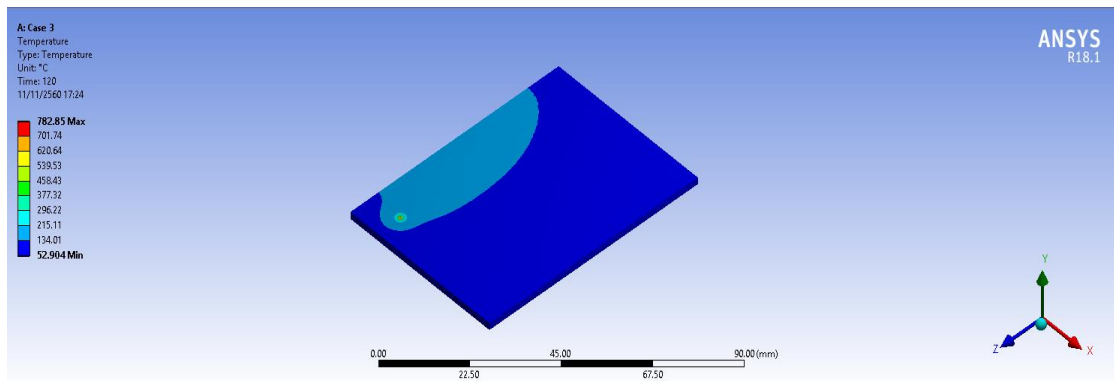
#### - Thermal Transient (D5) modeling

1. Click the initial temperature to define the initial temp.
2. Determine the boundary condition such as convection, radiation, heat flow, heat flux,
3. Select the moving heat flux model, moving heat source model, and then defined the details.

Details of "Moving Heat Flux"	
<input type="checkbox"/> <b>Geometry</b>	
Scoping Method	Geometry Selection
Geometry	1 Face
<input type="checkbox"/> <b>Path</b>	
Scoping Method	Geometry Selection
Geometry	2 Edges
<input type="checkbox"/> <b>Start Point</b>	
Scoping Method	Geometry Selection
Geometry	1 Vertex
<input type="checkbox"/> <b>Definition</b>	
Index	1
First Patch?	Yes
Last Patch?	Yes
Velocity	0.68 [mm sec <sup>-1</sup> ]
Radius of the Beam	0.34 [mm]
Source Power Intensity	50 [W mm <sup>-1</sup> mm <sup>-1</sup> ]
Start Time	0 [sec]
End Time	180 [sec]
Number of Segments	60
Minimum Steps for Cooling Phase	20
Material Removal	No
Melting Temperature	1500 [C]

Details of "Moving Heat Energy"	
<input type="checkbox"/> <b>Geometry</b>	
Scoping Method	Geometry Selection
Geometry	1 Body
<input type="checkbox"/> <b>Path</b>	
Scoping Method	Geometry Selection
Geometry	3 Edges
<input type="checkbox"/> <b>Start Point</b>	
Scoping Method	Geometry Selection
Geometry	1 Vertex
<input type="checkbox"/> <b>Definition</b>	
Index	1
First Patch?	Yes
Last Patch?	Yes
Velocity	0.68 [mm sec <sup>-1</sup> ]
Radius of the Beam	0.34 [mm]
Source Power	50 [W mm <sup>-1</sup> mm <sup>-1</sup> ]
Absorption Coefficient	0.3 [mm <sup>-1</sup> ]
Start Time	0 [sec]
End Time	180 [sec]
Number of Segments	60
Minimum Steps for Cooling Phase	20
Material Removal	No
Melting Temperature	1500 [C]

4. Click solution, click solve. After that you can get the simulation results



**Result of temperature distribution on workpiece**

## Setting up a: Simulation of the Laser powder bed fusion process using Flow-3D / Flow-weld software

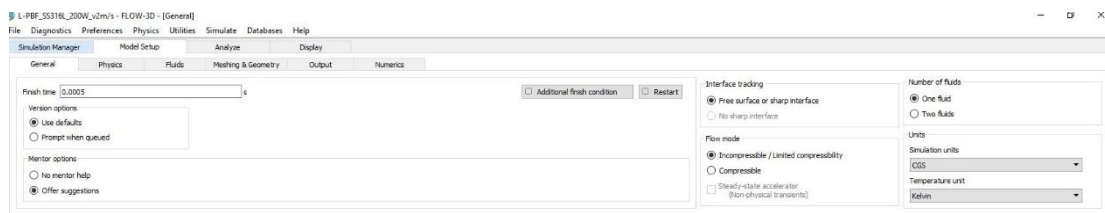
### - Simulation manager

1. Open the Flow-3D software
2. Click new work space and set the name of your project

### - Model setup

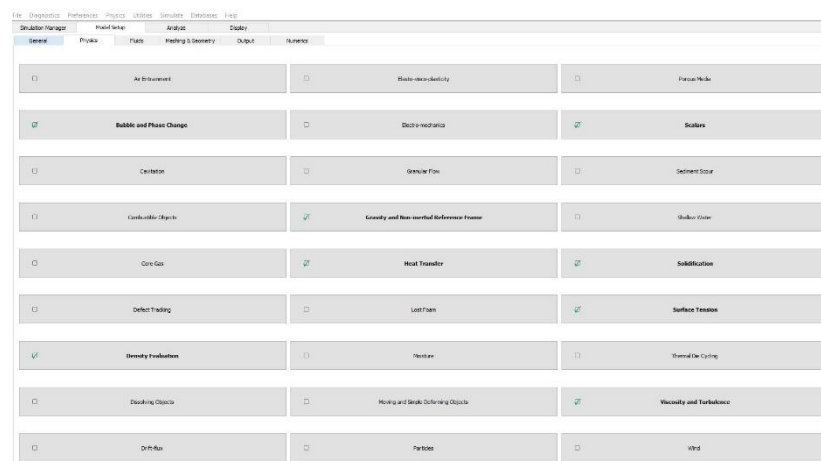
#### *Model setup - General*

1. Set finish time ( $t = s/v$ )  
\*s is distance of laser scanning (cm), v is velocity (cm/s)
2. Select *one fluid* in number of fluid model
3. Select *free or sharp surface* in interface tracking model
4. Select *incompressible or limited compressibility* in flow mode model
5. Click preference, select *default version option*, select *local*, select the *custom double precision* at version box



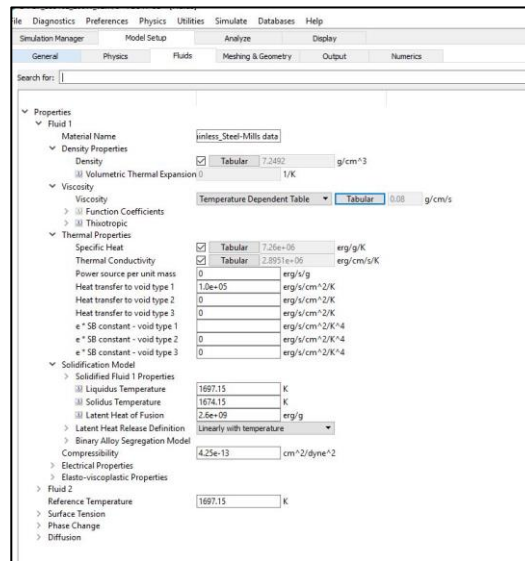
#### *Model setup - Physic*

1. Select the physical model *including Gravity, Heat transfer, Viscosity and Turbulence model, Solidification model, Density evaluation model, Surface tension and Bubble and phase change*



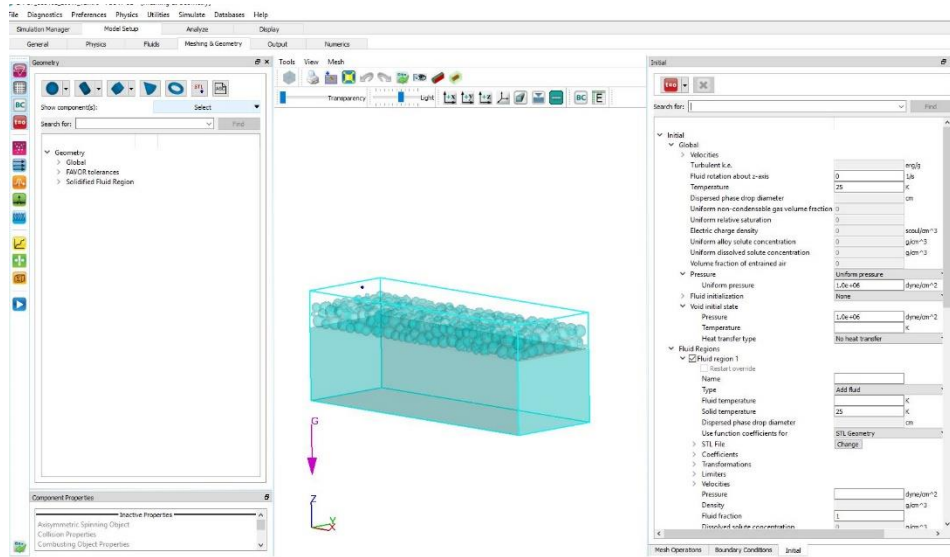
## Model setup – Fluid

1. Select material are used in your work by upload the material data from database



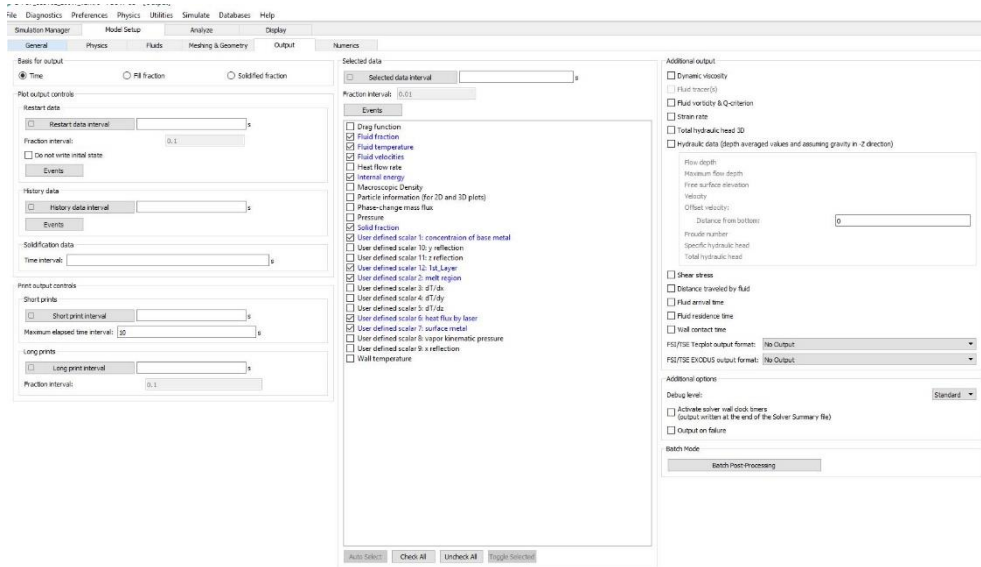
## Model setup – Meshing and geometry

1. Upload the STL file CAD 3D
2. Select mesh operation to define mesh type, mesh cell : size of cell



3. Define the boundary condition -> X min, X max, Y min, Y max define symmetry, Z max: define pressure of argon gas Z min: define that it is wall
4. Return to program code in edit simulation, define the scanning speed and laser power by importing the csv file to program code.

## - Output



## - The simulation result from Flow sight

